ROYAL INSTITUTE
OF TECHNOLOGY

Concepts for Compact Solid-State Lasers in the Visible and UV

Sandra Johansson

Doctoral Thesis

Department of Applied Physics
Royal Institute of Technology
Stockholm, Sweden 2006

Concepts for Compact Solid-State Lasers in the Visible and UV

Sandra Johansson
ISBN 91-7178-539-6
ISBN 978-91-7178-539-8

Doktorsavhandling vid Kungliga Tekniska Högskolan
TRITA-FYS 2006:72
ISSN 0280-316X
ISRN KTH/FYS/--06:72--SE

Akademisk avhandling som med tillstånd av Kungliga Tekniska Högskolan framlägges till offentlig granskning för avläggande av teknologie doktorsexamen i fysik, fredagen den 15 december 2006, kl. 10.00, Sal FB55, AlbaNova, Roslagstullsbacken 21, Stockholm. Avhandlingen kommer att försvaras på engelska.

Laser Physics
Department of Applied Physics
Royal Institute of Technology
SE-106 91 Stockholm, Sweden

Cover: Second harmonic generation in periodically poled $KTiOPO_4$.

Printed by Universitetsservice US-AB, Stockholm, 2006.

Johansson, Sandra
Concepts for Compact Solid-State Lasers in the Visible and UV
Laser Physics, Department of Applied Physics, Royal Institute of Technology, SE-106 91 Stockholm, Sweden
ISBN 91-7178-539-6, 978-91-7178-539-8, TRITA-FYS 2006:72, ISSN 0280-316X, ISRN KTH/FYS/--06:72--SE

Abstract

In many fields, scientific or industrial, optical devices that can be tailored in terms of spectral qualities and output power depending on the application in question are attractive. Nonlinear optics in combination with powerful laser sources provide a tool to achieve essentially any wavelength in the electromagnetic spectrum, and the advancement of material technology during the last decade has opened up new possibilities in terms of realising such devices.

The main part of the thesis deals with the development of compact functional lasers based on nonlinear interaction utilising diode-pumped solid-state lasers and also laser diodes. Efficient frequency conversion into the visible and ultraviolet part of the electromagnetic spectrum has been achieved, using both Nd:YAG and Nd:YVO_4 lasers as well as a semiconductor laser as the fundamental light sources. For the nonlinear conversion, periodically poled potassium titanyl phosphate (PPKTP), bismuth triborate (BiBO) and beta barium borate (BBO) have been employed.

In the search for compact and reliable light sources emitting in the visible part of the spectrum, two different approaches have been explored. First, a scheme based on sum-frequency mixing of a diode-pumped solid-state laser and a laser diode of good beam quality. The idea of this approach is to take advantage of the individual strength of each device, which would be the flexibility in terms of wavelength for the laser diode and the possibility to reach high output power from the diode-pumped solid-state laser. Second, by mixing two different solid-state lasers substantially more output power could be generated albeit at a cost of less freedom in the choice of spectral output. As these two light sources had their central wavelength at 492 nm and 593 nm, respectively, they are highly interesting in biomedical applications since they correspond to the peak absorption of several popular fluorophores.

In applications such as lithography, material synthesis and fibre grating fabrication, laser sources emitting in the deep-UV spectrum are desired. An all solid-state 236 nm laser source with 20 mW of average power have been designed and constructed, by frequency-quadrupling a passively Q-switched Nd:YAG laser lasing on a quasi-three level transition.

Also, a novel concept for miniaturising solid-state lasers has been examined. Using a heat-conductive polymer carrier, a generic approach especially suited for mass-production of functional laser devices is presented.

Finally, it has been proven that GRIN lenses can provide a very compact beam shaping solution to standard laser diodes based on the beam twisting approach. This method offers several advantages such as compactness of the beam shaping system, automated assembly in solid-state laser manufacturing due to the shape of these lenses and polarisation preservation of the laser diode output.

Keywords: nonlinear optics, frequency conversion, visible lasers, ultraviolet lasers, $KTiOPO_4$, BiBO, BBO, quasi phase-matching, birefringent phase-matching, solid-state lasers, diode-pumped lasers, Q-switched lasers, gradient-index lenses, laser beam shaping.

To my family

כל העולם כלו גשר צר
מאד והעיקר לא לפחד כלל.

Preface

The main part of the work resulting in this thesis was performed in the Laser Physics group at the Department of Applied Physics, Royal Institute of Technology in Stockholm, Sweden.

This project was made possible through the generous funding obtained from the Carl Trygger Foundation, The Lars Hierta Foundation, and the Helge Ax.son Johnson Foundation.

A fruitful collaboration within the framework of this thesis has been performed with the Nonlinear Optics group at DTU, Lyngby in Denmark, lead by Prof. Preben Buchhave.

The thesis is based on scientific work described in six articles. It contains an introductory part where a short historical background of the field of lasers and nonlinear optics is given, which is followed by an overview of the theory behind solid-state lasers together with a numerical investigation, and some general relations in nonlinear optics. The remaining chapters treat the experimental studies conducted during this project. This section is followed by the reprints of the publications listed below.

List of Publications

Publications included in the thesis

I. S. Johansson, S. Spiekermann, S. Wang, V. Pasiskevicius, F. Laurell, and K. Ekvall, ”*Generation of turquoise light by sum-frequency mixing of a diode-pumped solid-state laser and a laser diode in periodically poled PPKTP*,” Opt. Exp. **12** (20), 4935-4940 (2004).

II. S. Johansson, S. Wang, V. Pasiskevicius and F. Laurell, ”*A compact 492-nm light source based on sum-frequency mixing*,” Opt. Exp. **13** (7) 2590-2596, (2005).

III. J. Janousek, S. Johansson, P. Tidemand-Lichtenberg, S. Wang, J.L. Mortensen, P. Buchhave and F. Laurell, ”*Efficient all solid-state continuous-wave yellow-orange light source*,” Opt. Exp. **13** (4), 1188-1192 (2005).

IV. D. Evekull, S. Johansson, S. Bjurshagen, M. Olson, R. Koch and F. Laurell, “*Polymer encapsulated miniature Nd:YAG lasers*,” El. Lett. **39** (20), 1446-1448 (2003)

V. S. Johansson, V. Pasiskevicius, F. Laurell, R. Hansson and K. Ekvall, "*Solid-state laser pumped by twisted beam shaped laser diode*," Submitted to Optics Communications in November 2006.

VI. S. Johansson, S. Bjurshagen, C. Canalias, V. Pasiskevicius, R. Koch and F. Laurell, "*An all solid-state UV source based on a frequency-quadrupled, passively Q-switched 946 nm laser*," Submitted to Optics Express in October 2006.

Publications not included in the thesis

1. S. Johansson, S. Bjurshagen, F.Laurell, R. Koch and H. Karlsson, ”*Advanced technology platform for miniaturised diode-pumped solid-state lasers*,” EPS-QEOD Europhoton Conference (Lausanne, Switzerland, 2004), paper FrB6.

2. S. Johansson, S. Spiekermann, V. Pasiskevicius, F. Laurell, Katrin Ekvall, and S. Wang, ”*Generation of turquoise light by SFM a DPSSL and a laser diode in a single-pass configuration*,” Conference on Lasers and Electro-Optics (San Fransisco, California, 2004), paper CFE3.

3. J. Janousek, S. Johansson, P. Tidemand-Lichtenberg, J. Mortensen, P. Buchhave and F. Laurell, ”*Efficient generation of continuous-wave yellow-orange light using sum-frequency in periodically poled KTP*,” Advanced Solid-State Photonics (Vienna, Austria, 2005), paper MF26.

4. J. Janousek, S. Johansson, P. Tidemand-Lichtenberg, J. Mortensen, P. Buchhave and F. Laurell, ”*Efficient generation of continuous-wave yellow-orange light using sum-frequency generation in periodically poled KTP*,” Trends in Optics and Photonics Series Vol 98 (2005).

5. P. Tidemand-Lichtenberg, S. Johansson, M. Andersen, J. Janousek, P. Buchhave and F. Laurell, ”*Pulsed, all solid-state light source in the visible spectral region based on non-linear cavity dumping*,” Advanced Solid-State Photonics (Lake Tahoe, Nevada, 2006), paper TuB19.

Acknowledgements

This thesis would not have been possible without the help and support from several different persons.

First of all, I would like to express my gratitude to Prof. Fredrik Laurell for accepting me as a PhD student in his group. Your endless support and positive attitude has certainly made things easier to cope with during my stay in the Laser Physics group. Being your student has provided me with opportunities that would otherwise have been out of reach for me.

Without the guidance and support from Dr. Valdas Pasiskevicius many of the projects that I have been working with would never have been successful. Your patience, enthusiasm and investment in time concerning experimental as well as theoretical work have inspired me to reach for higher goals.

Furthermore, I want to express my gratitude to Cobolt AB and its people, Dr. Katrin Ekvall, Renée Hansson, Dr. Gunnar Karlsson, Dr. Shunhua Wang, and Dr. Håkan Karlsson. Without you, I would never have been able to generate that beautiful turquoise radiation. Thanks for supplying me with all that optics, laser crystals and PPKTP crystals. And not to forget, for all good parties that we had together.

A successful joint project on yellow-orange lasers was made possible through the collaboration with the Nonlinear Optics group at DTU, Denmark. I would especially like to thank Jiri Janousek and Dr. Peter Tidemand-Lichtenberg for the time that you invested in the project and for the hospitality you showed me each time I visited your lab.

I would also like to thank the people at ACREO AB for fruitful collaborations, especially Dr. Ralf Koch, Dr. Walter Margulis, David Evekull and Åsa Claesson.

Thanks to Agneta Falk, the administrative issues were made a lot easier. Rolf Helg in the mechanical workshop always seemed to be able to have that extra time to manufacture all those mounts and holders quickly whenever I needed it, I am very grateful for that. Not to forget, without the help from Assoc. Prof. Jens A. Tellefsen a lot of important details would have been forgotten. Thanks for staying around even though you could have stayed home and enjoyed your retirement.

I am very grateful for the assistance that I have received from Dr. Stefan Bjurshagen, it has been very nice collaborating with you and sharing office with you. Special thanks to Dr. Carlota Canalias for fabricating an almost endless row of PPKTP crystals, I owe you a lot. I would also like to thank Dr. Mikael Tiihonen for invaluable tips on what do after my PhD studies, Jonas Hellström for all the good times on Stureplan, Pär Jelger for sharing my interest in fashion, Björn Jacobsson for interesting discussions, and Stefan Holmgren for sharing his knowledge in laser physics. In addition, I would like to thank all diploma workers currently working in our group who have certainly made the lunch times and coffee breaks a lot funnier; Ida, Patrik, Mats, Hanna, Anna-Kristin and Jimmy. For those rewarding (and sometimes just funny) discussions on physics and all other topics of the world, I would like to thank all of my colleagues.

Finally, I would like to express my gratitude to all my friends and extended family in Stockholm, Gothenburg and Berlin for always being there for me and for all the good times that we had together. Special thanks to my home girls Christi and Sussi for making me laugh when I needed it the most. And last, but definitely not the least, I thank my mother and my sister Jenny for believing in me.

Table of Contents

Chapter 1

Introduction

1.1 Background

Ever since C. Schawlow and C. H. Townes[1] proposed the idea of extending the maser principle to the optical frequency part of the electromagnetic spectrum and thereby inventing the laser, the development of light sources tailored for specific applications has been a major part of optical research. The first practical laser was demonstrated one and a half years later, in August 1960 by T. H. Maiman[2], and shortly afterwards, generation of second harmonic radiation was observed for the first time by P. A. Franken *et al*[3] by focussing a ruby laser into crystalline quartz. It was not a coincidence that these two publications occurred during the same short time-span, since nonlinear effects are dependent on powerful, coherent light sources. For the last decades, the fields of non-linear optics and lasers have been intertwined and have evolved in parallel.

Today, there are a vast number of applications for lasers such as: IT and fiber communication, micromarking and microsurgery, industrial drilling and welding, remote sensing and range-finding, to just mention a few. The rare-earth doped solid-state lasers have characteristics features that are advantageous in both research and industrial applications. Examples of these are high efficiency, good beam quality and the possibility of Q-switching due to the generally long life-time of the upper laser level. The solid-state crystals are also practical as laser materials since they are neither electrostatically sensitive nor diffusive. Furthermore, the solid-state lasers can be made very small in size using the microchip laser approach. With the development of high-brightness GaAlAs laser diodes in the late 1980's, the low quantum defect of solid-state materials could be exploited because of the possibility to pump the rare-earth ions directly into the absorption band. In addition, the high absorption also permits the use of smaller laser crystals, thus facilitating compact devices.

A serious drawback of a conventional solid-state laser is that it can not have an arbitrary wavelength. This is because the emission wavelengths of the laser are governed by the energy levels of the gain medium, which in turn are given by the specific dopant and the host material. Nonlinear optics provides a solution to this problem, by the use of parametric processes in nonlinear materials. In these processes, frequency conversion interactions take place in a medium, where optical waves exchange energy among themselves. For example, an optical wave incident on a nonlinear crystal can generate a new wave with a frequency consisting of higher harmonics of the frequency of the incident wave. Thus, radiation of other frequencies than those produced directly by lasers can be obtained.

However, there are certain physical constraints in a nonlinear interaction that should be fulfilled. First, the photon energy conservation principle must be met. In the case of sum frequency generation with three interacting waves at frequencies ω_1, ω_2 and ω_3, respectively, this principle gives the relation $\omega_1 + \omega_2 = \omega_3$. Second, the photon momentum must be conserved in order for the nonlinear process to be efficient. This is the physical meaning of the term phase-matching, which simply says that the interacting waves must propagate at the same velocity. Since all materials have frequency dependent refractive indices, phase-matching techniques have to be used. Initially, the predominant technique was birefringent phasematching, but this kind of phase-matching does not always provide access to the highest nonlinear coefficient in the material. When the technique of quasi phase-matching (QPM) was proposed in the early 1960's it opened up for more nonlinear material flexibility and freedom in the choice of possible frequency interactions. In the case of ferroelectric nonlinear materials, it is possible to achieve periodic domain inversion by employing the so-called ferroelectric poling technique, which was first demonstrated by Yamada *et al* in 1993[41].

The combination of this QPM technique and nonlinear materials such as $KTiOPO_4$ (KTP) and its isomorphs, together with diode-pumped solid-state lasers has made it possible to construct very compact and efficient devices that are available in both the pulsed regime and continuous wave. Depending on the practical application, such as biomedical analysis and medical treatments, color display technology, optical data storage, reprographics and spectroscopic applications, the optical device can be tailored in terms of wavelength, output power and time scale. For many applications, the size of the optical device is crucial. Large and bulky devices are often unpractical and difficult to manage. Therefore, down-scaling the size of the frequency-converted, diode-pumped solid-state laser is an important issue. In addition, if these devices can be assembled in a way to make the production more cost-effective, the number of applications could be even more widespread. This field was initially investigated by Å. Claesson *et al*[52], by constructing miniature lasers on a silicon microbench building set.

The field of nonlinear optics and laser physics continues to evolve together with the advances in material science. As an example, nonlinear materials with high resistance to the photochromic effect are in demand in high-power applications, thus making it possible to exploit the full potential of the nonlinearity. The interdisciplinary nature of the field and the wide range of possible applications, both in research and industry, is probably the reason why it is still a growing and vital research field.

1.2 Development of the Work

This work was initiated by a search for novel concepts for functional and compact solid-state lasers with their possible applications in areas such as biomedicine, display technology and optical data storage. The project started out with the investigation of the microcarrier platform as a building set for inexpensive and low power lasers. Using a thermally conductive polymer as the carrier material, we were able to generate 2 W of output power from a microchip Nd:YAG in a 50 mm long carrier.

However, a large part of the experimental work was devoted to the design and construction of solid-state lasers emitting in the visible part of the electromagnetic spectrum, using sum-frequency generation. The concept of employing a laser diode and a solid-state laser in sum-frequency mixing was already presented by Risk et al[81] in 1988. This approach was further examined using the single-transverse mode output from a low power laser diode, and a diode-pumped solid-state laser, and since there is a drive for compact and efficient lasers in the blue spectral region, we choose to use a 915 nm laser diode in combination with a 1064 nm solid-state laser. As material technology had advanced considerably since the late 1980's, we could benefit from the high nonlinearity of periodically poled KTP. It showed that 4 mW of 492 nm power could be achieved in a single-pass configuration, which corresponds to a conversion efficiency as high as 2.2 $\%W^{-1}cm^{-1}$. A natural continuation of this project was to design it as an intra-cavity configuration, where the PPKTP crystal was placed inside the high circulating field of the solid-state laser. Still maintaining the small dimensions of the experimental setup, we were able to generate 27 mW of 492 nm power. However, since optimum focussing conditions inside the nonlinear crystals are difficult to combine with a very compact experimental setup, the latter experiment resulted in a somewhat lower conversion efficiency of 0.45 $\%W^{-1}cm^{-1}$. If visible output power up to the Watt range is to be achieved, one has to scale up the dimensions, and since laser diodes in the high power region do not produce light of high beam quality, the use of diode-pumped solid-state lasers is preferred. To explore the possibilities of producing several hundreds of milliwatts of power in the visible spectral region, we mixed two different diode-pumped solid-state lasers in a semi-intracavity configuration. As light sources in the yellow-orange spectral region are attractive in dermatology and ophthalmology, we combined two Nd:YVO_4 lasers, operating at 1064 nm and 1342 nm, respectively, to reach the 593 nm wavelength. Using a fairly compact experimental setup, we could generate 750 mW of 593 nm power in a Gaussian mode. Considering that the total diode power was 6.4 W only, this gives an optical-to-optical efficiency of 11 %.

In applications such as lithography and material synthesis, laser sources emitting in the deep-UV spectrum are desired. Our approach was to frequency-quadruple a passively Q-switched Nd:YAG laser lasing on a quasi-three level transition. For conversion into the blue spectral region, PPKTP and BiBO were examined in terms of conversion efficiency and their ability to generate stable second-harmonic power. For the last step, a BBO crystal was used for the generation of 236 nm power since very few other nonlinear crystals are transparent in this spectral region.

Finally, we explored the possibility to beam shape the elliptic and astigmatic beams from conventional laser diodes with without using bulky standard spherical or cylindrical lenses. It was shown that GRIN lenses can provide a very compact beam shaping solution to standard laser diodes based on the beam twisting approach. This method provides several advantages such as compactness of the beam shaping system, automated assembly in solid-state laser manufacturing due to the shape of these lenses and polarisation preservation of the laser diode output.

1.3 Thesis Outline

The thesis is built up as follows. Chapter 2 presents an overview of the basic theory of solid-state lasers. The rate equations for a quasi-three level system are introduced together with the theoretical background for passive Q-switching, leading the numerical simulations presented at the end of the chapter. Chapter 3 is intended to establish a general knowledge of the field of nonlinear optics. Some important equations are derived and the nonlinear processes second harmonic generation and sum-frequency generation are introduced and explained. It also covers the two main methods used for phase-matching of nonlinear processes. Chapter 4 presents two different design concepts for miniaturising solid-state lasers. Chapter 5 is devoted to the development of light sources in the visible spectral region based on sum-frequency mixing. Two light sources are presented, emitting in the turquoise and the yellow spectral region, respectively. Chapter 6 deals with the construction of a solid-state deep UV light source. Chapter 7 contains a summary of the original work and my contribution to each paper. Finally, I will conclude my work in Chapter 8.

Chapter 2

Solid-State Lasers

The use of lasers played a crucial role for the evolvement and practical implementation of nonlinear optics. In this Chapter, an overview of the governing relations in laser theory and some important equations is given. In the last part, results from a numerical simulation of a passively Q-switched quasi-three level laser are presented. These simulations were conducted during the development of the UV laser source described in Chapter 6, as a means to optimise the fundamental light source.

2.1 Basic theory

A laser is based on the concept of stimulated emission of radiation, where an electron is stimulated by a photon to give up its energy and decay to a lower energy level. In this process, another photon is created having exactly the same characteristics as the first photon in terms of frequency, polarisation, phase and propagation direction. The condition for this to happen is that the energy of the incoming photon matches the energy level difference between the higher and lower energy states, or

$$E_p = h\upsilon \approx E_j - E_i, \tag{2.1}$$

where $E_j > E_i$, ν is the frequency of the incoming photon and h is Planck's constant. This expression states that the energy of the incoming photon does not have to exactly equal the energy difference between the two electron states. The probability function for a photon to interact with a atom is not given by Dirac's delta function centred at ν, but is broadened with respect to the frequency into a lineshape function $g(\nu)$. This lineshape function can have different appearances depending on the type of broadening that is present in the specific atomic system. There exist mainly two types of broadening, homogeneous and inhomogeneous broadening. The first type describes a system where all atoms are indistinguishable and have the same transition energy and central frequency. Here, the overall lineshape of the absorption cross section is identical with the lineshape of the single-atom cross-section. In this case, the emission of a photon at a certain frequency reduces the subsequent average probability homogeneously over the linewidth. In for example Nd:YAG, the main homogeneous broadening mechanism is thermal broadening, where the thermal vibrations of the lattice surrounding the active ions influences the atomic transition. Inhomogeneous broadening on the other hand describes a system where the atoms are distinguishable, and the emission of a photon will reduce the subsequent average probability inhomogeneously over the linewidth. The overall response of a collection of atoms to an applied signal is broadened, due to displaced centre frequencies of the individual atoms. For solid-state lasers, crystal inhomogeneities can be a cause for inhomogeneous broadening. This may lead to so-called spectral hole-burning, where the emission around a certain frequency is temporarily obstructed because of reduction of the gain at that particular frequency (a "hole" is burned in the gain curve).

Not only the stimulated emission process is possible in the photon-electron interaction between two energy states E_i and E_j, but also the two processes absorption and spontaneous emission. Absorption is essentially the inversion of stimulated emission, where an atom with an electron in the lower energy state absorbs a photon of energy E_p and is thus excited to the higher energy state. Whereas stimulated emission involves radiation of a photon that is an exact copy of the incoming photon, spontaneous emission is a process where an electron is spontaneously de-excited into the lower energy state, thereby emitting a photon of random phase and propagation direction. Its energy (and thus its frequency distribution) is described by the lineshape function $g(\nu)$.

In thermal equilibrium, the population density N_j (population number per volume) of the state of higher energy is lower than that of the lower energy state according to Boltzmann statistics, but if the population densities are inverted, this will result in an exponential decay of the population density N_j into the lower level E_i. This decay will governed by a time-constant τ_j, called the spontaneous emission lifetime.

2.2 Intensity gain and absorption

By considering a thin slab of thickness dz submitted to an applied optical signal of intensity I, it is possible to derive expressions for gain and absorption as function of the population densities. A schematic picture of the energy level system for the media can be seen in Fig. 2.1. It is assumed that the atoms in the slab have an average absorption cross-section σ_{ij}, which gives the probability for an atom to be excited to the higher energy state E_j. Likewise, there is a corresponding probability for the atom to relax into the lower energy state E_i upon emitting a photon which is related to the stimulated emission cross section σ_{ji}. Then, the power emitted or absorbed by an individual atom in the slab is given by $\sigma \cdot I$. Taking all atoms of the slab into account, the total intensity absorbed in the length element dz is consequently $N_i \sigma_{ij} dz \cdot I$. Similarly, the total emitted intensity is $N_j \sigma_{ji} dz \cdot I$. The net difference is thus[4-6]

$$dI = \left(N_j \sigma_{ji} - N_i \sigma_{ij}\right) I\, dz \tag{2.2}$$

It should be noted that the absorption cross section and the stimulated emission cross sections are related through the expression $\sigma_{ji} = \sigma_{ij}\, g_i / g_j$ [5,6], where the g_i and g_j are the degeneracy factors of the states E_i and E_j, respectively. The light beam of initial intensity I will thus experience a net gain or decay depending on the sign of $N_j \sigma_{ji} - N_i \sigma_{ij}$, thereby implying that N_j has to be larger than $N_i\, g_j / g_i$ in order for the optical signal to be amplified. Rewriting the expression above gives the following differential equation

$$\frac{dI}{dz} = \sigma_{ji} \Delta N \cdot I \tag{2.3}$$

where the so-called population-inversion density is defined as $\Delta N = N_j - N_i\, g_j / g_i$. This equation can be easily solved according to

$$I(z) = I(0)\exp\left(\sigma_{ji}\Delta N \cdot z\right) \tag{2.4}$$

Here, the gain coefficient is defined as $g = \sigma_{ji}\Delta N$, implying that if $N_j > N_i\, g_j/g_i$, the optical signal will grow exponentially as it traverses the slab. On the other hand, if there is no population inversion (i.e. $\Delta N < 0$), there will be a net absorption of the optical signal in the medium. The corresponding absorption coefficient is then defined as

$$\alpha = \left(\frac{g_j}{g_i}N_i - N_j\right)\sigma_{ji} \quad . \tag{2.5}$$

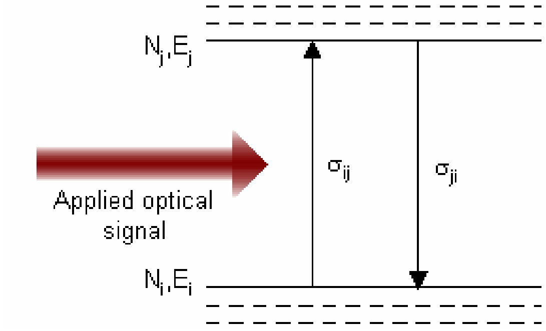

Fig. 2.1 Schematic of the energy levels with their absorption and emission cross-sections.

It is important to note that population inversion can never be reached in a two-level system. This is since the probability for absorbing a photon is exactly equal to the probability of emitting a photon, once $N_j = N_i\, g_j/g_i$. In other words, the absorption becomes saturated and the additional absorption required for population inversion will not occur. Thus, the gain required for lasing action is achieved in multi-level systems. A typical example is the four-level laser system, where an energy state at a higher level than E_j, termed E_k, together with the ground state with the energy E_0 are taking part in the stimulated emission process. Here, the electrons in the ground state are excited, often by means of optical pumping, to the highest energy state with energy E_k, and from there it rapidly decays to E_j through non-radiative relaxation. In order for the process to be efficient, the time-scale of this decay must be much shorter than the spontaneous emission life-time of the energy state E_j. If the population of the lower energy state E_i is negligible at thermal equilibrium, population inversion between E_j and E_i is easily reached and stimulated emission takes place between the upper laser level E_j and the lower laser level E_i. In addition, fast relaxation from E_i to E_0 is also desirable for reaching population inversion between the laser levels. Nevertheless, other laser systems are also possible, such as the three-level laser system where the lower laser level coincides with the ground-state E_0. In materials exhibiting Stark splitting of the energy states, i.e. when sublevels are present within the different energy levels, the lower laser level can be thermally populated if it lies close enough to the ground-state level. In this case, the system is called a quasi-three level laser system. In the following sections, the latter kind of laser system will be modelled using the so-called rate equations.

2.3 Rate equations

The modelling of laser systems are often expressed through the rate equations. As an example, the 946 nm laser transition of Nd:YAG is considered. This transition takes place between the lowest Stark level of the energy state $^4F_{3/2}$ and the highest Stark level of the energy state $^4I_{9/2}$, as seen in Fig. 2.2. Thus, the lower laser level is a sublevel of the ground state level.

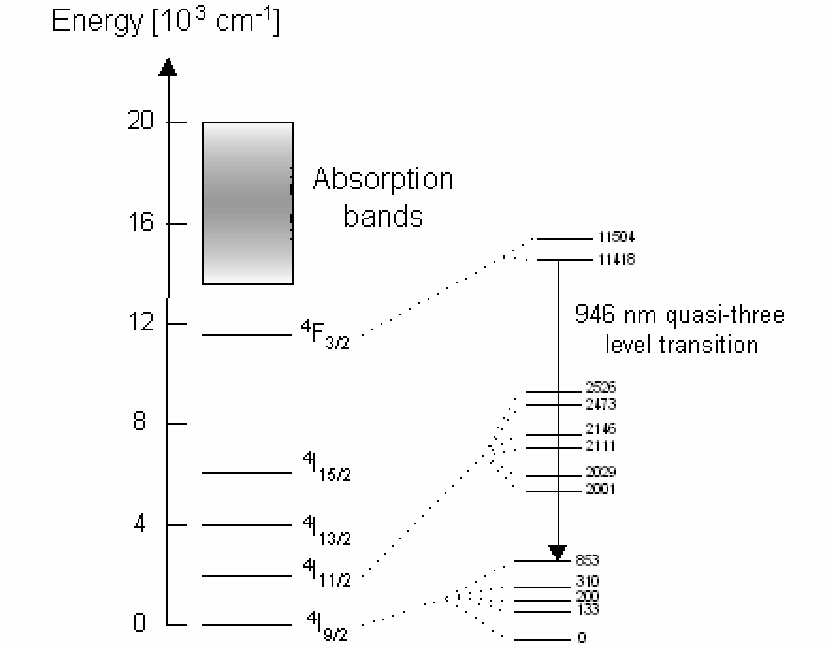

Fig. 2.2 The energy diagram for Nd^{3+} in the YAG host. For clarity, only the Stark sublevels of the two lowest energy levels and the upper laser level are shown.

This is a quasi three-level system where the Nd^{3+} ions are excited from the ground state into the absorption level 3 and then very rapidly decay via multiphonon relaxations down to the metastable upper laser level 2. After the laser transition, the ions relax from the upper Stark level of the energy state $^4I_{9/2}$ to the lowest level within the same manifold. A simplified scheme of the energy levels with their corresponding population densities and life-times is shown in Fig. 2.3. Here, the ground state and upper laser level population densities are N_1 and N_2, respectively and the population density of the absorption level is termed N_3. The doping concentration or the total population density is termed N_0 and for the laser system described here, N_3 is so small that $N_0 \approx N_1 + N_2$.

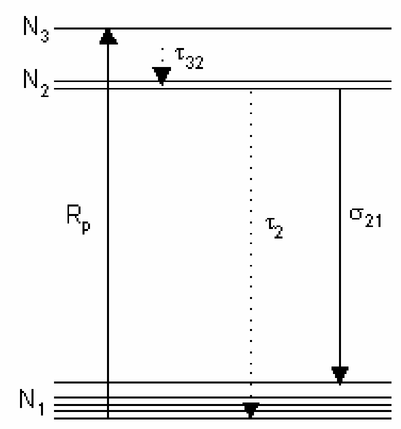

Fig. 2.3 The energy diagram for a quasi-three-level laser system.

The excitation of the ions at the ground state into the absorption level is typically achieved employing optical pumping. In this work, laser diodes have been used in an end-pumping configuration. All of the pump power of the laser diode is not absorbed by the laser crystal, and the fraction of the incident power that is absorbed is called the absorption efficiency, given by $\eta_a = 1 - \exp(-\alpha l_{cr})$ as can be deduced from Eq. 2.4 and Eq. 2.5, where l_{cr} is the length of the crystal and α is the absorption coefficient given by $\alpha = \sigma_p N_0$. It should be noted that in the latter expression pump saturation has been neglected, and is thus an approximation. In addition, it has been assumed that the pump beam makes a single-pass through the material. Also, an effective absorption cross section σ_p have been used for the transition from the ground-state level to the absorption band. The pumping process to the absorption band is described by the pump rate density R_p given by

$$R_p(x,y,z) = \frac{\eta_a \eta_p \lambda_p P_P}{hc_0} r_p(x,y,z) \tag{2.6}$$

where η_p is the quantum efficiency of the pumping process, λ_p is the centre wavelength of the pump source, c_0 is the velocity of light in vacuum and P_p is the incident pump power. It should be noted that η_p can be close to unity when using a pump with a narrow bandwidth (e.g. a laser diode), whereas for flash lamp pumping, it can be significantly reduced. The function r_p is the normalised spatial distribution of the pump beam over the laser crystal. This function is usually considered to be Gaussian, but for simplicity it is here assumed to have a top-hat shape. Also neglecting exponential decay of the pump power, the pump rate density can then be written as

$$R_p = \frac{\eta_p \alpha \lambda_p}{hc_0} \cdot \frac{P_p}{A_{eff}} \tag{2.7}$$

where $A_{eff} = \pi \omega_p^2 / 2$ is the effective Gauss area for a pump beam with $1/e^2$-radius ω_p. In addition, an effective pump radius can be defined as[7]

$$\overline{w}_p^2 = \frac{\int_0^{l_{cr}} w_p^2(z)\exp(-\alpha z)dz}{\int_0^{l_{cr}} \exp(-\alpha z)\mathrm{d}z} \tag{2.8}$$

where l_{cr} is the length of the laser crystal and $w_p(z)$ is described as a Gaussian beam using the beam propagation factor $M^2 = 52$ for the pump source.

In order to model how the photon density builds up inside a laser, a simple cavity with two mirrors and a laser crystal with refractive index n is considered. The reflectivity of the outcoupling mirror is R, and the optical path length of the cavity is l_c^*. A residual round-trip loss L is assumed. If the spatial distribution of the laser mode is considered to be a uniform top-hat function instead of Gaussian, the rate equations governing the temporal dynamics of the population densities of the laser levels N_1 and N_2 as well as the photon density ϕ can be formulated according to [5,6]

$$\begin{aligned} \frac{dN_2}{dt} &= -\frac{dN_1}{dt} = R_p - \frac{N_2}{\tau_2} - c_0\sigma_{21}\Delta N\phi \\ \frac{d\phi}{dt} &= \frac{\phi}{t_r}\left(2\sigma\Delta N l_{cr} - \delta\right) \end{aligned} \tag{2.9}$$

where $t_r = 2l_c^*/c_0$ is the round trip time in the laser cavity and $\delta = L - \ln R$ is the total round trip loss in the cavity. A so-called cavity lifetime of the photons can be defined from these two parameters, given by $t_c = t_r/\delta$. It should be noted that the population inversion density ΔN is the difference in population density between the Stark levels, which are populated according to the Boltzmann distribution at thermal equilibrium. The fraction of the total population density N_2 residing in the upper laser level is denoted f_b, so that the actual population density is $N_b = f_b N_2$, where

$$f_b = \frac{g_b \exp\left(-\Delta E_{2b}/k_B T\right)}{Z_2} \tag{2.10}$$

Here, k_B is Boltzmann's constant, T is the temperature and

$$Z_2 = \sum_{i=1}^{m} g_i \exp\left[-\Delta E_{2i}/k_B T\right] \tag{2.11}$$

is the partition function of level 2. The energy difference between sublevel i and the lowest sublevel within the manifold is denoted ΔE_i and g_i is the degeneracy of sublevel i. Similarly, the fraction of the total population density N_1 in the lower laser level is denoted f_a and the actual population density is consequently $N_a = f_a N_1$. Thus, the population inversion density in Eq. 2.9 is given by $\Delta N = N_b - N_a$.

Since there is a non-negligible fraction of the ground-state population density residing in the lower laser level, this gives rise to reabsorption effects, i.e. laser photons produced in the stimulated emission process are absorbed by the ions in the lower laser level which are then excited to the absorption band, instead of contributing to the laser photon amplification in the cavity. This effect is implicitly taken care of in the above formulated rate equations.

2.4 Energy-transfer upconversion

It has previously been shown[8-13] that energy-transfer upconversion (ETU) is a detrimental effect in Nd-doped lasers. This effect involves the ions residing in the upper laser level, where two nearby ions interact in an upconversion process. One ion relaxes down to a lower lying energy state and transfers its energy to the other ion, which is thereby raised (upconverted) to a higher energy state. Consequently, ETU reduces the population of the upper laser level and thus the population inversion, which in turn degrades the overall laser performance.

Here, it is considered that the decay rate via multiphonon processes from the energy states involved in the ETU process is much faster than the life-time of the upper laser level. The net effect is that only one excited ion is removed from the upper laser level by each upconversion process, since the upconverted ion will decay rapidly back to the upper laser level.

Including ETU effects in the modelling of the laser system above, modifies the rate equation for the upper laser level according to

$$\frac{dN_2}{dt} = -\frac{dN_1}{dt} = R_p - \frac{N_2}{\tau_2} - c_0\sigma_{21}\Delta N\phi - WN_2^2 \qquad (2.12)$$

where W is the so-called upconversion rate parameter which has the value $2.8 \cdot 10^{-22}\,m^3 s^{-1}$ for Nd:YAG[8]. The main consequences of ETU are heat generation and reduced available gain.

2.5 Passive Q-switching

In many applications, high output power is advantageous. One way of achieving high peak power lasers is by compressing the power generated in a laser cavity into short, energetic pulses. A widely used technique for realising these pulses is the so-called Q-switching technique[14]. This technique is based on the concept of modulating the losses inside the laser cavity, thereby modulating the ratio of the stored energy to the loss per cycle, i.e. the Q-value. The modulated loss can be pictured as a shutter inside the cavity, which is either closed or open. If the shutter is closed, laser action is prevented and the population inversion can continue to build up as the laser crystal is pumped continuously. When the shutter opens, the laser will exhibit a gain that greatly exceeds the losses. The stored energy may then be released in the form of a short and intense light pulse.

A compact and practical way of Q-switching solid-state lasers is to use saturable absorbers in the laser cavity[15]. This kind of Q-switching is passive, since no external driving sources are needed. A saturable absorber consists of a material that absorbs at the laser wavelength and becomes almost transparent for a low incident light intensity, thus behaving as a variable loss in the laser cavity. As the laser medium is pumped, the energy in the cavity builds up and approaches the threshold condition despite the extra loss introduced by the absorber. A weak resonating field begins to grow in the cavity, which successively becomes strong enough to bleach the saturable absorber. The bleaching occurs when the ground-state level of the absorber is depleted. However, this bleaching can be incomplete and thus cause residual absorption losses in the saturable absorber. Another disadvantage of using saturable absorbers is timing jitter, which is connected to mechanical as well as temperature instabilities in the laser system.

In the 1 μm spectral region, Cr^{4+}:YAG is often chosen because of its large absorption cross-section and low saturable intensity at the laser wavelength. In addition, it has a high damage threshold and is photochemically and thermally stable. It also provides the possibility of a compact and simple laser cavity. The energy level system of the Cr^{4+}:YAG crystal is shown in Fig. 2.4. As Cr^{4+}-doped crystals are susceptible to excited state absorption (ESA)[16], a four-level model is used to analyse its performance as a Q-switch. Absorption of the laser wavelength takes place at the 1-3 transition as well as the ESA at the 2-4 transition and the corresponding absorption cross-sections are σ_{gs} and σ_{es}, respectively. The relaxation rate for the transitions 4-2 and 3-2 is fast, while the life-time of level 2 is $\tau_s = 4.1$ μs[17] for Cr^{4+}:YAG. Thus, only the ground level 1 and level 2 have non-negligible population densities, termed N_{s1} and N_{s2}. The total population density participating in transitions is N_{s0} and can be obtained from the following expression[17] (in accordance with Eq. 2.4)

$$T_0 = \exp\left(-N_{s0}\sigma_{gs}l_s\right) \tag{2.13}$$

where T_0 is the initial (small-signal) transmission and l_s is the thickness of the absorber crystal.

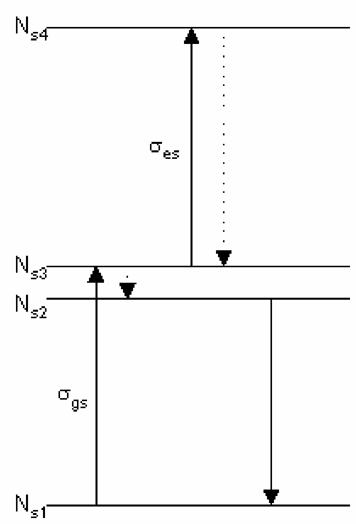

Fig. 2.4 The four-level model of the Cr^{4+}-doped saturable absorber.

To model a passively Q-switched laser, the coupled rate equations can be written as[16,18]

$$\begin{aligned}
\frac{dN_b}{dt} &= f_b R_p - \frac{N_b}{\tau_2} - f_b c_0 \sigma_{21} \Delta N \phi - \frac{W N_b^2}{f_b} \\
\frac{dN_a}{dt} &= -\frac{f_a}{f_b}\frac{dN_a}{dt} = -f_a R_p + \frac{f_a N_2}{\tau_2} + f_a c_0 \sigma_{21} \Delta N \phi + f_a W N_2^2 \\
\frac{d\phi}{dt} &= \frac{\phi}{t_r}\left(2\sigma_{21}\Delta N l_{cr} - 2\sigma_{gs} N_{s1} l_s - 2\sigma_{es}\left(N_{s0} - N_{s1}\right) l_s - \delta\right) \\
\frac{dN_{s1}}{dt} &= -\frac{dN_{s2}}{dt} = -c_0\,\sigma_{gs} N_{s1}\phi + \frac{\left(N_{s0} - N_{s1}\right)}{\tau_s}
\end{aligned} \tag{2.14}$$

where the temporal dynamics of the ground-state population density in the saturable absorber is governed by the last equation. In the equations above, it has been assumed that the size of the laser mode is equal in the laser crystal and in the saturable absorber so that the photon density in the same in all equations. By numerically simulating the temporal dynamics of the rate equation system above, the proper choice of initial transmission of the saturable absorber and transmission $T = 1-R$ of the output coupler can made in order to optimise the performance of the passively Q-switched laser. However, Degnan *et al*[19] extended the rate equations to include the effect of thermalization, i.e. single phonon-assisted transitions between non-degenerate Stark sublevels. Since the energy level differences in each multiplet lies within the highest phonon energies in Nd:YAG (the highest phonon energies are in the order of 700 cm^{-1} [20]), the thermalization transitions between non-degenerate Stark sublevels within either of the two multiplets is hence probable. By introducing the so-called thermalization time-constants τ_u and τ_l for the upper and lower laser multiplets, respectively, the rate equations are modified according to

$$\begin{aligned}
\frac{dN_b}{dt} &= f_b R_p - \frac{\left(N_b - f_b N_2\right)}{\tau_u} - \frac{N_b}{\tau_2} - c_0 \sigma_{21} \Delta N \phi - \frac{W N_b^2}{f_b} \\
\frac{dN_a}{dt} &= -f_a R_p - \frac{\left(N_a - f_a N_1\right)}{\tau_l} + \frac{f_a N_2}{\tau_2} + c_0 \sigma_{21} \Delta N \phi + f_a W N_2^2 \\
\frac{dN_2}{dt} &= R_p - \frac{N_2}{\tau_2} - c_0 \sigma_{21} \Delta N \phi - W N_2^2 \\
\frac{dN_1}{dt} &= -\frac{dN_2}{dt} = -R_p + \frac{N_2}{\tau_2} + c_0 \sigma_{21} \Delta N \phi + W N_2^2
\end{aligned} \tag{2.15}$$

where the equations for the photon population density and the ground-state population density in the saturable absorber are the same as in Eq. 2.14 and have hence been omitted. Here, N_2 and N_1 refer to the total population densities in the upper and lower lasing manifold, respectively. Within their respective multiplets, the population densities in the upper and lower Stark sublevels are denoted N_b and N_a, respectively.

The total number of photons in the cavity can be calculated from the following integral

$$\frac{d\Phi}{dt} = \iiint_{cavity} \frac{d\phi}{dt} dV \tag{2.16}$$

and is related to the output power as $P_{out} = Th\upsilon_L \Phi / t_r$ where ν_L is the laser frequency. In the simulations described in the following section, it has been used that the laser mode radius is smaller than the pump mode radius, so the integration in (2.16) is taken over the laser mode volume. Thus, the population density is given by $\phi = \Phi / V_L$, where $V_L = l_c^* \pi \omega_L^2 / 2$.

2.6 Q-switching performance of a quasi-three level Nd:YAG laser

The rate equations above (Eq. 2.15) can be applied to the passively Q-switched quasi-three level Nd:YAG laser described in Paper VI. The laser in question comprised a 15 mm long composite rod with a 5 mm long Nd:YAG crystal (doping level 1.1 atm%) and two undoped end-caps each 5 mm in length. The end-caps allow for a longitudinal heat flow when the crystal is heated by the pump, which reduces the thermal effects. Its diameter was 3 mm and it was directly watercooled to a temperature of 15 ˚C. A planar incoupling mirror and an outcoupling mirror with a ROC = 200 mm and transmission of 12 % were used, and the total cavity length was approximately 26 mm. A 0.5 mm thin uncoated Cr:YAG disc (employed in Brewster's angle to yield polarised laser output) with an initial transmission of 94 % was used as a saturable absorber. A fiber-coupled 808-nm diode (Limo GmbH) was used as the pump source, emitting up to 21 W from a 200 μm fibre with a NA of 0.22. For 7 W of absorbed power, the average output power was 0.94 W and the repetition frequency was 22 kHz whereas the pulse length was 16 ns as stated in Paper VI. These values correspond to a peak power of 2.9 kW and a pulse energy of 43 μJ.

In the simulations, the residual loss term was appreciated to L = 5.5 %, where additional absorption losses of the Cr:YAG crystal is taken into account. The additional absorption loss originating from water absorption is described in paper VI. Furthermore, the depolarisation loss[21] at this particular pump power is appreciated to 0.5 %. With this value of the loss factor and using that the cavity round-trip time is 0.26 ns, a cavity photon lifetime of 1.5 ns can be calculated. Thus, the pulse length is approximately 11 times longer than the cavity lifetime. The other input parameters used in the simulations were as follows: $N_0 = 1.5 \times 10^{20}$ cm^{-3} [22], n = 1.82, τ_2 = 230 μs [23], $\sigma_{21} = 5.1 \times 10^{-22}$ cm^{2} [24], τ_s = 4.1 μs [16], $\sigma_{gs} = 4.0 \times 10^{-18}$ cm^{2} [25] and $\sigma_{es} = 1.1 \times 10^{-18}$ cm^{2} [25]. The absorption coefficient α was determined experimentally to about 2.48 cm^{-1}, and given that the launched pump power was 9.85 W, the fraction of the pump absorbed in the crystal is then 71 %. A laser mode radius of 109 μm and an effective pump radius of 160 μm were used in the simulations. As for the thermalization time-constants, no exact data exist in the literature. The time-constant for the upper multiplet was appreciated to 3-5 ns in the article by Degnan *et al*[19], but for the lower multiplet no data could be found in the literature. If one considers that since the energy difference ΔE between the Stark levels in the lower multiplet is larger than in the upper multiplet, and assume that the time-constants follow the energy-gap law[26] $\tau^{-1} = \tau_0^{-1}\exp(-\gamma\Delta E)$ and use the slope parameter $\gamma = 5.24 \times 10^{-3}$ cm^{-1} [27], it can be deduced that the thermalization time-constant for the lower laser multiplets is approximately 11 times longer than for the upper laser multiplets. Considering that the pulse length was 16 ns, thermalization time-constants of these orders should have an impact on the performance of the laser. It was found that the numerical values got closest to the experimentally achieved results of peak power, repetition frequency and pulse length provided that thermalization time-constants of 5 ns for the upper laser level[19] and 55 ns for the lower laser level are assumed. However, the numerical simulation predicts a too short pulse length of 10 ns compared to the experimental value of 16 ns. Also the numerical values of peak power (3.09 kW), repetition frequency (30 kHz) and pulse energy (54 μJ) were too high.

Nevertheless, when no thermalization effects are taken into account, i.e. Eq (2.14) is used instead of Eq. (2.15), the numerical values do not even get close to the experimental results for any values of the input parameters. In general, the Q-switching model without thermalization predicts too short pulse lengths and much too high peak powers. Using the same input parameters as given above but neglecting thermalization would result in a pulse length of 6 ns and a peak power of 22 kW.

To see how thermalization and also upconversion effects influenced the pulse characteristics, numerical simulations were carried out with using Eq. 2.15 and Eq. 2.14, using the same input parameters and setting W = 0 in order to neglect upconversion. The result is presented in Fig. 2.5. The effect of the thermalization is that the pulse dynamics includes several peaks instead of just one, as in the two lower graphs of Fig. 2.5. The reason for this behaviour is nontrivial, but it can be understood that thermalization modulates the population inversion and thus the pulse dynamics through the thermalization terms in Eq. 2.15. As for the upconversion, it does not seem to influence the pulse characteristics to a greater extent when thermalization is taken into account, but it has a large effect on the peak power when thermalization is neglected, as can be seen when comparing the two lower graphs.

Although the numerical simulations can not exactly predict the experimental results, I also investigated how different transmission of the outcoupling mirror for the laser and the initial transmission of the saturable absorber would affect the laser characteristics. The results of the simulations are presented in Fig. 2.6-2.9. As expected, a lower initial transmission of the saturable absorber yields a higher peak power combined with a shorter pulse length and a lower value of the repetition frequency. However, these demands must be balanced with the risk of damage of the coatings on the crystals in the laser cavity. In addition, the reabsorption losses inherent in quasi-three level lasers impose limits on the optimum choice of initial transmission as well as the output coupler transmission.

The effective radius is also a crucial parameter when designing Q-switched lasers. In Fig. 2.10-2.13, the dependence on the effective radius of the pump beam is presented. As a lower initial transmission of the saturable absorber acts as larger round-trip loss for the Q-switched laser during population-inversion build-up, this sets demands on the size of the focused pump beam waist. As seen from Fig. 2.10, the optimum peak power occurs for a smaller effective pump beam radius when the initial transmission is lower.

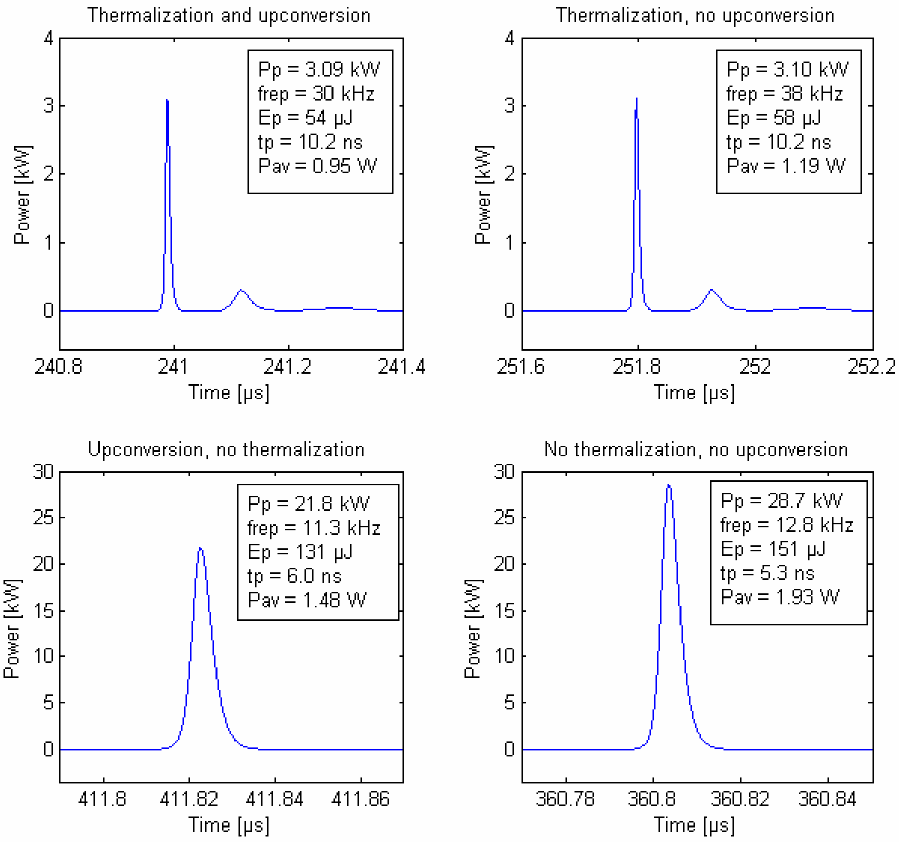

Fig. 2.5 Pulse characteristics with and without thermalization and upconversion.

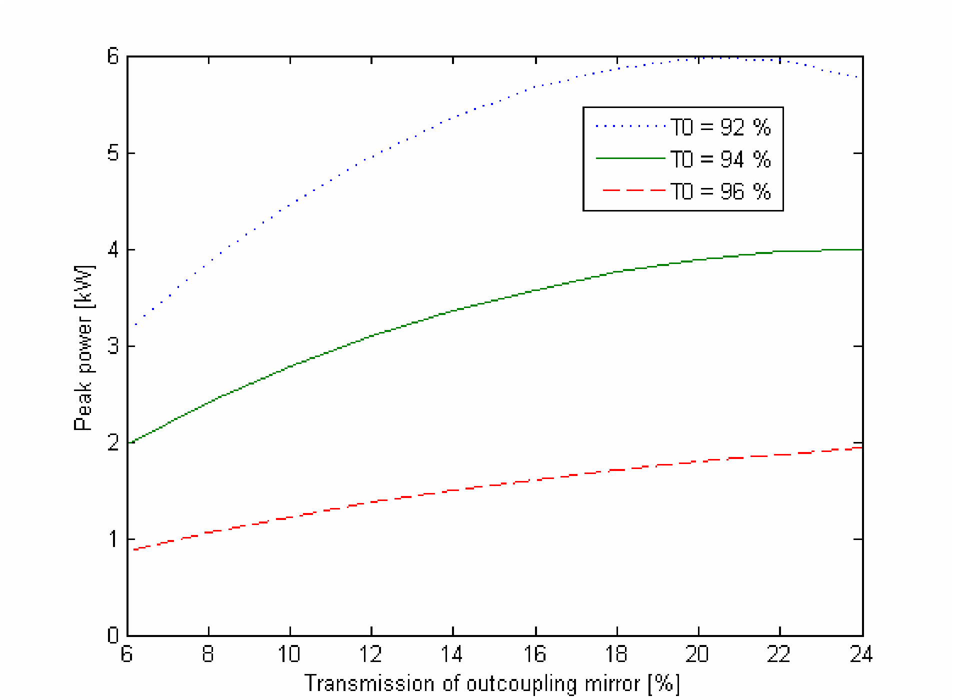

Fig. 2.6 The peak power as function of transmission of outcoupling mirror for different values of the initial transmission of the Cr:YAG crystal.

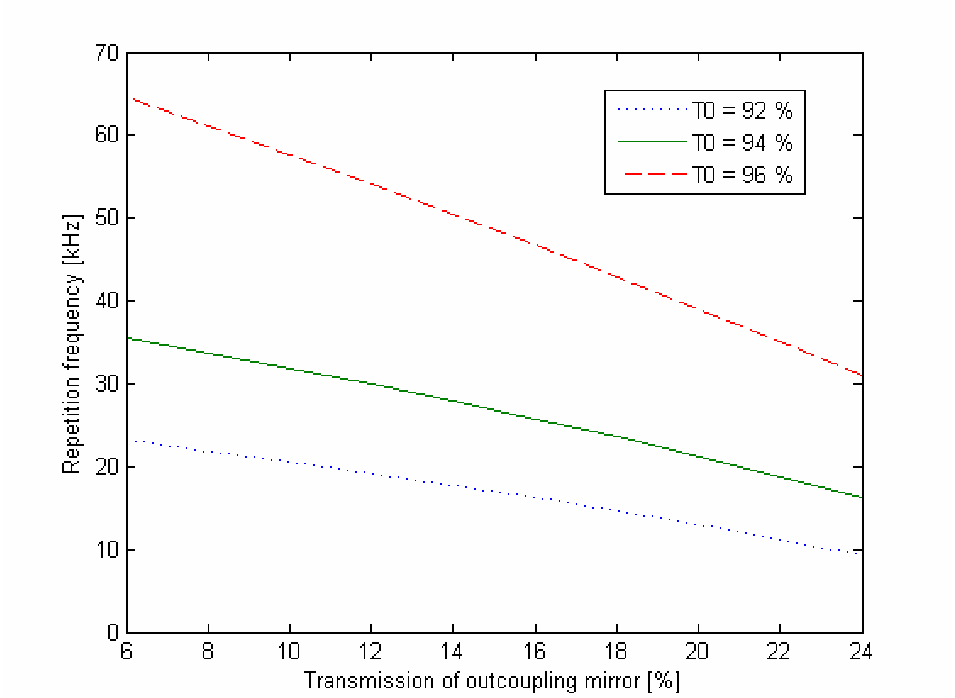

Fig. 2.7 The repetition frequency as function of transmission of outcoupling mirror for different values of the initial transmission of the Cr:YAG crystal.

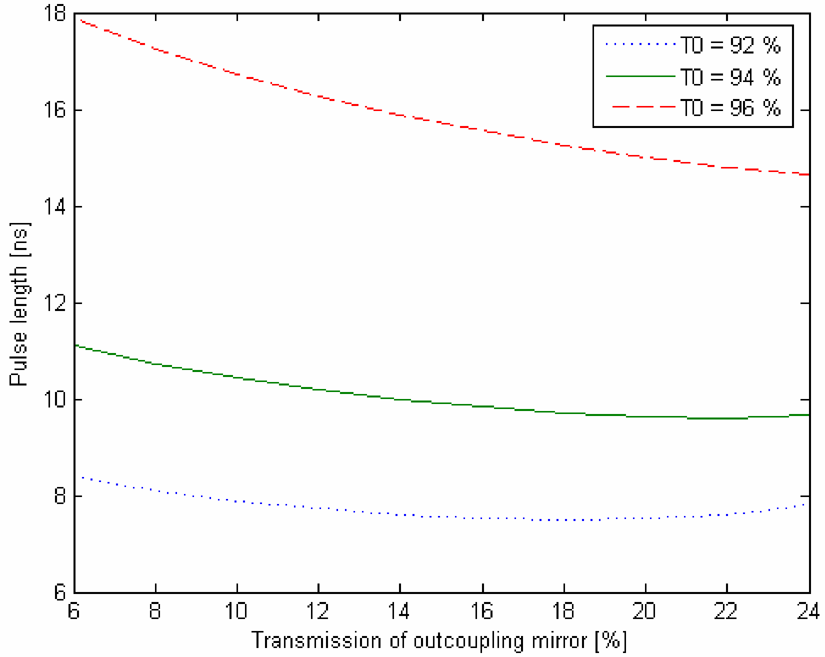

Fig. 2.8 The pulse length as function of transmission of outcoupling mirror for different values of the initial transmission of the Cr:YAG crystal.

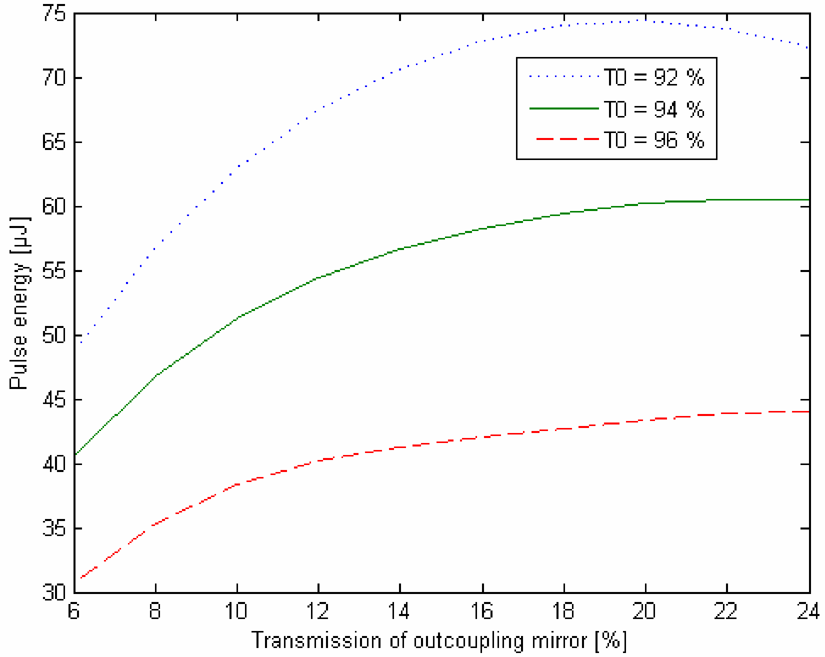

Fig. 2.9 The pulse energy as function of transmission of outcoupling mirror for different values of the initial transmission of the Cr:YAG crystal.

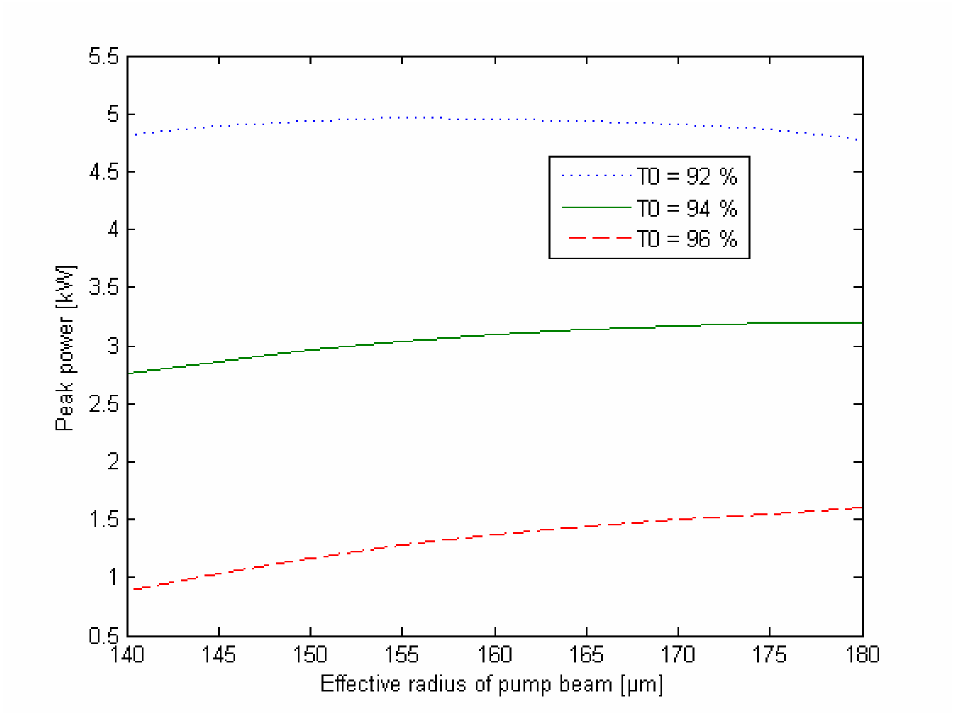

Fig. 2.10 The peak power as function of the effective radius of the pump beam for different values of the initial transmission of the Cr:YAG crystal.

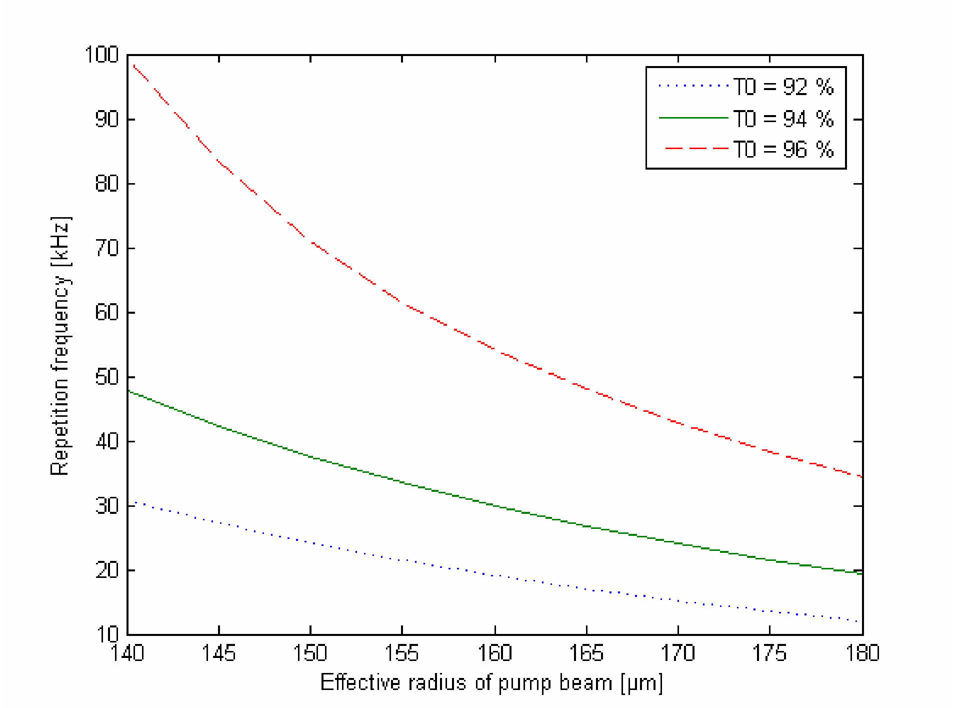

Fig. 2.11 The repetition frequency as function of the effective radius of the pump beam for different values of the initial transmission of the Cr:YAG crystal.

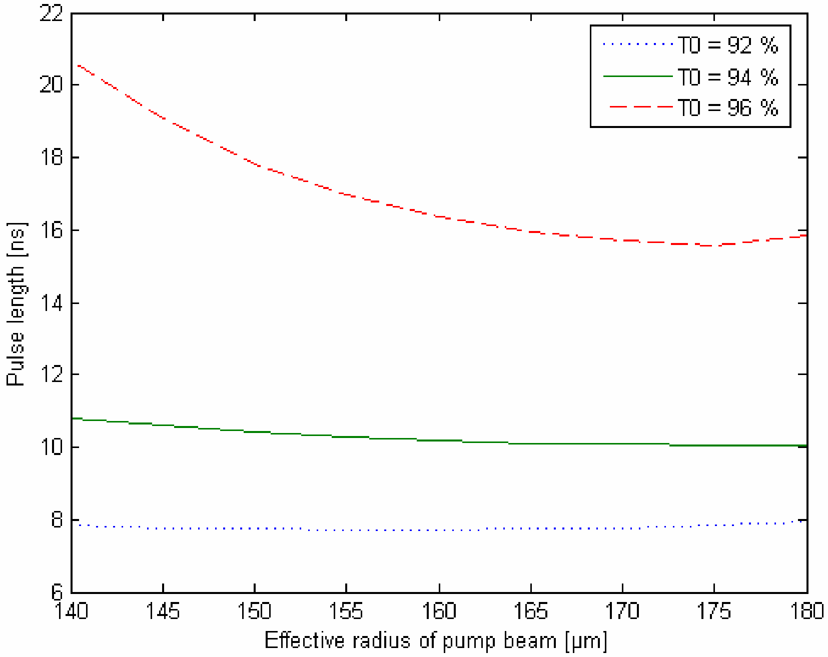

Fig. 2.12 The pulse length as function of the effective radius of the pump beam for different values of the initial transmission of the Cr:YAG crystal.

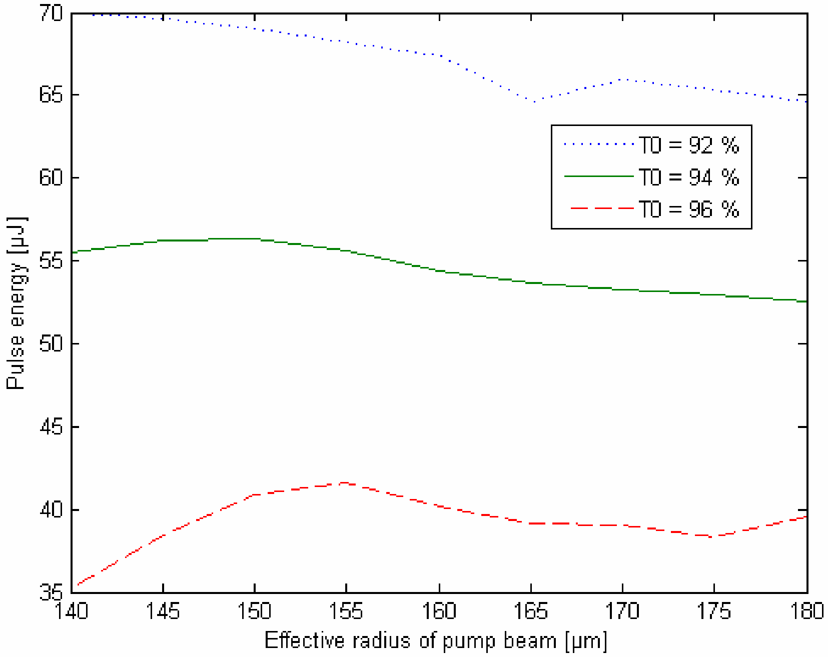

Fig. 2.13 The pulse energy as function of the effective radius of the pump beam for different values of the initial transmission of the Cr:YAG crystal.

Chapter 3

Nonlinear Optics

What is nonlinear optics really? As opposed to linear optics, where

- the optical properties of the medium is unchanged by the optical intensity
- the frequency of light is not altered while it traverses the medium

nonlinear optics has the following important consequences:

- the optical properties (refractive index, absorption, etc) *can* in fact change due to the optical intensity
- the frequency of light *can* be altered while it traverses the medium

It should here be understood that by light waves are meant electromagnetic waves having frequencies ranging from the infrared via the visible into the ultraviolet part of the spectrum. It should also be noted that nonlinear interaction between light waves can only take place within a medium, where a nonlinear polarisation can be induced. Then, the only assumption is that the optical intensity of the electromagnetic wave is high enough, which is expressed by the constitutive relation below.

3.1 The Constitutive Relation

A simple but powerful model of how light interacts with media is given by the following: Suppose that the media is constituted by a positive nucleus surrounded by a negatively charged electron cloud having the same centre as the nucleus. This is the equilibrium condition, and no net polarisation is present in the material. If a light wave is incident on the media, this will bring the charges into oscillation, where the electrons move in the opposite direction of the field whereas the nucleus moves in the same direction of the field. Since the nucleus is much heavier than the electrons, the induced oscillation will be more pronounced for the electrons. A spatial separation of the centres of positive and negative charge is caused, creating an electric dipole. Thus, an electric polarisation $\boldsymbol{P}$ is induced in the material, in the direction of the applied field $\boldsymbol{E}$. In linear optics, this is mathematically described by

$$\boldsymbol{P} = \varepsilon_0 \boldsymbol{\chi} \cdot \boldsymbol{E}\,, \tag{3.1}$$

where ε_0 is the permittivity in vacuum and $\boldsymbol{\chi}$ denotes the susceptibility tensor. For light waves of high intensities, this equation does not hold anymore since the dipoles will not be able to follow the oscillation of the applied field in a linear way, but instead exhibit a nonlinear response. This is formally expressed as

$$\boldsymbol{P} = \varepsilon_0 \boldsymbol{\chi}(\boldsymbol{E}) \cdot \boldsymbol{E} \,, \tag{3.2}$$

stating that the susceptibility $\boldsymbol{\chi}$ is dependent on the applied field. Equation (3.2) is the constitutive relation which governs the nonlinear process. In case that the deviation from the linear description is small, Equation (3.2) can be expanded in a perturbation series[28-32],

$$\boldsymbol{P} = \varepsilon_0 (\boldsymbol{\chi}^{(1)} \cdot \boldsymbol{E} + \boldsymbol{\chi}^{(2)} \cdot \boldsymbol{E}^2 + \boldsymbol{\chi}^{(3)} \cdot \boldsymbol{E}^3 + \ldots) = \boldsymbol{P}^{(L)} + \boldsymbol{P}^{(NL)} \,, \tag{3.3}$$

where $\boldsymbol{\chi}^{(2)}$ and $\boldsymbol{\chi}^{(3)}$ etc. are the second order, third order, etc. nonlinear susceptibility tensors, which rapidly decrease in magnitude for higher orders. This thesis will focus on nonlinear processes of second order, described by $\boldsymbol{P}^{(2)} = \varepsilon_0 \boldsymbol{\chi}^{(2)} \cdot \boldsymbol{E}^2$ where $\boldsymbol{\chi}^{(2)}$ is a tensor of third rank consisting of 27 elements. A more compact tensor notation is applicable if intrinsic permutation - and Kleinman symmetries[33] hold, denoted the ***d***-tensor. This tensor is defined by the relation $2\boldsymbol{d}_{\mu m} = \boldsymbol{\chi}^{(2)}_{\mu\alpha\beta}$ and contains only 18 independent elements, which further simplifies the calculations. The indices given in the relation are connected to the polarisation directions *x*,*y*, and *z* of the applied field, and the index *m* is a contraction of the index pair $\alpha\beta$[28]. In matrix form, the second-order polarisation $\boldsymbol{P}^{(2)}_{\omega_3}$ can then be expressed as

$$\begin{bmatrix} (P^{(2)}_{\omega_3})_x \\ (P^{(2)}_{\omega_3})_y \\ (P^{(2)}_{\omega_3})_z \end{bmatrix} = 2\varepsilon_0 K \begin{bmatrix} d_{11} & d_{12} & d_{13} & d_{14} & d_{15} & d_{16} \\ d_{21} & d_{22} & d_{23} & d_{24} & d_{25} & d_{26} \\ d_{31} & d_{32} & d_{33} & d_{34} & d_{35} & d_{36} \end{bmatrix} \begin{bmatrix} \left(E_{\omega_1}\right)_x \left(E_{\omega_2}\right)_x \\ \left(E_{\omega_1}\right)_y \left(E_{\omega_2}\right)_y \\ \left(E_{\omega_1}\right)_z \left(E_{\omega_2}\right)_z \\ \left(E_{\omega_1}\right)_y \left(E_{\omega_2}\right)_z + \left(E_{\omega_2}\right)_y \left(E_{\omega_1}\right)_z \\ \left(E_{\omega_1}\right)_x \left(E_{\omega_2}\right)_z + \left(E_{\omega_2}\right)_x \left(E_{\omega_1}\right)_z \\ \left(E_{\omega_1}\right)_x \left(E_{\omega_2}\right)_y + \left(E_{\omega_2}\right)_x \left(E_{\omega_1}\right)_y \end{bmatrix} . \tag{3.4}$$

It should here be understood that the frequencies involved in the nonlinear process are denoted ω_1, ω_2 and ω_3 where the latter is the sum of the two first. The constant *K* is a degeneracy factor and is equal to ½ for second harmonic generation and optical rectification, and for all other second-order parametric processes it is equal to one.

Simplifications of the ***d***-tensor can be made when taking spatial symmetries of the nonlinear optical medium into account. Depending on which particular crystal class the medium belongs to, some elements of the ***d***-tensor are equal and other vanish, so the number of independent elements is reduced.

3.2 The Coupled Wave-Equations

Maxwell's equations give a general description of the propagation of electromagnetic waves. Common to all nonlinear optical media treated here is that they are dielectrics, i.e. there is no free charge in the media and the magnetic permeability is low. From Maxwell's equations, it is then possible to derive the wave equation:

$$\nabla^2 \boldsymbol{E}(r,t) - \frac{1}{c_0^2}\frac{\partial^2 \boldsymbol{E}(r,t)}{\partial t^2} = \mu_0 \frac{\partial^2 \boldsymbol{P}(r,t)}{\partial t^2} \tag{3.5}$$

where c_0 is the velocity of light and μ_0 is the magnetic permeability in vacuum. The right-hand side of Eq. 3.5 acts as a source term for the electric field $\boldsymbol{E}$, at the same time as the polarisation $\boldsymbol{P}$ induced by the $\boldsymbol{E}$ in the dielectric medium is described as the response of the medium to an incoming wave. Instead of using the instantaneous fields, it is practical to use a Fourier description of $\boldsymbol{E}$ and $\boldsymbol{P}$, and by considering infinite plane, quasi-monochromatic fields propagating in the z-direction, they can be written as

$$\begin{aligned}\boldsymbol{E}(r,\omega) &= \frac{1}{2}\sum_{\omega_\sigma}\left[\boldsymbol{E}_{\omega_\sigma}(r,\omega-\omega_\sigma)\exp\left(ik_\sigma z\right)+c.c.\right]\\ \boldsymbol{P}(r,\omega) &= \frac{1}{2}\sum_{\omega_\sigma}\left[\boldsymbol{P}_{\omega_\sigma}(r,\omega-\omega_\sigma)\exp\left(ik_\sigma z\right)+c.c.\right]\end{aligned} \tag{3.6}$$

where the envelopes have some limited extent around the carrier frequency ω_σ. The complex conjugates are added since $\boldsymbol{E}(r,t)$ and $\boldsymbol{P}(r,t)$ are real functions. The wavenumber k_σ is given by $k_\sigma = \omega_\sigma n_\omega / c_0$, where n_ω is the refractive index at the carrier frequency. Performing the Fourier transform on the wave-equation yields

$$\nabla^2 \boldsymbol{E}(r,\omega) + \frac{\omega_\sigma^2}{c_0^2}\left(1+\boldsymbol{\chi}^{(1)}\right)\cdot \boldsymbol{E}(r,\omega) = -\mu_0 \omega_\sigma^2 \boldsymbol{P}^{(NL)}(r,\omega)\,. \tag{3.7}$$

Here, the linear part of the polarisation has been moved to the left-hand side of the equation, thereby defining the dielectric constant as $\boldsymbol{\varepsilon} = 1+\boldsymbol{\chi}^{(1)}$. This constant is related to the refractive index as $\boldsymbol{n} = \mathrm{Re}\left(\sqrt{1+\boldsymbol{\chi}^{(1)}}\right)$, while the optical absorption is related to the imaginary part of the dielectric constant. The envelope $\boldsymbol{E}_{\omega_\sigma}(r,\omega-\omega_\sigma)$ of the electric field varies as the wave propagates through the medium, but if the variation is slow over a distance of one wavelength, it is possible to make an approximation commonly termed as the "slowly varying envelope approximation" (SVEA):

$$\left|\frac{\partial^2 \mathbf{E}_{\omega_\sigma}}{\partial z^2}\right| << \left|k_\sigma \frac{\partial \mathbf{E}_{\omega_\sigma}}{\partial z}\right| \tag{3.8}$$

This approximation is most often valid in nonlinear optics, and the wave-equation is then reduced to a differential equation of first order:

$$\frac{\partial \mathbf{E}_{\omega_\sigma}}{\partial z} = \frac{i\mu_0 \omega_\sigma^2}{2k_\sigma}\boldsymbol{P}^{(NL)}\exp\left(-ik_\sigma z\right) \tag{3.9}$$

This equation must be satisfied by all the quasi-monochromatic waves present in the nonlinear medium, whether applied or generated. For the case of second-order nonlinear processes, three different waves are involved in the parametric interaction. By using Eq. 3.4, the induced nonlinear polarisation can then be written in scalar form as

$$P^{(NL)} = \varepsilon_0 K d_{eff} E_{\omega_1} E_{\omega_2} \exp\left(i\left(k_1 + k_2\right)z\right) \tag{3.10}$$

where the effective nonlinear coefficient d_{eff} is derived from the ***d***-tensor in Eq. 3.4 taking the polarisations of the interacting fields into account. By inserting the expression in (3.10) in the first-order wave equation (3.9), the result is a set of coupled equations,

$$\begin{aligned}
\frac{\partial E_{\omega_1}}{\partial z} &= \frac{i\omega_1^2}{k_1 c_0^2} K d_{eff} E_{\omega_\sigma} E_{\omega_2}^* \exp(i\Delta k z) \\
\frac{\partial E_{\omega_2}}{\partial z} &= \frac{i\omega_2^2}{k_2 c_0^2} K d_{eff} E_{\omega_\sigma} E_{\omega_1}^* \exp(i\Delta k z) \\
\frac{\partial E_{\omega_\sigma}}{\partial z} &= \frac{i\omega_\sigma^2}{k_\sigma c_0^2} K d_{eff} E_{\omega_1} E_{\omega_2} \exp(-i\Delta k z)
\end{aligned} \tag{3.11}$$

This set of equations describes how the waves couple to each other via the induced polarisation as they propagate through the nonlinear media. The energy conservation principle is obeyed through the condition $\omega_\sigma = \omega_1 + \omega_2$, whereas the phase mismatch between the interacting waves is expressed by $\Delta k = k_\sigma - k_1 - k_2$. With the coupled wave-equations as a starting-point, second-order nonlinear processes can be described within the quasi-monochromatic plane-wave approximation.

3.3 Second Harmonic Generation and Sum Frequency Generation

In the general description of second-order nonlinear processes, several types of interactions can take place, two of them being second harmonic generation and sum frequency generation. Other processes are difference frequency mixing, optical rectification, Pockel’s effect and optical parametric amplification (OPA). They all belong to the group of nonlinear interactions where two incident waves generate a new wave via the nonlinear media. The other type of nonlinear interaction involves a single incident wave (often called the pump wave) which then generates two new waves in the nonlinear media. The process optical parametric generation (OPG) belongs to this type. It is often useful to describe all these processes within the photon picture, where the first group of processes involves two photons that interact to create a new photon whereas the other group is characterised by one photon being split up in two new photons. In this thesis, only second harmonic generation and sum frequency generation will be considered in the following chapters. A graphical presentation of sum frequency generation is shown in Fig. 3.1.

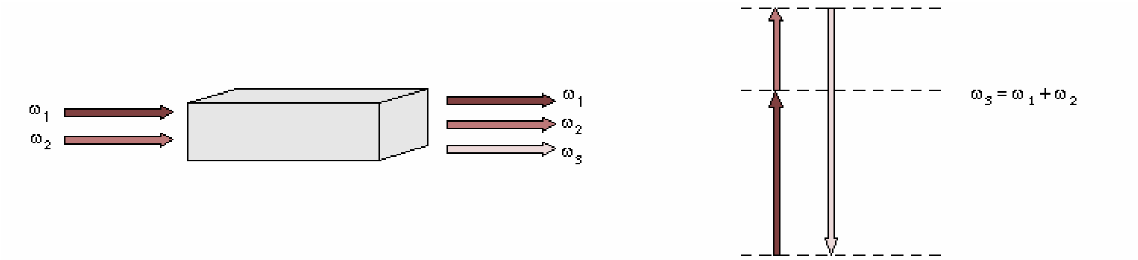

Fig. 3.1 Sum-frequency generation depicted as a three wave interaction in a nonlinear media and described within the photon picture.

3.3.1 Plane Wave Analysis

Using the coupled wave equations (Eq. 3.11), it is possible to derive an expression for the intensity of the generated wave. For the case of sum frequency generation where two waves of frequencies ω_1 and ω_2 add up to create a new wave at frequency ω_3, the equations are identical to Eq. 3.11, given that $\omega_\sigma = \omega_3$. For notational convenience, the optical fields E_{ω_1}, E_{ω_2}, and E_{ω_3} are hereafter termed E_1, E_2 and E_3. Assuming that the conversion from the two fundamental waves to the generated wave is low, it is a straight-forward procedure to analytically solve these equations. As an example, consider the case of a nonlinear crystal of length L and having a nonlinear coefficient d_{eff}, where the latter parameter is given by the crystal symmetry and the polarisation of the interacting waves. Neglecting depletion of E_1 and E_2, i.e. $E_1(L) = E_1(0)$ and $E_2(L) = E_2(0)$, the remaining equation is

$$\frac{\partial E_3}{\partial z} = \frac{i\omega_3^2}{k_3 c_0^2} d_{eff} E_1(0) E_2(0) \exp(-i\Delta k z). \tag{3.12}$$

By integrating over the crystal length and invoking the intensities given by $I_i = \frac{1}{2}\varepsilon_0 c_0 n_i |E_i|^2$, the following expression is obtained:

$$I_3 = \frac{8\pi^2 d_{eff}^2 L^2 I_1 I_2}{n_1 n_2 n_3 \varepsilon_0 c_0 \lambda_3^2} sinc^2\left(\frac{\Delta k L}{2}\right) \tag{3.13}$$

The function *sinc(x)* is defined as *sin(x)/x* and the refractive indices n_i are taken at their respective frequency ω_i. The wavelength λ_3 is related to the generated frequency as $\omega_3 = 2\pi c_0 / \lambda_3$. From Eq. 3.13, it can be seen that the degree of conversion from the two fundamental intensities to the generated intensity I_3 is highly dependent on the phase mismatch Δk. In Fig. 3.2, the $sinc^2$-dependence is plotted, showing that for $\Delta k \neq 0$, the conversion efficiency is decreased. If, on the other hand it can be arranged so that $\Delta k = 0$, the generated intensity I_3 will increase rapidly for an increased crystal length and a high nonlinear coefficient.

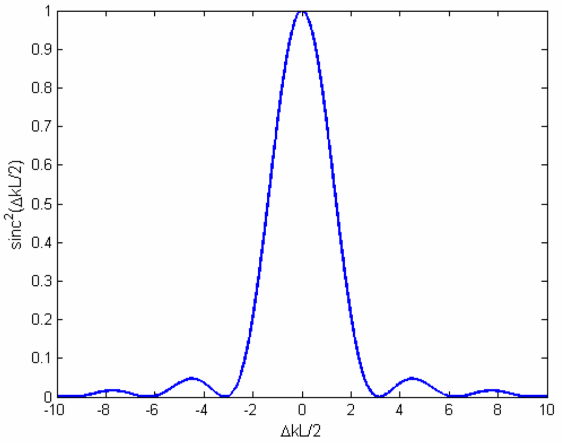

Fig. 3.2 The sinc^2-function.

It should be noted that for depletion of one or both of the fundamental waves, the expression for the intensity I_3 will be different. For simplicity, if the case of second harmonic generation is considered, the counterpart of Eq. 3.13 will be

$$I_3 = \frac{2\pi^2 d_{eff}^2 L^2 I_1^2}{n_1^2 n_3 \varepsilon_0 c_0 \lambda_3^2} sinc^2\left(\frac{\Delta kL}{2}\right) \tag{3.14}$$

where it has been used that $\omega_1 = \omega_2$. Assuming that phase matching is achieved, $\Delta k = 0$, the conversion efficiency is then written as

$$\eta_{SHG} = \frac{I_3}{I_1} = \frac{2\pi^2 d_{eff}^2 L^2}{n_1^2 n_3 \varepsilon_0 c_0 \lambda_3^2} I_1 \tag{3.15}$$

From a mathematical point of view, there is actually nothing that prevents the conversion efficiency from exceeding one in this expression, which is of course physically untrue. If depletion of the fundamental wave is taken into account, the task is then to solve the coupled wave equations in Eq. 3.11. This can be done analytically[32], and the resulting conversion efficiency is then

$$\eta_{SHG,depl} = \tanh^2\left(\sqrt{\frac{2\pi^2 d_{eff}^2 L^2 I_1}{n_1^2 n_3 \varepsilon_0 c_0 \lambda_3^2}}\right) \tag{3.16}$$

which cannot exceed one, as expected.

3.3.2 Gaussian Beams

Although the plane wave analysis is a very powerful tool for describing second order nonlinear processes, real-life beams have a spatial confinement and do not act like unbounded plane waves. Thus, the analysis has to be extended to actual, often Gaussian, beams in order to be more accurate. Examining the expressions for conversion efficiency in the previous section, it is obvious that a tightly confined beam is desired since intensity is power per unit area. In addition, a long length of the nonlinear crystal is important according to the derived conversion efficiencies. Unfortunately, there is a trade-off between tight confinement and long interaction length because all beams exhibit diffraction. This optimisation problem has been addressed by Boyd and Kleinman in the case of second harmonic generation, and later for sum frequency generation by Guha and Falk. In both cases, the analysis involved circular Gaussian beams, focused in a material exhibiting walk-off. Only the results are stated here. For second harmonic generation, the generated power is given by[35]

$$P_3 = \frac{16\pi^2 d_{eff}^2}{\varepsilon_0 c_0 \lambda_1^3 n_3 n_1} P_1^2 L \, h(\xi, B, \sigma) \tag{3.17}$$

where *h(ξ,B,σ)* is the so-called focusing function, see Fig. 3.2. The parameters *ξ*, *B,* and *σ* are defined as

$$\begin{aligned} \xi &= L/b \\ B &= \rho\sqrt{Lk_1}/2 \\ \sigma &= b\Delta k/2 \end{aligned} \tag{3.18}$$

Here, the so-called confocal parameter is defined as $b = 2\pi n_1 \omega_0^2/\lambda_1$ and the walk-off angle ρ is defined as the angle between the generated second-harmonic wave relative to the fundamental wave. From Eq. 3.17, it can then be concluded that maximising the generated power is a question of optimising the focusing function *h(ξ,B,σ)* with respect to the focusing parameter *ξ*, the walk-off parameter *B* and the phase-matching parameter *σ*.

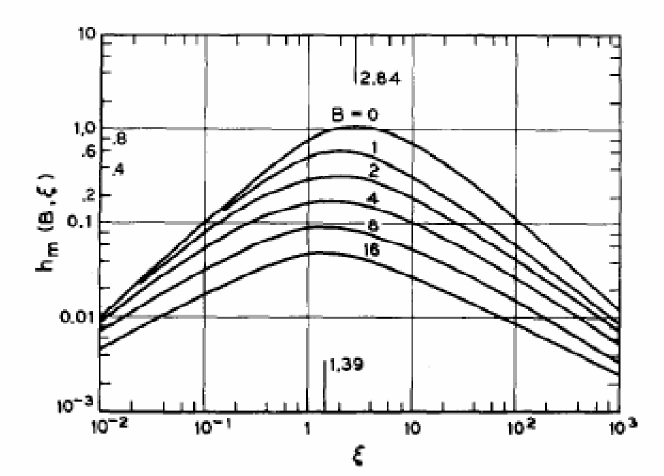

Fig. 3.2 The Boyd-Kleinman focusing function.

The counterpart to Eq. 3.17 for the more general case of sum frequency generation is given by the following expression[36]:

$$P_3 = \frac{32\pi^2 d_{eff}^2}{\varepsilon_0 c_0 n_3^2 \lambda_1 \lambda_2 \lambda_3} P_1 \, P_2 \, L \, h(\xi, B, \sigma) \tag{3.19}$$

In general, maximum conversion efficiency occurs when the two beams involved in the interaction have different confocal parameters.

3.4 Phase-Matching

A crucial parameter for the nonlinear conversion efficiency is the value of the phase mismatch. Only nonlinear processes for which $\Delta k \approx 0$, can have significant efficiency. The condition $\Delta k = 0$ expresses that the waves that take part in the nonlinear process travel at the same phase velocity. This is generally not the case because of dispersion in optical materials. In SHG, this has the consequence that the generated second harmonic wave will drift out of phase with the driving polarisation. After a certain distance $L_c = |\pi/\Delta k|$, called the coherence length, they will be out of phase by 180˚, and the intensity of the second harmonic wave will begin to flow back to the fundamental wave. There will thus be an oscillation in second harmonic power along the nonlinear crystal, instead of solely converting intensity from the fundamental wave to the second harmonic. The coherence length is typically only a few micrometers long, whereas efficient nonlinear generation is achieved for crystals that are considerably longer, typically several millimetres. Hence special techniques will have to be used in order to overcome this obstruction. In practice, there exist two methods for achieving phase-matching. One of them is birefringent phase-matching, based on the utilisation of the natural birefringence of some materials. The other is called quasi phase-matching, based on methods where the nonlinear material is artificially structured in order to introduce an 180˚ phase shift of the locally generated wave every coherence length.

3.4.1 Birefringent Phase-Matching

When a nonlinear process showed efficient frequency conversion for the first time, birefringent phase-matching was used[37,38]. It is still the most common method to achieve phase-matching. The method is exploiting the natural birefringence of some materials, where the refractive index is dependent upon the polarisation of the incoming wave(s). It is thereby possible to compensate for the refractive index difference between the interacting waves. As an example, second harmonic generation in potassium niobate (KN) is considered. The condition that has to be fulfilled is then

$$\Delta k = k_{SH} - 2k_F = \frac{2\omega}{c_0}\left(n_{SH} - n_F\right) = 0 . \tag{3.20}$$

The nonlinear material KN is a biaxial crystal, thus having three principal axes *a*, *b* and *c* with their respective refractive indices, n_a, n_b and n_c. By letting the polarisation of the second harmonic lie along the fast axis c, and propagate the fundamental in the a-b plane, the phase-matching condition can be fulfilled, or $n_{SH} - n_F = 0$. The refractive index experienced by the fundamental wave is then given by

$$\frac{1}{n_{a-b}(\theta)} = \sqrt{\frac{\sin^2\theta}{n_a^2} + \frac{\cos^2\theta}{n_b^2}} \tag{3.21}$$

where the angle θ is measured from the *a*-axis to the propagation direction. A graphical presentation of this is shown in Fig. 3.3. As the refractive index experienced by the second harmonic will the same for all propagation directions (independent of θ), it corresponds to the circle $n_c(2\omega)$ in Fig. 3.3, whereas the relation for $n(\theta)$ describes an ellipse in the *a*-*b* plane. For a specific propagation direction given by the angle θ, phase-matching between the fundamental and the second harmonic wave will be obtained, i.e. $n_{a\text{-}b}(\theta)=n_c$.

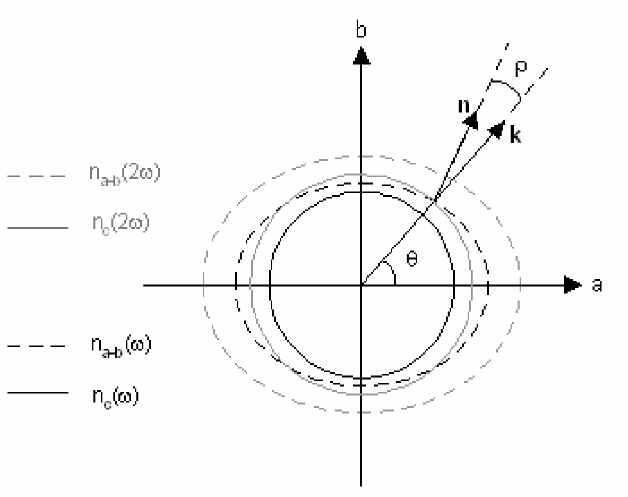

Fig. 3.3 Birefringent phasematching in KN.

There is however a complication to this angle tuning technique, because of Poynting vector walk-off[39]. The power flow of the wave, represented by the Poynting vector, will be normal to the refractive index curve and can thus differ from the propagation vector, depending on the polarisation of the propagating wave. This deviation is termed the walk-off angle ρ, given by the following expression[4]

$$\tan\rho = \frac{\tan\theta\left(\dfrac{n_b^2}{n_a^2}-1\right)}{1+\dfrac{n_b^2}{n_a^2}\tan^2\theta} \quad . \tag{3.22}$$

This has the effect that the spatial overlap between the fundamental beam and the second harmonic beam will be reduced after a certain propagation distance, and it thus follows that the conversion efficiency will be lowered because of the shorter possible interaction length. In addition, this prevents tight focusing since a smaller beam waist separates faster than a large one which will limit the second harmonic generation even further.

From Eq. 3.22 it can be deduced that the walk-off angle will be zero when the propagation direction lies along a principal axis. This is called non-critical phase-matching, which is advantageous since the acceptance angle $\Delta\theta$ for phase-matching will be larger compared to critical phase-matching. However, the propagation direction can not always be chosen along a principal axis but is limited to certain directions depending on the frequencies that should be phase-matched. Also, the highest possible nonlinear coefficient can not be chosen freely because of the limitations in choice of θ, and certain frequencies can not be efficiently phase-matched since the nonlinear coefficient is too low to be useful or even zero. Nevertheless, in some cases birefringent phase-matching is the remaining choice, e.g. in the generation of deep-UV light where very few nonlinear crystals are transparent in this part of the frequency spectrum.

3.4.2 Quasi-Phase Matching

Although quasi phase-matching was suggested for the first time in 1962[34,40], it was not until the early 1990's that this technique started to be useful in practice[39]. The reason for this lies in the technology itself: quasi phase-matching requires that the nonlinear material is artificially structured in order to introduce an 180° phase shift of the locally generated wave every coherence length. The coherence length is on the order of 3-7 μm, and this have to be done consistently over a distance of several millimetres, i.e. hundreds or thousands of coherence lengths. Thus, the quasi phase-matching technique had to await the advances in material technology.

One possible way of introducing this phase shift is by reversing the sign of d_{eff} every coherence length, as can be seen from Eq. 3.12. This means that d_{eff} is modulated in a periodic way according to[42]

$$d(z) = d_{eff} \sum_{m=-\infty}^{\infty} D_m \exp(iK_m z) \tag{3.23}$$

with a period of Λ, expressed by the so-called grating wave vector

$$K_m = \frac{2\pi m}{\Lambda}, \tag{3.24}$$

where m is an integer. Assuming second harmonic generation and integrating Eq. 3.12 over a certain interaction length L, will yield the following expression for the generated field

$$E_{2\omega} = \frac{i\omega E_\omega^2}{n_{2\omega} c_0} \int_0^L d(z) \exp(-i\Delta k' z) dz \tag{3.25}$$

where $\Delta k' = k_{2\omega} - k_\omega$ has been introduced for the wave vector mismatch. If $d(z)$ is set to zero outside the integration length L, the integral in (3.25) can be written as a Fourier transform with transform variables $\Delta k'$ and z. This transform then relates the wave vector mismatch to the modulated nonlinear coefficient along the direction of propagation. Obviously, maximum conversion efficiency will be obtained where this transform reaches a maximum. If the Fourier series in 3.23 is inserted in this expression, this will result in

$$E_{2\omega} = \frac{i\omega E_\omega^2 d_{eff}}{n_{2\omega} c_0} \int_0^L \sum_{m=-\infty}^{\infty} D_m \exp(i(K_m - \Delta k')z) dz \tag{3.26}$$

Thus, the integral is maximised when K_m is close to $\Delta k'$. This can be only be satisfied for one term in the Fourier series, with the corresponding Fourier coefficient

$$D_m = \frac{2}{m\pi} \sin(m\pi D) \tag{3.27}$$

where D is the duty cycle defined by l_+/Λ and l_+ is the length of the positive section of $d(z)$. The new effective nonlinear coefficient is then given by $d_{QPM} = D_m d_{eff}$ and the new phase-matching condition is then

$$\Delta k = k_{2\omega} - 2k_{\omega} - K_m = 0\,. \tag{3.28}$$

Phase-matched nonlinear interactions are then achieved by tailoring the proper grating vector with respect to the phase-mismatch $\Delta k'$. The nonlinear coefficient d_{QPM} is maximised if the argument of the sine-function is equal to $\pi/2$ or $3\pi/2$, and for optimum quasi phase-matching, where $m = 1$, this leads to $d_{QPM} = 2d_{eff}/\pi$. Thus, quasi phase-matching is achieved at the price of a small reduction in the conversion efficiency compared to perfect phase-matching. This can be seen in Fig. 2.4. Nevertheless, this drawback is outweighed by the possibility to noncritically phasematch any interaction within the transparency range of the nonlinear crystal in question. Also, access to the highest possible nonlinear coefficient in the ***d***-tensor is provided with this technique. For some crystals, for example in potassium titanyl phosphate (KTP), this is the d_{33} element which in birefringent phase-matching is not accessible since this would require that the fundamental and the second harmonic wave would have the same polarisation and thus the same phase velocity.

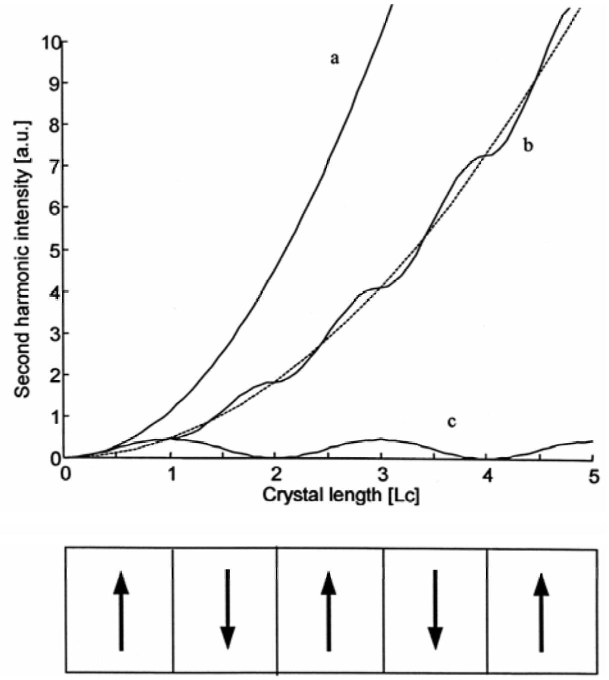

Fig. 3.4 Second harmonic power for perfect phase-matching (a), 1:st order quasi phase-matching (b) and no phase-matching (c). Also shown is a schematic of a periodically structured nonlinear material.

3.5 Nonlinear Crystals

The nonlinear crystal potassium titanyl phosphate, or $KTiOPO_4$, has a central role in this thesis. It was synthesised for the first time in 1890[43], but did not attract real interest until the 1970s when the first detailed analysis of the crystal structure was reported[44]. Its nonlinear and mechanical properties were investigated by John Bierlein and his research group at DuPont Inc, where it was discovered that it possess a high nonlinear susceptibility in addition to a high resistance to optical and mechanical damage[44]. For instance, the nonlinear coefficient d_{33} can be as high as 16.9 pm/V. Since it also has a wide transparency range, 365 nm – 4.3 µm, it has been become one of the most widely used nonlinear crystals. Its reasonably large birefringence makes it suitable for birefringent phase-matching, and since it is ferroelectric it can also be used for quasi phase-matching by the possibility to periodically pole the material. The KTP samples used in this work were made from flux-grown KTP and the periodic domain inversion was achieved by electric-field poling. Another advantage of KTP is its possibility to phase-match at room-temperature.

In addition, the borate crystals BiB_3O_6 (BiBO) and β-BaB_20 (BBO) have been employed in this work. They cannot be periodically poled, since they are not ferroelectric, so birefringent phase-matching is used for efficient nonlinear conversion. This imposes restrictions on the interaction length because of walk-off, and limits the conversion efficiency due relatively small angular acceptance bandwidth. Nevertheless, they have very high damage thresholds, which make them suitable for high power applications. Moreover, they are transparent down to deep-UV and in the case of BBO it has a transparency range of 185 nm – 2600 nm. Unfortunately, the nonlinear coefficient d_{eff} of these crystals is relatively low. For BiBO, it is typically 1 to 3 pm/V[46,47] and for BBO 0.5 to 2 pm/V[48-50]. Nonetheless, they are often the remaining choice when it comes to generation of deep-UV light.

Chapter 4

Compact Lasers

For many applications, the size of the optical device is crucial. Large and bulky devices are often unpractical and difficult to manage. Therefore, down-scaling the size of the frequency-converted, diode-pumped solid-state laser is an important issue. In addition, if these devices can be assembled in a way to make the production more cost-effective, the number of applications could be even more widespread. Here, two different approaches to miniaturise diode-pumped lasers are described.

4.1 Miniature Lasers using Polymer Microcarriers

The first example of a miniature diode-pumped solid-state laser was introduced by J.J. Zayhowski and A. Mooradian in 1989[51], when the concept of monolithic microchip lasers was presented. Monolithic microchip lasers are based on flat-flat cavities, where the cavity mirrors are dielectrically coated on the facets of the gain medium. By using sub-mm long crystals, single-frequency lasing can be achieved since the longitudinal mode spacing is then greater than the spectral gain bandwidth. However, the concept of microchip lasers has later been extended to include crystal lengths of several millimetres. The stability of the flat-flat laser resonator is determined by pump-induced thermal guiding, i.e. the combined effect of thermal lensing and thermal bulging of the end-facets.

For applications where several optical elements are to be assembled in an optical device, the microchip laser approach can be taken one step further. By using micro-structured carriers for mounting of all optical components, i.e. laser crystals, imaging optics, nonlinear crystals etc, passive alignment and compact integration of all components is enabled. This design concept was initially investigated by Å. Claesson *et al* [52], by constructing miniature lasers on a micro-structured silicon carrier. By using wet etching, V-grooves with a bottom angle of 70.5° were shaped in a silicon chip, thus acting as the micro-structured carrier. Rhombic micro-chip laser crystals (3-4 mm long) were diced from mirror-coated wafers in order to fit in the V-groove, see Fig. 4.1. A second identical silicon carrier is then placed on top of the laser crystal, acting as a lid. Thus, robust design and a homogeneous heatsink are provided.

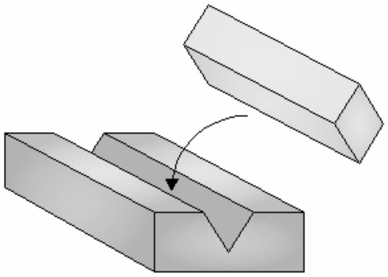

Fig. 4.1 Mounting of rhombic laser crystal in an etched V-groove of a silicon carrier.

In Paper IV, this design concept is extended to micro-structured carriers in polymer materials. Even though the thermal management becomes more challenging using polymers instead of silicon, this approach is promising because of advantages in key parameters such as design freedom of the carrier structure and cost-effective production. The polymer carrier used in Paper IV was manufactured from a thermally conductive polycarbonate (RB019) from Cool Polymers Inc. with a heat conductivity of 20 $Wm^{-1}K^{-1}$, which is considerably larger than for traditional polymers (typically 0.2 $Wm^{-1}K^{-1}$). A single V-groove (0.79 mm deep and 1.12 mm wide) was manufactured using standard injection moulding techniques in 50 mm long sample with an aperture of 10 x 3 mm^2. The rhombic cut Nd:YAG (1 atm% doping) crystal was 3 mm long, having a HR coating for 1064 nm on the incoupling facet and a reflectivity of 96 % at 1064 nm on the outcoupling facet. The laser crystal was fixed in the groove with thermo-compression, using a thin film of evaporated indium as an intermediate layer. The indium film provides better thermal contact, relaxes the tolerances for the crystal dimension and reduces the stress caused by the thermal expansion mismatch between the crystal and the carrier. A second polymer carrier was placed as a lid and fixated with thermo-compression. Examples of miniature lasers built on the polymer carrier platform are shown in Fig. 4.2. The polymer carrier was placed on a Peltier cooling plate kept at 20˚C. Using a fibre-coupled laser diode (LIMO) with a fibre diameter of 200 µm, the laser crystal was pumped with up to 8.4 W of power. A threshold of 400 mW and a maximum output at 1064 nm of 2.08 W was measured, corresponding to a slope efficiency of 26 %. The latter value is lower compared to the results achieved for the silicon carrier, which can partly be attributed to unoptimal overlap between the pump beam and laser beam. In addition, the thermal effects in the laser crystal should be more prominent which also has a detrimental effect on the performance of the laser.

Furthermore, the asymmetric heat flow provided a preference for light polarised in the vertical direction, in contrary to the unpolarised output expected for the isotropic Nd:YAG crystal. This feature was lifted at high pump powers because of thermally induced birefringence, resulting in depolarisation[21] of the light.

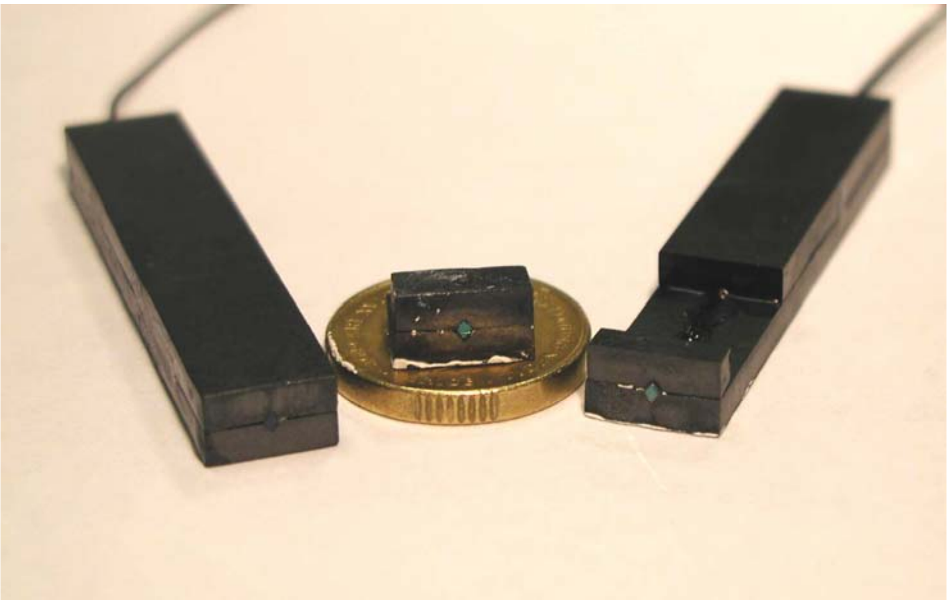

Fig. 4.2 Miniature lasers constructed on a polymer micro-carrier.

Nevertheless, the polymer micro-carrier design concept showed promising results and provides a rugged building-set suitable for mass-production. Especially low power applications, e.g. in bioanalysis, could be an interesting field for this type of low-cost miniature lasers. An example of an optical device based on the micro-structure carrier is shown in Fig. 4.3, where a nonlinear crystal is inserted for frequency conversion into the visible part of the electromagnetic spectrum.

This particular work has been the subject for a review article in the magazine Laser Focus World's January issue in 2004[53].

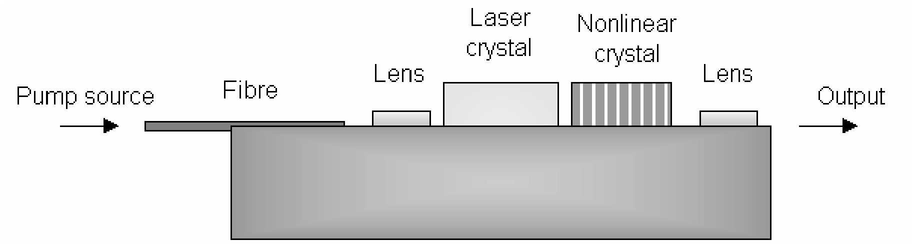

Fig. 4.3 Conceptual design of an optical device based on the micro-structure carrier.

4.2 Beam twisting

4.2.1 Beam Shaping of Astigmatic beams

The use of laser diodes in end-pumping of solid-state lasers is a well adopted method of achieving high conversion efficiency and compactness. A good spatial overlap between the pump- and the laser mode is required for efficient extraction of the pump power. If the solid state laser gain is realized using quasi-three-level transitions the mode matching requirement becomes even more acute together with the requirement of maintaining high pumping intensity along the laser crystal length. These tasks are, however, rather difficult to achieve using either broad-stripe laser diodes or laser diode bars as pumping sources. It is well known, that the single broad stripe laser diodes which can provide power up to 5 W in CW operation generate elliptical astigmatic output beams with a strong asymmetry in the beam propagation constants, M_x^2, M_y^2, along the main axes of the output beam.

One way of overcoming this problem is by using fibre-coupled diodes, thus achieving a rotationally symmetric beam. Variations on the same technique have involved micro-step mirrors in combination with optical fibers[54] and the use of fibre bundles[55]. The drawbacks of this approach are that expensive aspheric lenses have to be used in order to image the laser diode output into the fibre core, and that the total available power is reduced by the coupling losses. Furthermore, the fibre itself with additional focussing optics is space-consuming which is problematic when designing compact solid-state lasers. At the same time the polarization becomes scrambled in the optical fibre, with the consequence that the polarization state of the pump beam becomes a function of surrounding temperature variations and mechanical stresses. This modulation of the polarization state translates directly into the variation of the absorbed pump power and thus the laser output power in anisotropic laser media such as widely used ortho-vanadates or double tungstates. Another proposed way to improve the spatial qualities of an asymmetric laser diode beam is the two-mirror beam-shaping technique[56]. This method is quite efficient but requires delicate alignment of the mirrors and has mostly been employed in the diode-bar pumping arrangements.

4.2.2 The Twisted Beam Approach

In Paper V described in this section, a beam shaping technique based on the concept of twisted Gaussian Schell-model beams is presented. Twisted Gaussian Schell-model beams were introduced by Simon and Mukunda[57] in 1993, and later treated by Friberg *et al*[58]. They showed that an astigmatic beam can be transformed into a stigmatic beam with a position-dependent phase factor, a so-called twist phase. Its effect is to twist the beam about the beam axis in the course of propagation. This transformation is achieved by an astigmatic optical lens system, described both theoretically[58] and experimentally[59,60]. In fact this is a generalization of the special case of transformation between the Hermite-Gauss modes with rectangular symmetry to the Laguerre-Gauss cylindrically symmetric set of modes[61-63]. An important property of this mode transformation is the conservation of the polarization state of the laser beam. In previous demonstrations of this technique, carefully positioned setup of bulk cylindrical lenses have been employed. In this work we show that the mode converter should not necessarily be large and that this technique works well in a compact arrangement in essence containing a single properly designed cylindrical GRIN lens. The laser diode mode transformer and the focussing arrangement using GRIN lenses is in principle simpler, more compact, and is, in principle, easier amenable for automated assembly in solid-state laser manufacturing than the arrangement of aspherical bulk lenses. Moreover, the polarization of the laser diode is preserved with high fidelity in GRIN lens optical arrangements[64]. To demonstrate the functionality of the GRIN lens mode transformer, we used it together with a commercial single stripe laser diode to build a compact blue light source based on intracavity frequency doubling of a Nd:YAG laser operating on the quasi-three level transition at 946 nm.

4.2.3 Theoretical Considerations of Beam Twisting with GRIN Lenses

The Hermite-Gauss set of modes having a rectangular symmetry are very suitable for expansion of the real beams generated by broad-stripe laser diodes. Typically, the laser diode rectangular waveguide supports the single lowest transversal mode in the direction perpendicular to the heterojunction plane and have multimode field distribution in the perpendicular direction. For transformation of this strongly astignmatic beams into a general Hermite-Gauss beam with twist two main types of settings of cylindrical lenses have been proposed[59]: (i) consisting of three lenses where one pair performs imaging in one plane, while the lens in the middle performs a partial Fourier transform in the perpendicular plane; (ii) setup consisting of two cylindrical lenses with the focal length f separated by a distance $\sqrt{2}f$ and transforming an astigmatic rectangular beam preconditioned in such a way that the Rayleigh lengths for the main axes of the corresponding Hermite-Gauss mode-set are both equal to $z_R = f(1+1/\sqrt{2})$. In both mode transformer arrangements the axes of the cylindrical lens system is rotated by 45 degrees with respect to the axes of the Hermite-Gauss mode-set. It has been proved[57] that both setups are equivalent and provide the resulting Gouy phase-shift difference of $\pi/2$ between the two axes of the cylindrical lens system. Obviously the two-lens system is simpler and more practical. A modification of the two-lens setup was proposed by replacing them with a single thick cylindrical lens[65]. For the purpose of mode transformation of a broad stripe laser diode in a compact configuration we designed a beam twister based on cylindrical GRIN lens placed at 45 degrees with respect to the major axes of the laser diode beam.

GRIN lenses have continuous distribution of the refractive index profile $n(x) = n_0 \operatorname{sech}(gx)$ stretching along the length of the optical beam path. Here x marks the direction of the refractive index gradient, g is the gradient constant and n_0 is the index of refraction in the middle of the lens. At a first glance it is not obvious that the GRIN lens can directly replace the mode-transformer based on the thick homogeneous glass block with cylindrical surfaces[65]. On the other hand, a GRIN lens can be looked upon as a thick lens with focal length of $f = (n_0 g \sin(gL))^{-1}$ and a working distance or the distance between the lens surface and focal plane of $s = (n_0 g \tan(gL))^{-1}$, where L marks the physical length of the lens. It is customary by manufacturers to specify the GRIN lens in terms of the pitch parameter which is defined as

$$p = gL/(2\pi). \tag{4.1}$$

Next for the design of the GRIN lens mode transformer we employed the results of Ref. 65 for the required thickness of a glass plate connecting two bulk cylindrical lenses having focal lengths of *f'*:

$$d = 2f'\left(1 + \frac{n'(1-\sqrt{2})}{\sqrt{2}}\right) \tag{4.2}$$

where *n'* is the index of refraction of the glass plate. The required Rayleigh length of the beam inside this bulk transformer then is related to the focal length of the cylindrical lenses and is given by:

$$z'_R = n' f'(1 + 1/\sqrt{2}). \tag{4.3}$$

Considering the analogy between the thick cylindrical lens and the GRIN lens we can derive a design equation for the GRIN lens in terms of the pitch parameter p and the length of the lens L:

$$F(p, L) = L + \frac{L}{n_0 \pi p \tan(2\pi p)} - \left(2 + \frac{n_0\left(1-\sqrt{2}\right)}{\sqrt{2}}\right)\frac{L}{n_0 \pi p \sin(2\pi p)} = 0, \tag{4.4}$$

where we assumed that the distance between the principal planes of the GRIN lens: $d' = L - 2(f - s) = d$ as defined for the bulk cylindrical lens in Eq. 4.2. For a given GRIN lens with a pitch parameter and an index of refraction in the center of the lens (usually the parameters determined by the manufacturer) the Eq. 4.4 can be solved to obtain the required length of the GRIN lens. In order to achieve Hermite-Gauss to Laguerre-Gauss mode conversion, the beam incoming into the mode converter has to be preconditioned in such a way that the beam waists for both the planes of the astigmatic beam is in the middle of the converter and the Rayleigh length in both planes is given by Eq. 4.3. Even if these conditions are not exactly met, the astigmatism of the beam will be still substantially reduced but the output field distribution would be represented by Hermite-Gauss modes with an added twist phase.

4.2.4 Experimental Verification of Beam Twisting with GRIN Lenses

The beam twister GRIN lens was designed employing parameters found in standard commercial products. So we chose the cylindrical lens with of the fraction in center n_0=1.623

and the gradient parameter $g = 0.514$ mm^{-1}. By using Eq. 4.1 and minimizing the modulus of *F(p,L)* in Eq. 4.4 we deduced a required length of around 4 mm. It should be noted that the function *F(p,L)* does not go to zero for the available index of refraction (n_0 should be at least 1.8 in order for Eq. 4.4 to have solutions) which means that transformation into Laguerre-Gauss modes is not possible with this particular GRIN material. On the other hand, for the laser pumping purposes we were only interested in producing a circularized Hermite-Gauss beam with twist. This greatly relaxes the requirements for the GRIN lens and we could choose a commercial off-shelf GRIN lens having 4.4 mm length. As will be shown below, this lens performed the beam circularization function very well. The required Rayleigh length for this beam twister is then 4.3 mm.

The laser diode used in the experiment was a standard broad-stripe 2 W laser diode (Osram) in C-mount, with an emitter area of 200 μm times 1 μm. The beam divergence angles (FWHM) were specified to 8° in the slow axis direction (x-direction) and 38° in the fast axis direction (y-direction). The beam propagation parameters in the planes containing slow and fast axes were $M_x^2 \approx 50$ and $M_y^2 \approx 1$, respectively. The laser diode beam was preconditioned before the beam twister by two separate cylindrical GRIN lenses. The beam waist at the output of the laser diode was imaged with magnification of 26 in the fast axis plane by a cylindrical GRIN lens having the focal length of 0.475 mm, the physical length of 1.16 mm and the working distance of 30 μm. The laser diode slow axis was imaged with the magnification of 1.3 by a cylindrical GRIN lens having the focal length of 2.39 mm, the physical length of 1.08 mm and the working distance of 2.05 mm. The image planes for the slow and fast axes were located in the middle of the beam twister cylindrical GRIN lens, whose axes were rotated 45 degrees with respect to the axes of the incoming beam. The magnification ratios where chosen with the aim of equalizing Rayleigh lengths for the slow and fast axis and making it equal to the Rayleigh length required by the chosen beam twister lens. All GRIN lenses had broadband coating for 800-960 nm wavelength range. The beam preconditioning and beam twisting arrangement is shown schematically in Fig. 4.4.

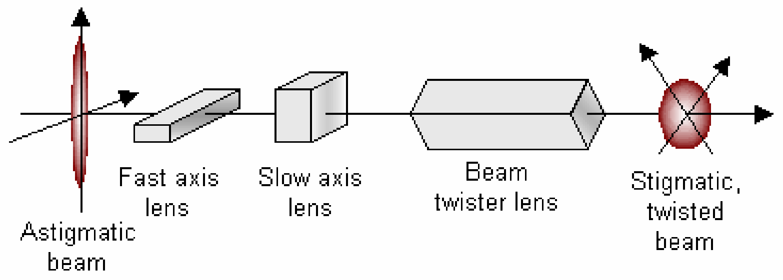

Fig. 4.4 The beam shaping system consisting of three GRIN lenses, showing an astigmatic beam which is transformed into a stigmatic beam with a twist phase.

The physical length of the total setup was 12.0 mm. After initial alignment all GRIN lenses were fixed using high-viscosity UV-curing epoxy. A photo of the lens arrangement can be seen in Fig. 4.5.

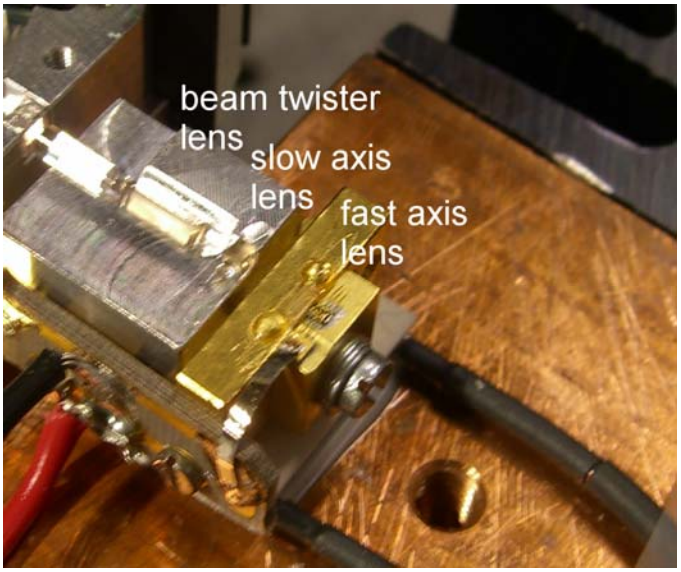

Fig. 4.5 The lens arrangement in front of the laser diode.

The beam twister arrangement, if properly constructed, converts an astigmatic beam into a circularized stigmatic beam with the resulting beam propagation parameter of $M_{BT}^2 = \left(M_x^2 + M_y^2\right)/2$. We determined the beam propagation parameters for the twisted beam in the slow axis and fast axis planes by focussing the output beam using a f=30 mm spherical lens and measuring the beam waist distribution around the focus. The twisted beam was to a large degree stigmatic with $M_x^2 = 24$ and $M_y^2 = 18$ and corresponding far-field divergence angles (1/e^2 half-width) of 4.7 mrad and 4.2 mrad, respectively. The result of the beam caustic measurements is shown in Fig. 4.6.

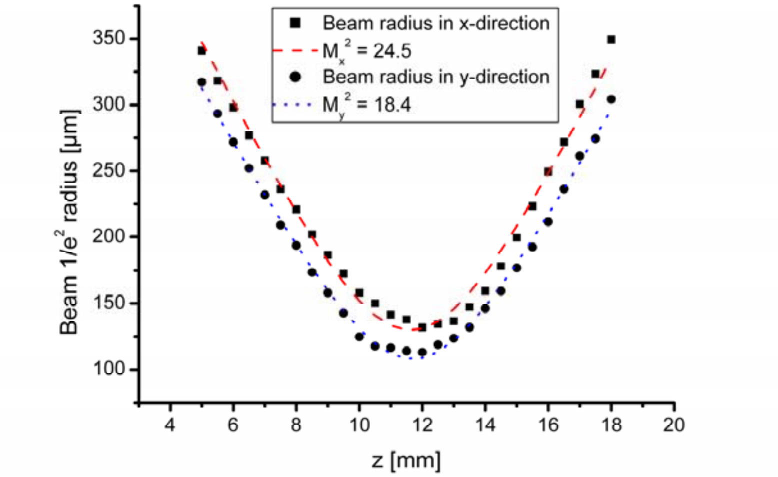

Fig. 4.6 The result of the M^2 measurements in the x- and y-direction.

We also verified that the polarization of the laser diode was preserved in the beam shaping system. The laser diode power after beam shaping was measured as function of the diode current, resulting in a maximum output power of 1.49 W at a diode current of 2.4 A. Given that the output power without the beam twisting system was 2 W, this corresponds to a transmission of 75 %.

4.2.5 Diode Pumping of a Frequency-Doubled Solid-State Laser

Ultimately, the usefulness of the beam twisted diode was tested by employing the beam twisted laser diode for pumping of an intra-cavity frequency-doubled Nd:YAG quasi-three level laser operating at 946 nm. The laser setup is shown in Fig. 4.7. To focus the output from the diode laser, an axially symmetric GRIN lens (pitch = 0.23, length 4.4 mm, diameter 1.8 mm) with an AR-coating maximized for 830 nm, was inserted 1.3 mm after the beam twister lens. This resulted in $1/e^2$ beam radii of 50 μm in both transversal directions, approximately 1 mm behind the lens.

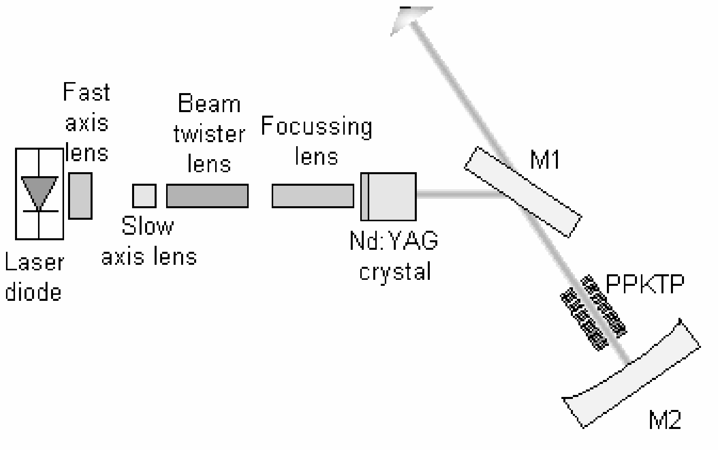

Fig. 4.7 The frequency-doubled Nd:YAG laser, pumped by the beam twisted laser diode.

The Nd:YAG crystal (doping level 1 atm%) was 1.5 mm long and had an aperture of 2 x 2 mm^2. The first surface was AR-coated for 808 nm and had a highly reflective coating at 946 nm, and the other was AR-coated for 946 nm and 1064 nm. At maximum diode current, the power reaching the laser crystal was 1.4 W. A 2 mm long PPKTP with a nominal grating period of 6.09 μm was used for frequency-doubling of the 946 nm light. The surfaces of the PPKTP were AR-coated for 946 nm and 473 nm. To achieve linearly polarized light in the cavity, a folding mirror was employed at an angle of 56˚. This mirror was highly transmissive ($T > 98\%$) for 473 nm, thus acting as the outcoupling mirror for the 473 nm light. Its reflectance was larger than 99.9 % at 946 nm. The cavity was enclosed by a mirror with a ROC = -50 mm and with a highly reflective coating at 946 nm.

The 473 nm and the 946 nm output were measured behind the 56˚ mirror as function of the diode current, using a Schott BG39 filter to separate the blue light from the IR light. Accounting for the filter losses, the maximum 473 nm power was 28 mW, measured at 2.4 A of diode current. This corresponds to around 9.6 W of 946 nm circulating power, and as expected, the second harmonic dependence on the fundamental is quadratic. The result is presented in Fig. 4.8.

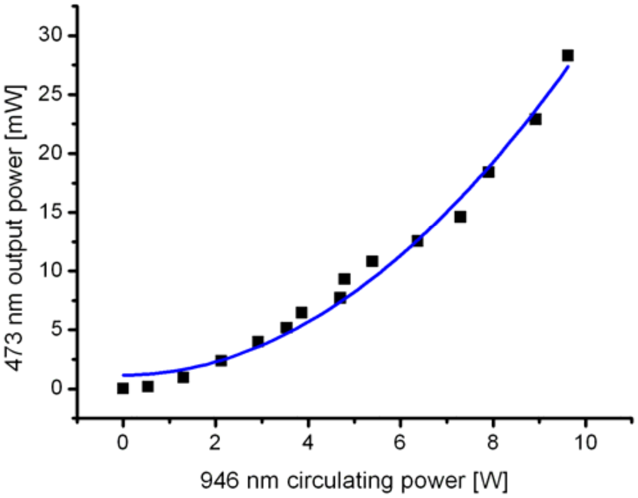

Fig. 4.8 The 473 nm output as function of circulating 946 nm power. The solid curve is a quadratic best fit.

The beam quality factors in the x – and y-direction were measured for the 473 nm light by using a fused silica lens with a focal length of 35 mm, giving $M_x^2 = M_y^2 = 1.3$. This corresponds to a far-field divergence angle (half-width) of 8.3 mrad. The result of the beam caustic measurements for the 473 nm output is displayed in Fig. 4.9.

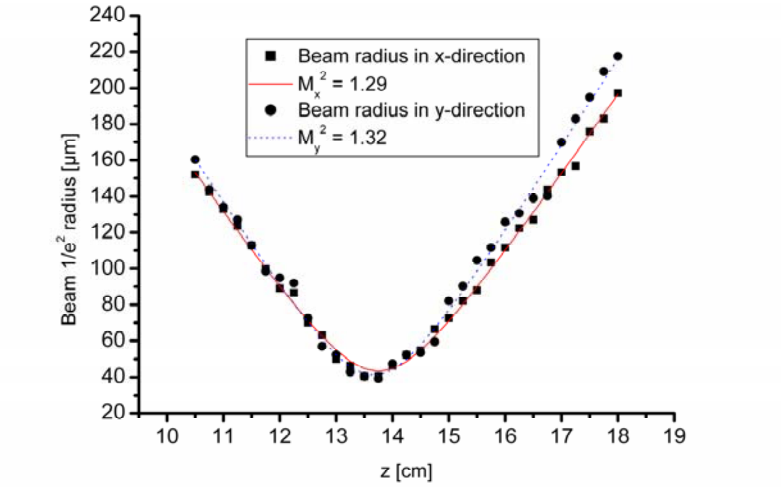

Fig. 4.9 The beam parameter products for the 473 nm light.

Finally it should be noted that the laser diode beam parameters are to a large degree reproducible for mass-produced devices. Consequently, it makes sense to consider making a monolithic GRIN lens assembly consisting of beam shaping and focussing lenses. This can be easily accomplished, e.g., by bonding GRIN lenses to the properly selected glass spacers. This would further reduce the length of the arrangement and substantially reduce the Fresnel losses.

Chapter 5

Visible Light Sources based on Sum-Frequency Mixing

Frequency conversion with periodically-poled nonlinear crystals into the visible spectral regions has been part of optical research for the last decade. The development of compact and efficient continuous wave lasers, ranging from the yellow-orange to the blue spectral region, has accelerated over the last several years[4,66]. These lasers are presently replacing the traditional gas lasers used in applications like bioanalysis, biomedicine, reprographics and semiconductor inspection.

Here, two kinds of methods to generate light in the visible spectral region based on sum-frequency mixing are presented. One method involves a diode-pumped solid-state laser and a laser diode, and has been used to generate light in the blue spectral region. However, this scheme can be used not only for the technologically interesting wavelength band of the Ar^+-ion lasers, but for obtaining essentially any wavelength in the visible spectrum by appropriate choice of lasers. The other method employs two diode-pumped solid-state lasers and was used for generation of yellow-orange light. In this case, the possible wavelengths used in the nonlinear interaction are limited and thus the wavelength of the generated light as well, but the power level is on the other hand substantially higher than in the first case.

5.1 Light Sources in the Blue Spectral Region

Low power, CW Ar^+-ion lasers are presently used in applications like bioanalysis, graphics and semiconductor inspection. A trend today is to replace these lasers with diode-pumped alternatives, since the Ar^+-ion lasers are bulky and inefficient. So far most attempts to reach the blue-green wavelength range have been based on frequency doubling of semiconductor lasers. Efficient blue light generation was first obtained at 425 nm by direct doubling of the radiation from a single stripe laser diode in a quasi-phase matched $LiNbO_3$ waveguide[67]. However, it was found that such units were unstable in output power as the waveguides had a very narrow phase-matching bandwidth (typically 0.2 nm) and the laser diodes drifted in wavelength with time due to mode hops, temperature and mechanical drift and aging[68]. In many biotech applications the 488 nm Ar^+-line is used. For this wavelength, particular chemistry is developed and matched to fluorophores. With the development of high power pump diode lasers for Er:Yb-fiber amplifiers at 980 nm it became possible both to reach this wavelength band and to obtain higher frequency doubled power at the same time. These lasers can be wavelength stabilized with pig-tailed fibre Bragg gratings and with such configurations it has been possible to obtain a long term stable blue-green light source emitting more than 5 mW in the 488 nm band[68]. This early work with frequency-doubled semiconductor lasers involved edge-emitting diodes, but recently, optically[69-70] and electrically pumped surface-emitting lasers[72] (VCSELs) have been used with intra-cavity frequency doubling. The bandgap of the InGaAs semiconductor has in both these cases been tailored to emit at around 976 nm to obtain the desired 488 nm wavelength after frequency doubling. Frequency doubling of fibre lasers emitting in the same spectral region has also proven to be efficient[73]. Single-frequency blue output with a linewidth down to a few MHz, has been obtained from an intra-cavity configuration[74,75], and using master-oscillator-power-amplifier (MOPA) systems[76,77]. Also methods based on sum-frequency generation (SFG) have been exploited, for example to attain yellow radiation[78,79] and blue radiation[80]. Although output powers as high as 20 W in the visible wavelength range has been achieved[78], remaining problems are power stability and high-frequency noise.

The concept of using a solid-state laser and a laser diode for the frequency mixing was first reported by Risk et al[81], where the laser diode was simultaneously used for pumping of the solid-state laser. A modulated blue laser source by direct modulation of the laser diode has also been demonstrated[81,82]. To be able to optimize each mixing source individually, it is advantageous to employ separate laser diodes for pumping and mixing, respectively. Furthermore, the nonlinear conversion efficiency can be improved by using a resonator cavity to enhance one or both of the IR fields. Several experiments employing DPSSLs and laser diodes in both intracavity[83,84] and extracavity[85,86] resonator configurations have been demonstrated.

In papers I and II described in this section, we present a simple scheme to obtain visible light by sum-frequency mixing radiation from a diode-pumped solid-state laser (DPSSL) and a laser diode in a periodically poled $KTiOPO_4$ (PPKTP) crystal. The two mixing lasers are combined for single-pass SFG, which is advantageous for stability and low noise. Since high-power laser diodes are available at a wide range of wavelengths, whereas diode-pumped solid-state lasers are fixed at certain wavelengths, it is thereby possible to obtain essentially any wavelength in the visible spectrum by appropriate choice of lasers. Furthermore, scaling in power is possible by using a high power DPSSL. As a proof of concept we choose to construct the light source in the above-mentioned technologically interesting wavelength band of the Ar^+-laser.

5.1.1 Sum-Frequency Mixing of a Solid-State Laser and a Laser Diode

The experimental setup used for the generation of 492 nm light is depicted in Fig. 5.1. A 2 mm long $Nd:YVO_4$ crystal (0.7 atm%, a-cut) was used for the solid-state laser oscillating at 1064.3 nm. It had a dielectric coating on the incoupling facet with high reflectance at 1064 nm and high transmission at 808 nm, whereas the opposite facet had an AR coating for 1064 nm. A mirror having a radius of curvature of 100 mm and a reflectivity of 95 % was used for outcoupling of the laser light. It was pumped at 808 nm with a 1.4 W fibre-coupled laser diode (Osram GmbH) with a fibre diameter of 200 μm. The pump light was focused into the laser crystal by means of two f = 11 mm lenses. This gave a maximum output power of 730 mW, corresponding to an efficiency of 52%. The output beam was polarized in the s-direction and the beam quality was close to Gaussian (M^2 ~1.5). For collimation of the beam, a lens with a focal length of 150 mm (L1) was used, giving a circular beam with a diameter of approximately 1 mm.

To obtain radiation at 492 nm, a laser diode from Axcel Photonics was employed. It was a narrow-stripe laser diode in C-mount, with an emitter area of approximately 5 μm times 1 μm. The beam divergence angles (FWHM) were specified to 8° in the slow axis direction (x-direction) and 28° in the fast axis direction (y-direction). For 500 mA of drive current a power of 400 mW was emitted in a single transverse mode. The free-running wavelength at this power and at a temperature of 36 ºC was 915.7 nm. A laser diode lens (Melles Griot 06GLC001, L2) was used for collimation of the beam. Its N.A. was 0.615 and its focal length was 6.5 mm. After collimation, the beam was astigmatic with a diameter of 4.8 mm in the x-direction and 1.9 mm in the y-direction. To achieve a better mode-overlap in the PPKTP crystal, the beam was reduced to 1.7 mm in the x-direction with the help of two uncoated cylindrical lenses acting as a telescope (T). Due to Fresnel reflections from the cylindrical lenses and the beam combiner, the effective power from the laser diode reaching the PPKTP crystal was 280 mW.

For the non-linear frequency conversion, a 9 mm long PPKTP crystal of thickness 1 mm times 1.5 mm was used. The crystal was flux-grown and had a nominal grating period of 6.99 μm designed for first order quasi-phase matching using the d_{33} coefficient. Domain inversion of the KTP crystal was achieved by electric-field poling. Its non-linear coefficient was d_{QPM} = 10 pm/V, measured by SHG of a Ti:Sapphire laser. This value is close to that of a perfectly poled crystal. The crystal had antireflection coating for 914 nm and 1064 nm on one side, and antireflection coating for 914 nm, 1064 nm and 492 nm on the opposite side.

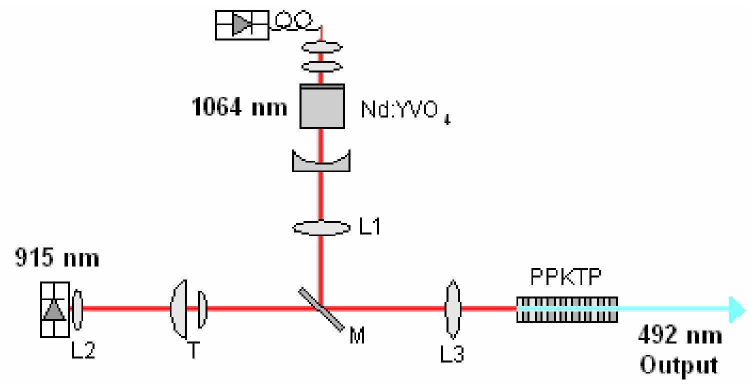

Fig. 5.1. The first version of the experimental set-up.

The two lasers were aligned perpendicular to each other and the beams were then combined with a dichroic mirror (M). By using a f = 50 mm lens (L3) the beams were focused to a 1/e^2-radius beam waist of 14 μm and 16 μm for the laser diode, and 28 μm for the DPSSL, inside the PPKTP crystal. For comparison, a numerical simulation of the mixing of two focused circular Gaussian beams was done, based on an analysis made by S. Guha and J. Falk[36]. The numerical simulation gave that the optimum focused spot sizes in the PPKTP crystal are 23 μm and 25 μm, respectively. Unfortunately, the available optics limited the choice of focused beam widths to the above stated values.

Two versions of the experimental set-up were tested. In the first set-up (depicted in Fig. 5.1), no attempt was made to long-term stabilize the laser diode's spectral output. This gave a maximum SFM output power at 492 nm of 4.0 mW. The experimentally achieved 492 nm power should be compared to 4.1 mW, calculated from the numerical simulation for two circular Gaussian beams taking the focusing condition into account. The generated power is given by $P_3 = \gamma_{SFM} P_1 P_2$, where the parameter γ_{SFM} is dependent on the non-linear coefficient of the material, the optical frequencies taking part in the non-linear process and the beam focusing conditions[4]. Hence if P_1 is fixed and P_2 is varied, the SFM power should vary linearly as a function of P_2. This is also the case as seen from Fig. 5.2, where the SFM power is plotted vs. the DPSSL power. In this way, power scaling would be a simple task, for example by increasing the DPSSL power.

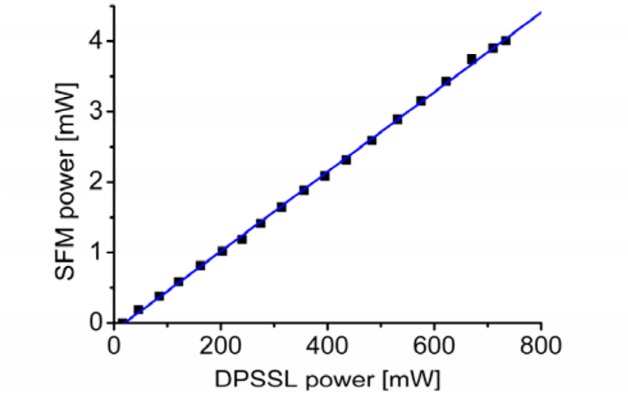

Fig. 5.2 492 nm output power measured for fixed laser diode power (at 280 mW) and changing the DPSSL power.

It is convenient to define the normalized conversion efficiency as

$$\eta_{SFM} = \frac{P_3}{P_1 \cdot P_2 \cdot L}, \tag{5.1}$$

where P_3 is the generated power, $P_{1,2}$ is the power of the two interacting beams, respectively, and L is the length of the nonlinear crystal. An output power of 4 mW would then correspond to 2.2 $\%W^{-1}cm^{-1}$, given that the laser diode power was 280 mW, the 1064 nm power was 730 mW and the length of the PPKTP crystal was 9 mm.

The spectral output of the folded solid-state laser was measured with an optical spectrum analyser having a resolution of 0.06 nm. With the spectrum analyzer three longitudinal modes could be detected, centered at 1064.3 nm and separated by 0.1 nm. This mode separation corresponds to the Nd:YVO_4 crystal length and is attributed to an imperfect AR coating on the output facet of the laser crystal. The laser diode was not single longitudinal mode either, though the total spectral width was narrower than the resolution of the spectrum analyzer.

The maximum power was reached at a KTP temperature of 36.2 ºC and the effective temperature bandwidth (FWHM) was approximately 5.8 ºC, as seen in Fig. 5.3. Regarding the temperature bandwidth, basic QPM theory[87] gives a numerical value of 3.4 ºC. The larger experimental value of 5.8 ºC is due to the presence of several longitudinal modes in the two lasers, giving a larger thermal acceptance bandwidth compared to the ideal single mode case. It can also be noted that the two side-peaks expected from theoretical analysis are missing, which also a consequence of the multi-longitudinal modes of the lasers.

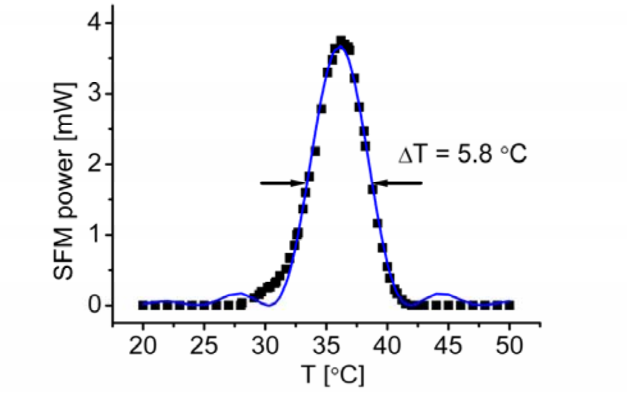

Fig. 5.3 The 492 nm output power as a function of the temperature of the PPKTP crystal. The measured data is represented by the squares and the curve is a sinc^2-fit of the data. The temperature bandwidth was ΔT = 5.8 ºC.

The short-term power fluctuations were less than 2.5 %. As can be expected, the beam shape was slightly elliptical, but it was nevertheless Gaussian in both directions.

5.1.2 Wavelength Stabilization of the Laser Diode

Occasionally it happened that the laser diode mode hopped resulting in a large instability of the SFM signal. In this case the wavelength shift was large enough to exceed the phase-matching bandwidth of the PPKTP crystal, which is in the order of 0.2 nm[4]. The mode hops, typically 0.3 nm, were primarily attributed to uncontrolled back-reflections from the optics and the crystal. In order to tune and long-term stabilize the wavelength of the laser diode, a transmission grating (Spectrogon AB) with 2000 lines/mm was employed in a Littrow configuration. In this configuration the grating has to reflect the -1:st diffraction order, see Fig. 5.4 below. From the grating equation it is possible to derive the required incident angle which is given by

$$\sin\theta_{in} = \frac{\lambda}{2d} \tag{5.2}$$

where λ is the wavelength and d is the grating period. As the wavelength of the laser diode was 915.7 nm and the grating period was 500 nm, the transmission grating was oriented with an angle of 66.3º towards the laser diode in order to control the wavelength and stabilize it at the phase-matching wavelength. Precision alignment of the transmission grating was possible by employing a motorized mount (New Focus). The distance from the emitter of the laser diode to the surface of the grating was approximately 6 cm. The laser diode could be tuned for wavelengths between 906 nm and 916 nm by tilting the grating where it operated perfectly stable with a linewidth below the resolution bandwidth of the OSA. However, it was not single-longitudinal mode and taking into account that the external cavity of the laser diode was 6 cm, it was calculated that the laser diode contained roughly 10 longitudinal modes. By employing a scanning Fabry-Perot interferometer, a linewidth of approximately 300 MHz was measured. The reflectance of the laser diode emitter facet was 2.5 % as specified by the manufacturer whereas the grating reflectance at 915 nm was in the order of 12 - 15 %. Thus, a narrower linewidth could possibly be achieved by using a proper AR coating on the laser diode.

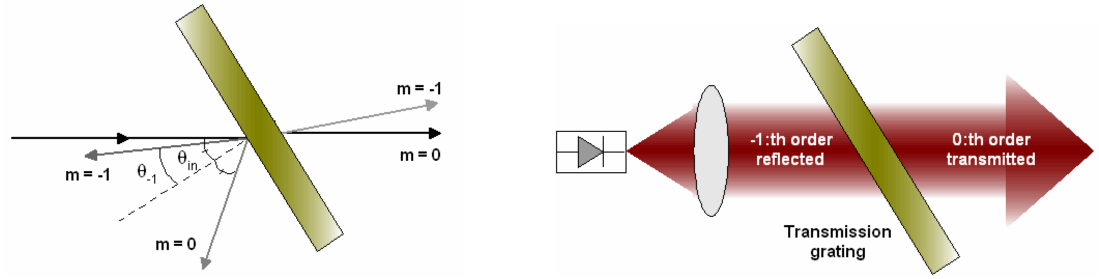

Fig. 5.4 Different orders of reflection and transmission from a transmission grating (left). In a Littrow configuration ($\theta_{in} = -\theta_{-1}$), the -1:th order is reflected back into the laser diode (right).

The diode pump power reaching the PPKTP crystal was in this case 110 mW. The power losses were mainly due to beam clipping, where the outer parts of the laser diode beam were cut because of the large tilt angle in combination with an undersized aperture of the transmission grating mount. Furthermore, the 0:th order reflection loss of the grating accounted for approximately 20 % of the total loss. The generated 492 nm power was in this case 0.74 mW, measured at a slightly lower power from the solid-state laser of 620 mW. This would then correspond to normalized conversion efficiency of 1.2 $\%W^{-1}cm^{-1}$. The decrease in conversion efficiency compared to the previous setup can be attributed to the clipping of the laser diode beam, which produced a somewhat diffracted beam and thus a deterioration of the beam quality.

The noise of the turquoise light was studied with an electrical spectrum analyser (HP 8560A). It exhibited very low noise levels, where only a small peak at 2.3 MHz could be observed (see Fig. 5.5) which is assumed to originate from relaxation oscillations of the $Nd:YVO_4$ laser. The signal-to-noise ratio at 2.3 MHz was measured to 104 dB.

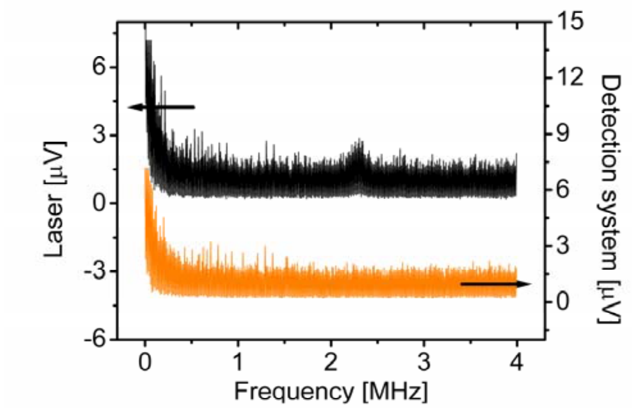

Fig. 5.5 Noise spectra of the 492 nm light (upper trace) and detection system noise (lower trace). Relaxation oscillations originating from the DPSSL are present at 2.3 MHz.

5.1.3 Intra-Cavity Setup

A possible way of scaling up the generated SFM power is to employ an intra-cavity configuration for the solid-state laser. More than 27 mW of 492-nm output power was demonstrated in Paper II, where a similar compact design was used. The 492-nm light was generated inside the cavity of the solid-state laser, thereby utilising the high circulating power, whereas the laser diode was single-passed through the PPKTP. The experimental set-up is depicted in Fig. 5.6. After the transmission grating, two anti-reflection (AR) coated cylindrical lenses (f_1 = 25.7 mm and f_2 = 10 mm) were used for beam shaping, giving a beam diameter of 1.9 mm in both directions. A dichroic mirror (M1, R>95% at 914 nm) was used for controlling the beam position in the PPKTP. To focus the laser diode beam, a f =100 mm (L) AR-coated lens was employed. This gave a spot radius of 46 µm inside the PPKTP crystal. The effective laser diode power reaching the PPKTP crystal was 170 mW. Again, the power losses compared to the 400 mW produced by the laser diode were mainly due to beam clipping.

Here, the solid-state laser was folded using two planar dichroic mirrors, M2 and M3. These mirrors were highly reflective (R > 99.95%) at 1064 nm for 45º. The reflectivity at 914 nm (45º) was less than 5%. The distance between the mirrors was only 11 mm, resulting in an intra-cavity $1/e^2$-radius beam waist of approximately 90 µm. As an output coupler (OC), a mirror with a radius of curvature of 50 mm was employed at a distance of 6 mm. Its reflectivity at 1064 nm was specified to 99.95%. A fiber-coupled diode (Osram GmbH) was used for pumping at 808 nm, giving a maximum pump power of 964 mW at a diode temperature of 35 ºC. The fiber diameter was 100 µm. The pump light was focused into the laser crystal by using 1:1 imaging, thus achieving good spatial overlap between the pump and laser beam.

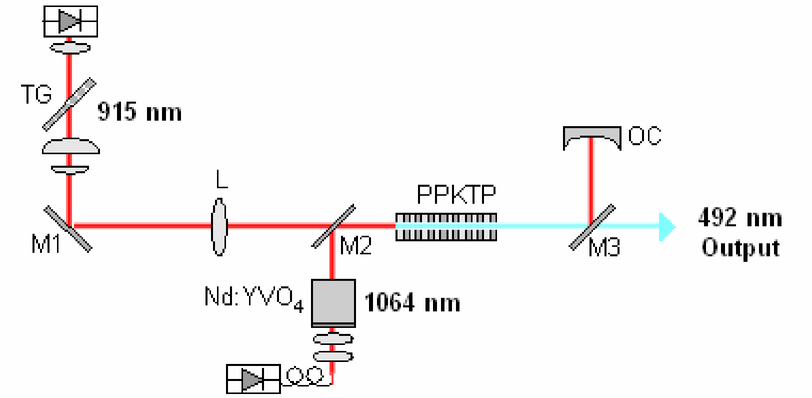

Fig. 5.6 Schematic design of the 492 nm light source.

The DPSSL had a slope efficiency of 24% and emitted a maximum of 23.5 mW, corresponding to 47 W of circulating power inside the laser cavity. Keeping the laser diode power fixed at 170 mW, the SFM power was measured as a function of the circulating 1064 nm power, see Fig 5.7. A maximum 492-nm output power of 27.4 mW was achieved at a circulating power of 39 W. This corresponds well to the theoretically calculated SFM power of 29 mW, where the experimental focussing conditions and beam overlap were taken into account. Using the previously defined normalized conversion efficiency, this corresponds to η_{SFM} = 0.45 $\%W^{-1}cm^{-1}$, which is considerably lower to that achieved in the single-pass configuration. This can be attributed to the substantially looser focusing for the 1064 nm beam compared to the previous case. Since the beam width of the DPSSL was twice as large as the width of the laser diode beam in the PPKTP crystal, it is expected that effectively 60% of the 1064 nm power was not used for the nonlinear interaction.

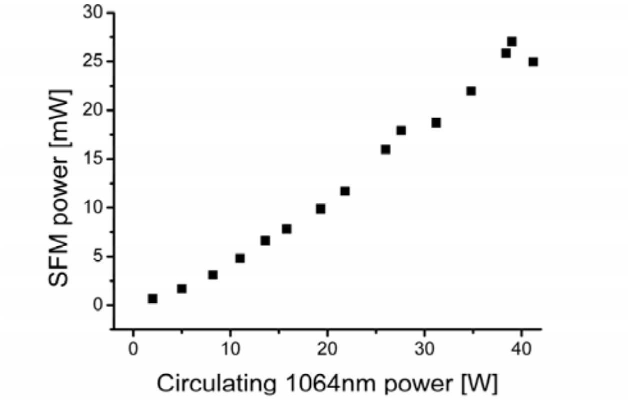

Fig. 5.7 492-nm CW output power as a function of the circulating 1064 nm power for fixed laser diode power (at 170 mW).

Saturation in both the SFM power and the normalized conversion efficiency were observed at high 1064 nm power, but the slope in the SFM power is nevertheless linear up to about 40 W of circulating power. Using that the absorption coefficient for KTP at this wavelength is in the order of 10^{-4} cm^{-1} [88], this would correspond to a few milliwatts of absorbed power. The heat generation in KTP was thus negligible and a thermal lens was not pronounced. The thermal effects in the laser crystal were also minimal at these relatively low pump powers. This is also confirmed experimentally, since no infrared or SFM beam quality degradation was observed at high circulating power. The saturation apparent in SFM output at the highest intra-cavity powers can be attributed to the broadening of the longitudinal mode spectrum and can thus not be explained by the thermal-lens related modification of the mismatch in mode overlap.

In addition, no gray tracking or power degradation occurred during the experiment, which took place during several hours per day for more than a week.

The slow SFM power fluctuation during a measurement over two hours was typically less than 10% and related to the mechanical stability of the setup. A high-speed Si-photodetector was used for measuring the high-frequency noise of the 492-nm light. A peak-to-peak value of 10% and a RMS value of 2.5% were recorded. The same noise characteristics were observed with the free-running DPSSL laser. Thus we attribute the SFM noise exclusively to the DPSSL laser source. By studying the spectrum of the SFM signal in Fig. 5.8, it is apparent that two modes of oscillation were taking part in the nonlinear interaction. As can be seen from the figure, the overall bandwidth for the 492-nm light was around 0.4 nm. By placing an etalon inside the cavity of the DPSSL the problem of simultaneous SFM of the different longitudinal modes could be overcome and the noise of the SFM signal significantly reduced. In contrast to the blue-green laser sources based on intracavity second harmonic generation where the nonlinear processes lead to longitudinal mode competition and increased noise in the visible output (the so called "green noise" phenomenon[89]), the noise of a purely SFM based visible source can be easily suppressed by stabilising the DPSSL laser and ensuring that the longitudinal mode spectrum fits the bandwidth of the nonlinear crystal.

The maximum power was reached at a KTP temperature of 31.1ºC and the effective temperature bandwidth (FWHM) was approximately 5.3ºC, as seen in Fig. 5.8. The latter value is larger than the numerically derived[87] value of 3.4ºC, which can be expected since the multi-mode case gives a larger thermal acceptance bandwidth and a lower efficiency.

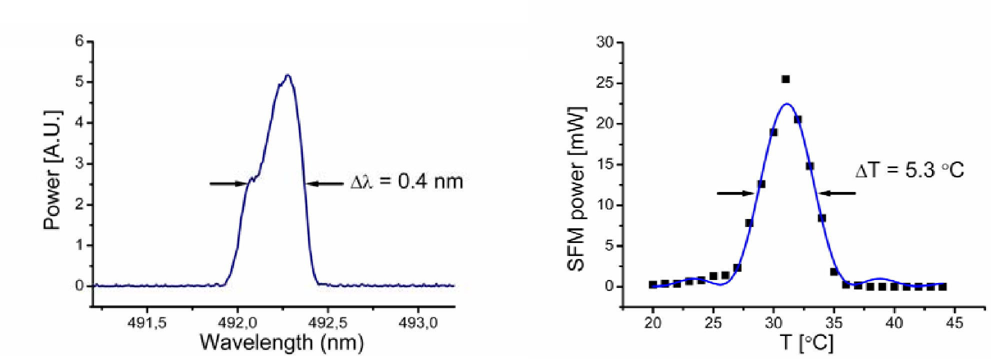

Fig. 5.8 The spectrum of the SFM signal at an output power of 27 mW. The total bandwidth is approximately 0.4 nm (left). The 492-nm output power as a function of the temperature of the PPKTP crystal. Measured data is represented by the squares and the curve is a sinc^2-fit of the data. The temperature bandwidth is 5.3 ºC (right).

The mixing configuration that was used to generate 492 nm light provides a flexible and compact way to reach essentially any wavelength in the visible spectral range. Using the high power from a diode-pumped solid-state laser, whether single-passed or from the intra-cavity field, and combining it with the appropriate wavelength from a diode laser, the foremost advantages of each light source can be utilized. However, there is a trade-off between compactness and high output power. The intra-cavity configuration presented here provided as much as 27 mW of 492 nm radiation in a very compact setup, and this number could be scaled up by using curved mirrors and a larger size of the cavity which would result in a tighter intra-cavity beam waist. In the above described experiments, there was also a loss in diode power due to an unoptimized mount for the transmission grating.

It should also be mentioned that a volume Bragg grating (VBG) could be used instead of a traditional transmission grating, thus providing an even more compact setup at the same time as gaining advantages as a extremely narrow linewidth and less expensive optical components.

An attempt to modulate the 492 nm light was made by modulating the drive current of the laser diode. Unfortunately, the presence of several longitudinal modes in the laser diode had the effect that the modulation affected each mode individually and resulted in mode hopping in the laser diode. This can be seen in Fig. 5.9 below.

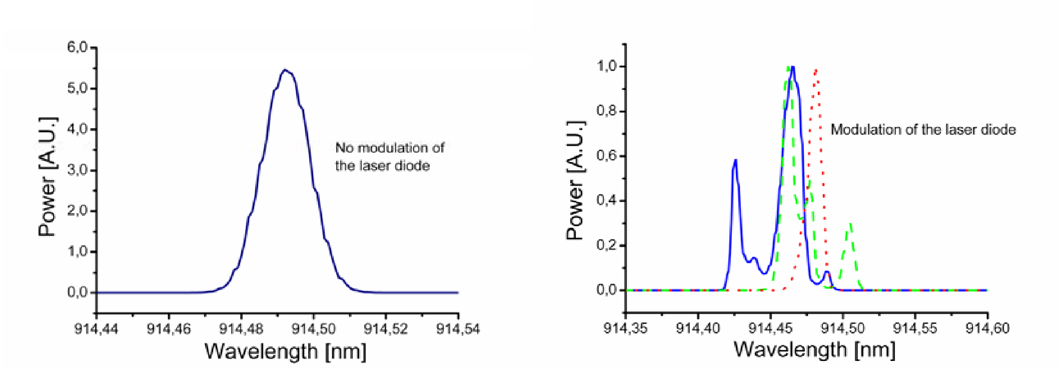

Fig. 5.9 The left graph displays the spectrum of the laser diode in absence of current modulation. To the right is the result of current modulation, clearly showing the mode hopping behaviour of the laser diode.

5.2 Light Sources in the Yellow Spectral Region

Lasers in the yellow spectral region have over the past decade found an increasing number of applications. The yellow spectrum corresponds to the peak absorption of several popular fluorescent dyes and of the sodium "D" and "d" lines around 594 nm. Furthermore, a great need exists in the field of biomedical optics for light sources in the yellow-orange spectral range, due to the high absorption in hemoglobin. This makes the yellow spectral range very interesting both in dermatology and ophthalmology. Important dermatological treatments are the removal of tattoos and so-called storchbites. In dermatology, pulsed radiation is often needed whereas in ophthalmology, there exists a need for stable continuous wave light sources in the 1 – 2 W power range. Today copper vapor lasers (578 nm) and various dye-lasers are used in the medical clinics for dermatological treatment. These lasers are generally large in size, inefficient (and thus need water cooling), complicated to operate, and both the gases and liquids used in these lasers are highly toxic.

In paper III described in this section, the objective is to make an all solid-state yellow-orange light source that can reach the required power level and stability necessary for ophthalmologic applications. The system should be cost efficient, compact in size and with a high efficiency and stability, allowing operation without water-cooling or special power installations. We have built an all-solid-state system pumped by laser diodes, capable of generating more than 750 mW of 593 nm continuous-wave power with a total diode pump power of 6.6 W. The system is based on sum-frequency generation (SFG) between the 1064 and the 1342 nm laser lines of two Nd:YVO_4 lasers using periodically poled KTP as the nonlinear media.

Different approaches have been used to pursue an all solid-state yellow laser. Recently[90], 605 nm radiation in the milliwatt range have been generated using frequency-doubled quantum-well semiconductor lasers. However, the power level of these devices is still too low and the wavelength too long for many medical applications. In the pulsed regime Raman shifted 1064 nm lasers with subsequent second harmonic generation have been shown to generate average powers in the Watt level[91]. More exotic materials such as Cr:Forsterite with large tuning range have been used to generate tens of milliwatts in the orange spectral range[92]. The approach described in this section is based on sum-frequency generation of two infrared Nd-based laser lines at 1064 and 1342 nm. This work is also presented in Paper III. Similar approaches have been demonstrated previously by a number of groups, both in the continuous-wave[93,94] and in the pulsed regime[95,96]. In the case of CW operation, these systems were based on extra-cavity SFG, whereas some of the pulsed systems used intra-cavity mixing. The reason for this choice was the difficulty in obtaining stable CW operation in the intra-cavity SFG system. In order to obtain sufficient SFG conversion efficiency it is necessary to use a doubly resonant external cavity[78, 97].

5.2.1 Sum-Frequency Mixing of two Solid-State Lasers

We have investigated a system based on SFG between the intra-cavity field of one solid-state laser and a single-pass field of another solid-state laser, as shown in Fig 5.10. Different cavity configurations were tested and compared both in terms of conversion efficiency and stability. The highest conversion efficiency as well as the best stability was obtained in the setup shown in Fig 5.10. The setup was tested both in a single-pass configuration with the 1064 nm laser and as a doubly resonant system where the non-linear SFG was intra-cavity to both lasers. At low pump power levels for the 1064 nm laser, the conversion efficiency could be increased by using the doubly resonant configuration. However, as the power was increased, the increase in conversion efficiency occurred at the expense of stable CW operation; the system became highly unstable and the average power generated never exceeded the 750 mW obtained in the single-pass configuration. Using the single-pass configuration it was possible to obtain high conversion efficiency, and maintain a high degree of stability in the system, even when the system operated with several longitudinal modes. A photo of the beam emerging from the laser is shown in Fig. 5.11.

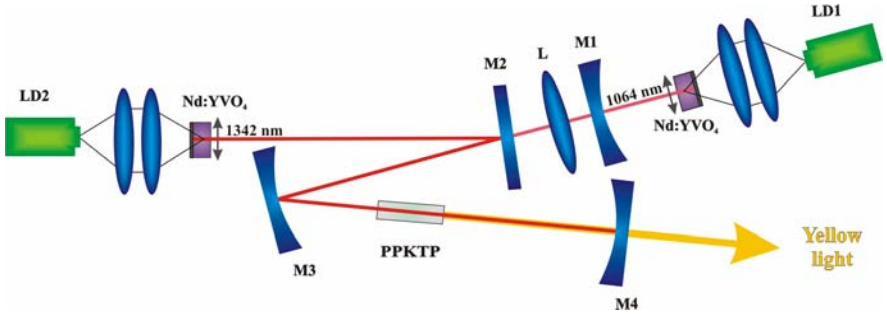

Fig. 5.10 Experimental setup for the 593 nm light generation based on sum frequency mixing between an intra-cavity 1342 nm laser and a single-pass 1064 nm laser in a PPKTP.

The experimental setup used for the generation of 593 nm light consisted of a 1342 nm laser with a folded cavity comprising the nonlinear crystal which in this case was a 11 mm long periodically poled KTP (PPKTP), and a 1064 nm laser, see Fig. 5.10. Both lasers were pumped by laser diodes (RPMC) capable of delivering up to 4 W of power at 808 nm. The laser crystal in the 1342 nm laser was a 3 mm long, a-cut Nd:YVO$_4$ crystal (1.0 atm%) with a highly reflective coating at 1342 nm on the incoupling facet and AR coating for 1342 nm, 1064 nm and 946 nm on the opposite facet. The cavity was folded by means of three mirrors M2 (planar), M3 (ROC = -100 mm) and M4 (-100 mm), all coated for high reflection at 1342 nm. Mirrors M2 and M4 were also coated for high transmission at 1064 nm, whereas mirror M3 was highly reflecting at 1064 nm. The transmission at 593 nm for mirror M4 was approximately 75%. The distance from the Nd:YVO$_4$ crystal to mirror M3 was 277 mm and the distance between mirror M3 and M4 was 158 mm, resulting in an intra-cavity 1/e^2-radius beam waist of approximately 47 µm between the curved mirrors.

The 1064 nm laser was designed as a straight-forward linear cavity with a 3 mm long, a-cut Nd:YVO$_4$ crystal (1 atm%) having a highly reflective coating at 1064 nm on the incoupling facet and a curved (ROC = -100 mm) mirror with a reflectivity of 95% for 1064 nm acting as an outcoupling mirror. The total physical length of the 1064 nm laser was 50 mm, resulting in a 100 µm beam waist inside the Nd:YVO$_4$ crystal. This was transformed into a 1/e^2-radius beam waist of approximately 36 µm at the 1342 nm beam waist position by the combined effect of a f = 150 mm lens (L) and the curved mirror M3.

The PPKTP crystal had a nominal grating period of 12.65 µm, designed for first-order quasi phase-matching at 25˚C for sum-frequency mixing of 1064 nm and 1342 nm. The total crystal length was 11 mm whereas poling was made over a length of 9 mm. Both facets of the PPKTP were AR coated for 1064 nm, 1342 nm and 593 nm, respectively.

Fig. 5.11 The yellow beam emerging from the solid-state laser system

5.2.2 Experimental Results

Using the setup described above more than 750 mW of yellow-orange light was generated using 3.2 W of diode pump power incident on each of the two laser crystals. This corresponds to an optical-to-optical conversion efficiency of 11 %.

The 1064 nm laser was able to generate 1.8 W of power in a single transverse mode using 3.2 W of diode pump power. This beam was focused by lens L and aligned to match the beam waist of the 1342 nm laser at the position of the PPKTP crystal. The 1342 nm laser was able to form an intra-cavity circulating power of more then 45 W traversing the PPKTP crystal, in the absence of the 1064 nm field (without nonlinear conversion), but then decreased slightly to 40 W. This corresponds to a normalized conversion efficiency of 1.2 %$W^{-1}cm^{-1}$.

Figure 5.12 shows measurements of generated yellow power (diamonds) as a function of diode laser pump power for the 1064 nm laser (Fig. 5.12 left) and 1342 nm laser (Fig. 5.12 right), respectively. Squares are the 1064 nm power transmitted through mirror M4; triangles show the 1064 nm power incident on the PPKTP crystal. Circles indicate the 1342 nm power.

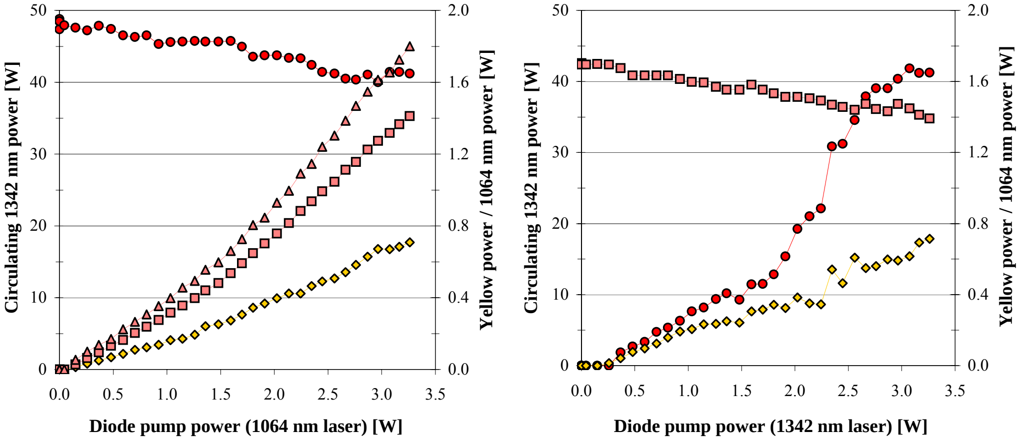

Fig. 5.12 Measurement of the generated 593 nm power (diamonds) as well as the circulating 1342 nm power (circles) and the transmitted 1064 nm power (squares) as a function of the diode pump power for the 1064 nm laser (left) and as a function of the diode pump power for 1342 nm laser (right).

Clearly, the generated power as a function of the 1064 nm pump power shows the smoothest behavior. However, the variations as a function of the 1342 nm pump diode power were also seen without nonlinear conversion, and they probably originated from thermal lensing rather than from instabilities induced by the nonlinear process. By operating the system at constant pump power and with a proper temperature stabilizing circuit for the PPKTP crystal, we obtained a very stable 593 nm output power. When the 1064 nm laser was operated in a single-pass configuration as described above, no indications of mode beating between longitudinal modes in the two lasers were seen. Furthermore, the transverse beam profile of the generated yellow light was very close to the fundamental Gaussian distribution, however slightly elliptical due to the slightly off-axis incidence on the curved mirror M3. The beam propagation parameter M^2 was measured by means of a beam analyzer fixed on a translation mount, resulting in $M_x^2 = 1.15$ and $M_y^2 = 1.05$, respectively. The three-dimensional beam profile of the 593 nm light is shown in Fig. 5.13 below.

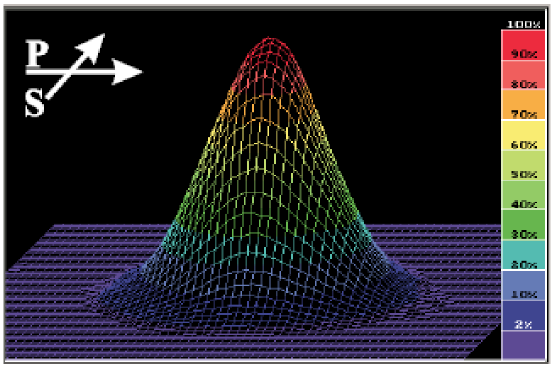

Fig. 5.13 The measured three-dimensional profile the 593 nm beam. Here, P indicates the direction parallel to the plane of incidence (x) and S refers to the perpendicular direction (y).

Using the measured values of the 1064 and the 1342 nm power incident on the PPKTP crystal and employing Eq. 3.19 given in Chapter 3, an effective nonlinear coefficient of the PPKTP crystal was calculated to d_{QPM} = 10.2 pm/V. By scanning the temperature of the PPKTP crystal from 30 ˚C to 70 ˚C, the phase-matching temperature could be determined. Figure 5.14 below shows the measured 593 nm power as a function of the PPKTP crystal temperature.

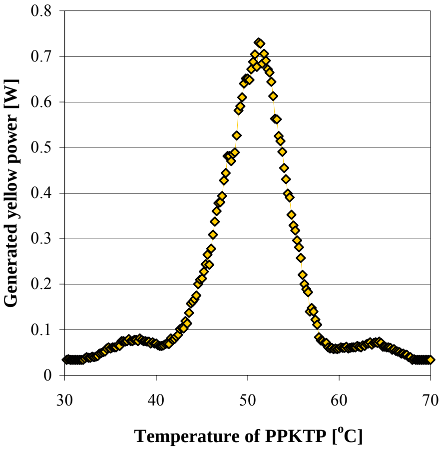

Fig. 5.14 Measured 593 nm power as a function of the PPKTP temperature.

As expected, the generated yellow power varies as a sinc^2-function, and the optimum phase-matching temperature was found to be 51 ˚C which is in fairly poor agreement with the designed phase-matching temperature. This discrepancy is most possibly due to uncertainties in the Sellmeier equations for KTP. However, the FWHM temperature bandwidth was 7.9 ˚C, which is in excellent agreement with the calculated bandwidth[87] of 7.8 ˚C, which would correspond to an effective crystal length of 8.9 mm.

A doubly resonant approach was also tested, by inserting an additional mirror coated for high reflectance at 1064 nm and high transmittance at 593 nm after mirror M4. In this way, the 1064 nm light was returned into the cavity, thus resulting in non-linear conversion also in the backward direction. At lower pump power levels, the nonlinear crystal was double-passed by the 1064 nm laser and 593 nm light of approximately the same amount was generated in the two directions. However, as the pump power was increased, the 1064 nm laser started to behave as a coupled cavity system with the new cavity formed between the HR facet of the laser crystal and the newly added mirror, and with mirror M1 as the coupling mirror. Reaching this point at approximately 0.75 W of diode pump power, the system became highly unstable, and the average power did not increase further with increasing pump power, as seen in Fig 5.15 (left). The overall system thus operated in a doubly resonant configuration, where the two IR lasers were both intra-cavity with respect to the nonlinear crystal. For comparison, the corresponding measured single-pass 593 nm power is shown in Fig. 5.15 as diamonds.

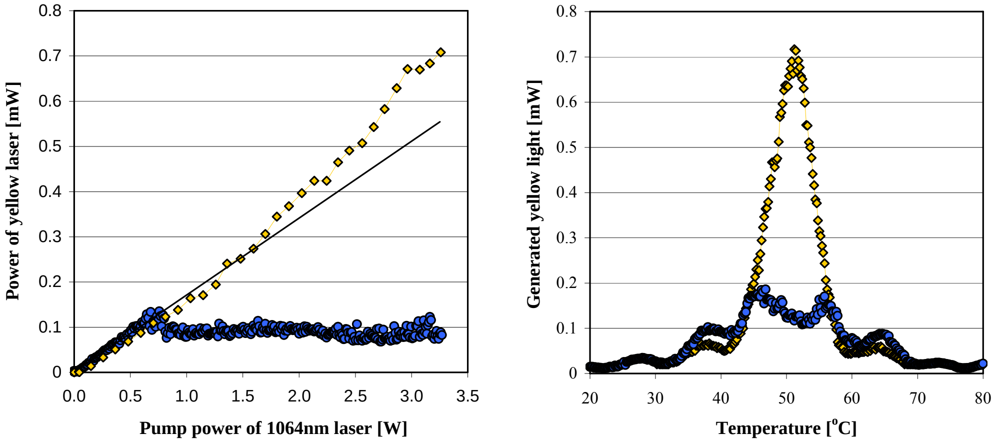

Fig. 5.15 Measured 593 nm output power as function of pump power of the 1064 nm laser (left) and PPKTP crystal temperature (right). Circles correspond to double-pass and diamonds to single-pass configuration. Circles show the power measured in the forward direction. Approximately the same amount of power was seen in the backward direction.

The right part of Fig. 5.15 shows the amount of generated 593 nm power as a function of the PPKTP temperature for maximum pump power. For low magnitudes of the conversion efficiency (corresponding to temperatures far from phase-matching), the measured data follow the expected sinc^2-function and increased 593 nm power in the side peaks of the sinc^2-function is seen as a result of the enhancement of the 1064 nm field. An interesting feature was observed when the temperature was scanned between 45 ˚C and 56 ˚C. As the non-linear coupling grew larger through the optimization of the phase-matching temperature, large amplitude fluctuations in the IR fields appeared and the overall laser system started to operate in a pulsed regime. The average power of the generated 593 nm light was approximately constant during this temperature interval. The measurements indicate that the nonlinear conversion efficiency has to be of a certain magnitude in order to couple the two oscillating fields via the SFG process and to stir up pulsed operation of the infrared fields. By using a fast detector, the amplitude fluctuations of the three fields were measured, see Fig. 5.16. These measurements were carried out at a PPKTP temperature of 51 ˚C and a pump power of the 1064 nm laser at 3.3 W whereas the pump power for the 1342 nm laser was 2.5 W. For these values, the generated 593 nm pulses became periodic with a pulse repetition rate of approximately 50 kHz. Considering that the measured pulse width of the 593 nm light was approximately 100 ns and the average power was 150 mW, this corresponds to a total peak power of 30 W.

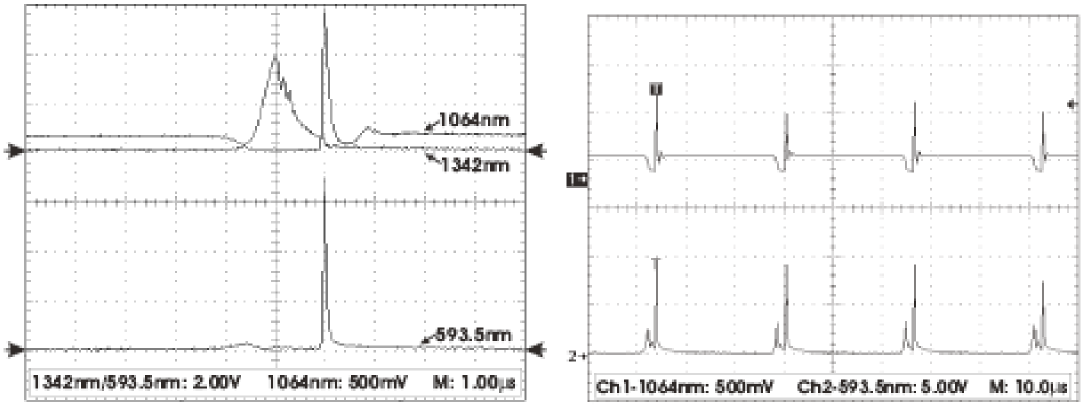

Fig. 5.16 In the left graph, a detail of the amplitude fluctuations of the three fields is shown. To the right, the pulse train of the 1064 nm laser (upper trace) and the generated 593 nm pulses (lower trace) are displayed.

The first system showed a stable and efficient performance as long as the 1064 nm laser was only single-passed through the non-linear crystal. The doubly resonant configuration resulted in a highly unstable operation of the IR lasers. In order to avoid this, a Faraday isolator could be inserted between the 1064 nm and the 1342 nm lasers to prevent a coupled cavity for the 1064 nm laser. At the pump power levels used, no saturation or beam degradation effects were observed. It is therefore expected that this system can be scaled to even higher power levels.

The dynamics of the system needs to be investigated further, in particular when the 1064 nm laser is operated in an intra-cavity configuration together with the 1342 nm laser. Preliminary measurements showed that it is possible to obtain stable pulsed operation of the system for certain magnitudes of the pump powers and 51 ˚C crystal temperature.

5.2.3 Nonlinear Cavity Dumping

In extension to this laser system, another approach to make a pulsed all-solid-state visible light source was investigated. This generic approach is based on sum frequency mixing between the large circulating intra-cavity field of a CW laser and the high peak power from a passively Q-switched solid-state laser. The basic idea is to dump the circulating field in a low-loss laser cavity containing a nonlinear media through non-linear frequency conversion into the visible spectrum by passing a high peak power pulse from a second laser through the nonlinear medium. As the nonlinear losses seen by the intra-cavity laser are proportional to the power of the pulsed laser, the nonlinear losses are zero between the pulses whereas the nonlinear conversion can be very high when the high peak power pulse is present. Thus, the process can be termed nonlinear cavity dumping. Another variation on this principle has proven to be very efficient in terms of generated SFM peak power[98].

For demonstration of the principle[99], a Cr:YAG crystal was inserted in the 1064 nm laser cavity. The initial (small-signal) transmission of this saturable absorber was 90 %, resulting in 100 ns long pulses with a repetition frequency of approximately 215 kHz and a corresponding peak power of 17 W. Although this passively Q-switched laser was far from optimized, the 1064 nm pulses were able to deplete approximately 50 % of the circulating 1342 nm field. In the left graph in Fig. 5.17 below, the time-dependent depletion of the circulating 1342 nm field together with the generated 593 nm pulses. The right graph displays the corresponding 1064 nm pulses, also together with the generated 593 nm pulses. As can be seen, the 593 nm pulses follow exactly the temporal dynamics of the 1064 nm laser. The measured average power of the 593 nm light was 110 mW (taking the Fresnel losses of mirror M4 into account), which corresponds to a peak power of 5.3 W and a normalized conversion efficiency of 0.9 $\%W^{-1}cm^{-1}$. This is somewhat lower than what was achieved for the CW case described in the previous section. In order to utilize the circulating field to maximum, the peak power of the 1064 nm laser should of course be larger. Furthermore, the repetition frequency of the 1064 nm laser should be chosen in such way so that it matches the relaxation oscillations arising from the depletion of the circulating 1342 nm field. The relaxation oscillations from a solid-state laser are typically in the order of ~100 μs[5], which would then set a limit on the maximum repetition frequency of approximately 10 kHz. A 1064 nm laser with this repetition frequency and peak powers in the order of several kilowatts has been demonstrated, although using active Q-switching instead of passive Q-switching. However, total depletion of the 1342 nm laser would occur for peak powers much lower than several kilowatts, at least for the PPKTP crystal used in this experiment (with regard to its high nonlinearity and length). Depending how high peak power that would be used for the nonlinear conversion, there exists a maximum effective length of the nonlinear medium. This is since back conversion would occur when one of the two interacting fields (in this case it is the 1342 nm field) is depleted[4].

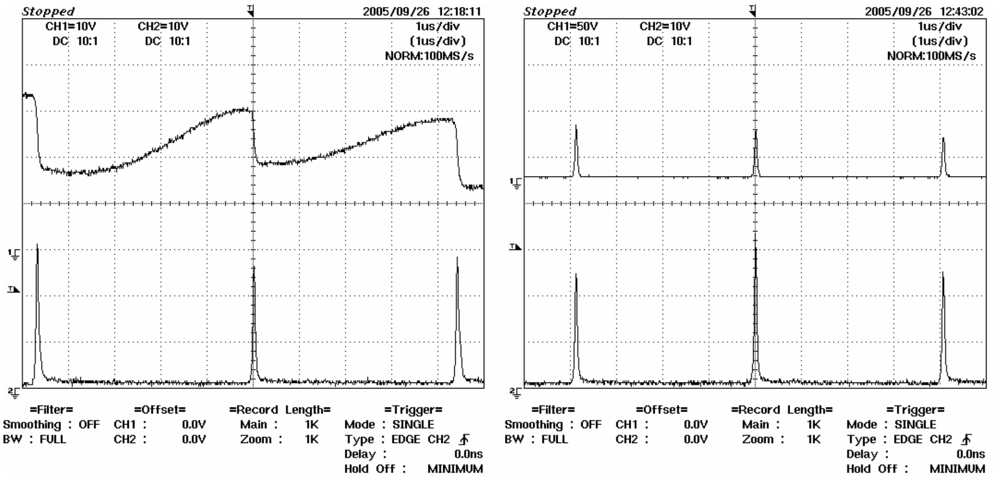

Fig. 5.17 To the left, the temporal dynamics of the 1342 nm laser (upper trace) is shown, together with the generated 593 nm pulses (lower trace). The right graph displays the pulse train measurements of the corresponding 1064 nm laser (upper trace) and 593 nm laser (lower trace).

.

Chapter 6

An all Solid-State deep-UV Light Source

Radiation in the ultraviolet part of the electromagnetic spectrum is desired because of the high photon energy and the ability to reach tight beam focusing. The photon energy in the UV region is sufficient to induce bond-breaking processes in many materials and is thus often used in applications concerning synthesis and processing of materials.

In this Chapter, an all solid-state deep UV source emitting at 236 nm is presented. It based on a frequency-quadrupled, passively Q-switched Nd:YAG laser operating on the $^4F_{3/2} \rightarrow {}^4I_{9/2}$ transition at 946 nm. This work is described in Paper VI.

6.1 UV Light Sources

Ultra-violet light sources find applications in a wide range of areas such as sub-µm lithography, micro-machining, fluorescence detection and imaging, and ophthalmology. Today, light sources used in these areas are mainly excimer lasers, but solid-state lasers are gaining territory because of advantages in efficiency, compactness and low system maintenance cost. However, the output power from solid-state UV lasers is often limited, especially in the shorter wavelength region. This is because the generation of UV radiation from solid-state lasers rely on cascaded frequency conversion, and the nonlinear efficiency is quite low for crystals transparent in the UV spectral region. The latter are primarily crystals from the borate class, e.g. β-barium borate (BBO) and cesium lithium borate (CLBO). Although CLBO has a nonlinear coefficient which is several times higher than that of BBO for wavelengths shorter than 250 µm and has proven to be able to generate UV power in the order of several watts (both in pulsed regime[100,101] and continuous wave[102,103]), CLBO is also known for being highly hygroscopic and needs sophisticated mounting in order to protect it from moisture. Moreover, its physical and thermal properties make it unsuitable for AR-coating. For practical reasons, the remaining choice for deep UV generation at the moment is thus BBO.

To enhance the generated UV radiation, external cavities are often used to resonate one of the interacting frequencies[104,105]. An alternative and simpler approach is the use of pulsed IR sources with high peak-power[106]. Here, a UV light source is presented based on a frequency-quadrupled, passively Q-switched quasi-three-level Nd:YAG laser, using a straightforward and compact setup. We also investigate the performance in terms of nonlinear conversion efficiency of several BiBO - and PPKTP crystals of different lengths. Two different phase-matching temperatures were also tried for the PPKTP crystals.

6.2 The Laser Source

The experimental arrangement of the passively Q-switched 946-nm Nd:YAG laser is depicted in Fig. 6.1. We used a simple, linear cavity design to ensure efficient lasing with good beam quality. A fiber-coupled 808-nm diode (Limo GmbH) was used as the pump source, emitting up to 21 W from a 200 µm fibre with a NA of 0.22. The laser crystal was a composite rod with a 5 mm long Nd:YAG (doping level 1.1 atm%) crystal and 5 mm long undoped YAG end-caps. The end-caps allow for a longitudinal heat flow when the crystal is heated by the pump, which reduces the thermal effects. Its diameter was 3 mm and it was directly watercooled to a temperature of 15 ˚C. Both surfaces were AR-coated for 946 nm. Using two plano-convex lenses with focal lengths of 30 mm, a $1/e^2$-radius beam waist of approximately 100 µm was achieved 2 mm inside the Nd:YAG crystal. The pump absorption ranged between 65% and 77% for diode powers between 7 W and 13 W. A planar mirror with HR coating for 946 nm (AR for 808 nm and 1064 nm) was used as an incoupling mirror, and the output mirror was a curved (ROC = 200 mm) mirror with a transmission of 12 % for 946 nm (AR for 1064 nm).

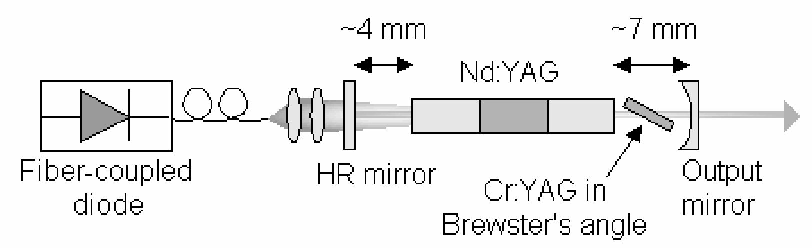

Fig. 6.1 The experimental arrangement of the Q-switched 946-nm laser.

A compact and practical way of Q-switching solid-state lasers is to use passive saturable absorbers, and in the 1 µm spectral region Cr^{4+}:YAG is often chosen because of its high damage threshold. In order to achieve high peak powers, a low initial absorber transmission and a sufficiently small laser beam radius are desired, but these demands has to be balanced with the risk of damage on the coatings. In addition, the quasi-three level nature of this laser imposes conditions on the output coupler transmission and the initial transmission of the saturable absorber, because of the reabsorption losses. We investigated these aspects experimentally and made the choice of a 0.5 mm thin uncoated Cr:YAG disc with an initial transmission of 94% that was employed in Brewster's angle, resulting in a linearly polarized beam with 16 ns-long pulses. For 7 W of absorbed power, the average output power was 0.94 W and the repetition frequency 22 kHz. This corresponds to a pulse energy of 43 µJ and a peak power of 2.9 kW. The beam quality factor M^2 was ≤1.5. Increasing the pump power resulted in higher average power, but lower peak power. This feature is displayed in Fig. 6.2 and Fig. 6.3. Further increasing of the pump power above 13 W degraded the overall performance of the laser in terms of average power, stability and beam quality. The relatively high output coupling of the laser mirror was chosen to minimize the risk of damaging the coatings of the surfaces, since the circulating energy density was high. Nevertheless, for absorbed powers >7W, the load on the (uncoated) surface of the Cr:YAG crystal was apparently so high that it caused damage on the surface. It was assumed that the water absorption around 946 nm was the reason, and to prevent this from occurring, the cavity was purged with N_2 gas. This effort did indeed improve the situation and the laser could perform well also at higher pump levels (but still below 13W).

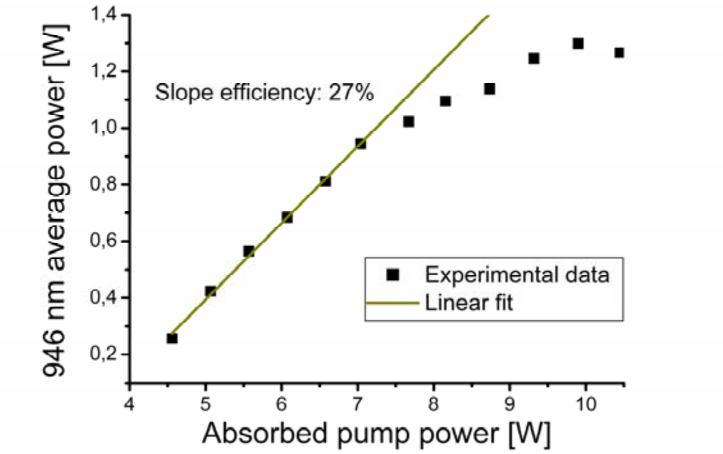

Fig. 6.2 The 946 nm average power as function of absorbed pump power.

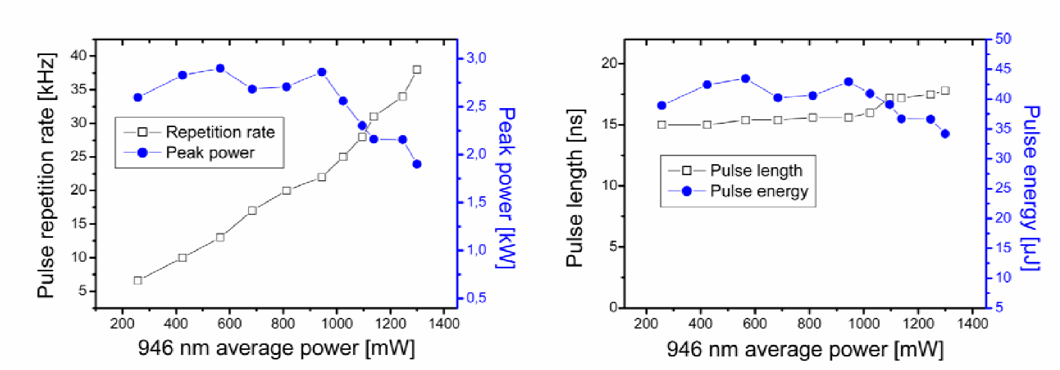

Fig. 6.3 Pulse repetition rate and peak power (left) and pulse length and pulse energy (right) as function of the 946 nm average power.

The damage threshold of the Cr^{4+}:YAG crystal is thus the limiting parameter in this laser and consequently in the generation of 473-nm and 236-nm light. As for the average power, it is also limited by the onset of multi-transverse mode operation determined by the available pumping and laser crystal geometry.

6.3 Second Harmonic Generation using BiBO and PPKTP

Generation of 473-nm light was obtained by frequency doubling in BiB_3O_6 (BiBO) cut for type-I phase-matching (ee->o) with θ = 161.7˚ and φ = 90˚, and periodically poled KTP (PPKTP) with two different nominal grating periods, 6.09 µm and 6.03 µm, designed for first-order quasi phase-matching at 25˚C and 75˚C, respectively. The BiBO crystals had lengths of 10 mm, 5 mm and 3 mm and the PPKTP crystals had lengths of 9 mm, 5 mm and 2 mm. The effective nonlinear coefficient (d_{eff}) of the BiBO crystals was 3.34 pm/V. The value of d_{eff} for the PPKTP crystals was measured by means of second-harmonic generation using a CW Ti-Sapphire laser, giving d_{QPM} = 9.8 pm/V. All PPKTP crystals were uncoated whereas the BiBO crystals had AR-coating for both 946 nm and 473 nm.

To evaluate how different focussing conditions affected the output power and the conversion efficiency of the BiBO crystals, a lens with 40 mm focal length was placed at four different distances from the output mirror of the 946-nm laser, resulting in 10 µm, 15 µm, 20 µm and 30 µm 1/e^2-radius beam waists. A dichroic mirror (HR for 946 nm and AR for 473 nm) and a BG39 filter were used to separate the IR from the 473-nm light. The maximum blue output power, measured for an average 946-nm power equal to 1.3 W, as function of focused beam waist is shown in Fig. 6.4 (left graph) where it can be seen that the longest crystal (10 mm) gives the best results for every focussing condition. As expected from the small crystal acceptance angle (0.65 mrad · cm), the generated 473-nm beam was more astigmatic for longer crystals. It should be noted that the optimum beam waist radii according to the Boyd-Kleinman criteria[35] are 17 µm, 12 µm and 9 µm for crystals of lengths 10 mm, 5 mm and 3 mm, respectively. Thus, it can be concluded that these focussing conditions lies close to those retrieved experimentally, although the latter are somewhat looser. In comparison to the theoretically calculated values for each crystal length, beam waist and 946-nm power (taking pump depletion into account) the experimental results are lower. For each of the three crystals, the maximum average power is around 80% of the theoretical values. Possibly this could be an effect of slightly imperfect fundamental beam quality.

In the right graph in Fig. 6.4 the peak 473-nm power and the conversion efficiency are shown as function of peak 946-nm power for the 10 mm long crystal with a 20 µm focused beam waist radius. For all fundamental peak power levels, the second harmonic peak powers are lower than expected. Though for the lowest measurement point, the experimental conversion efficiency is within the same range as the calculated (20% compared to 23%), but for increased fundamental peak powers (which do not generally correspond to increased 946-nm average powers, see Fig. 6.3) the conversion efficiency reaches a saturation level whereas theory predicts an increasing conversion efficiency as function of fundamental power, and for the highest peak power level an efficiency of 32% is expected instead of the 19% experimentally obtained. In fact, the gap between theoretically expected values and experimental data widens as the 946-nm power increases.

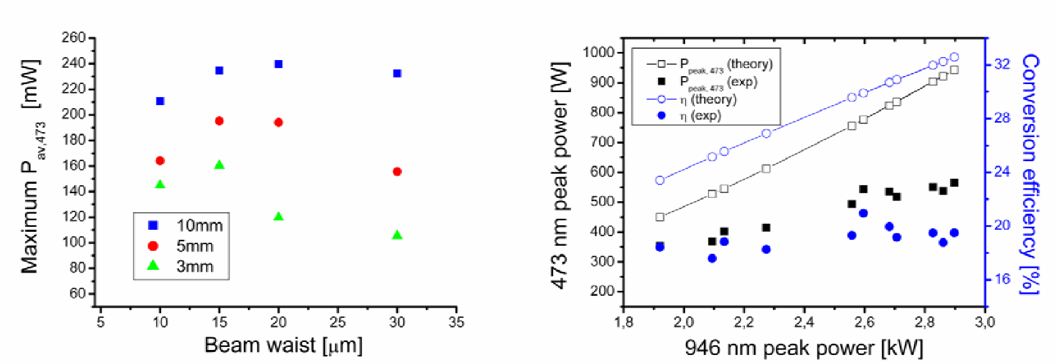

Fig. 6.4 Maximum output power from the BiBO crystals as function of beam waist (left). Second harmonic average power and conversion efficiency as function of fundamental average power for the 10 mm long BiBO crystal, focused beam waist radius = 20 µm (right).

The reason for this behaviour is not evident, although it can be noted that the relatively small acceptance angle (0.65 mrad for the 10 mm crystal) in combination with a somewhat degraded mode quality of the 946-nm beam for high diode pump power can play a significant role. Whereas the Poynting vector walk-off effect is taken into account in the Boyd-Kleinman theory, the crystal acceptance angle is not and would thus affect the value of the focussing parameter *h(ξ, B)*. Since the acceptance angle bandwidth works as a confined aperture and would thus decrease the efficiency homogeneously for all peak powers, experimental data suggests that there is an additional parasitic effect. We see mainly two candidates for this:

nonlinear (absorption) losses and/or dephasing effects due to linear absorption of the blue light leading to heating of the crystal and tuning away from phase-matching. As for other effects, such as photorefraction, no evident signs could be seen. In all cases, the power stability was better than 1% and no crystal damage occurred at any power level.

Similar experiments were then carried out for the PPKTP crystals. Crystals with two different phase-matching temperatures, 25˚C and 73˚C were compared in terms of output power and stability. The high fundamental peak powers in combination with long crystal length can have serious drawbacks because of linear absorption and the photocromic effect in KTP (which gives rise to temperature gradients), causing large instabilities in output power and impaired conversion efficiency. It has earlier been experimentally verified that an elevated crystal temperature can diminish the photochromic effect [88,107,108]. These issues will be discussed in more detail below.

In order to avoid crystal damage, rather loose focusing was used, where the 946-nm beam was imaged to form circular beam waist radii of 45 µm, 65 µm and 85 µm, respectively, in the PPKTP crystals using a lens with a focal length of 100 mm. Large instability in the 473-nm average power was observed for both the 9 mm-long crystals under all focusing conditions, and the power level did not exceed 370 mW in any of them. As for the 2 mm-long crystals, the power stability was good, but rather low blue output power levels were measured. An overview of the results achieved is displayed in Table 6.1.

	L_{cr} = 2 mm			L_{cr} = 5 mm			L_{cr} = 9 mm		
ω_0	45µm	65µm	85µm	45µm	65µm	85µm	45µm	65µm	85µm
T_0 = 25˚C	83	67	29	327	352	220	338	356	317
T_0 = 73˚C	190	139	57	354	405	263	353	366	296

Table 6.1. Average 473-nm power achieved with 45, 65 and 85 µm beam waist radii for three different crystal lengths at phase-matching temperatures 25˚C and 73˚C, respectively. All values are given in mW.

The highest average 473-nm power and conversion efficiency were achieved for the 5 mm long PPKTP crystal having a poled period of 6.03 µm and a focused beam waist radii of 65 µm at an average 946-nm power of 1.1 W, giving values of 405 mW and 41 %, respectively. The power stability was within 3 %. Harder focussing did not result in larger conversion efficiency but instead increased the power instability. The average second harmonic power and conversion efficiency are plotted in Fig. 6.5 as function of average fundamental power, where the Fresnel losses of the uncoated PPKTP crystal has been taken into account in the calculation of conversion efficiency. The heat-sink temperature was constant throughout the power measurement. An evident saturation in conversion efficiency can be seen. Also, the conversion efficiency for the lowest average powers is appreciably lower than expected. We believe that this is due to a temperature mismatch at low fundamental power. As for the saturation behaviour, a contributing factor is the non-negligible absorption of the visible light, which grows worse for shorter wavelengths[109]. Apart from the 473-nm loss itself, this also causes temperature gradients in the crystal, similar to what has been observed by Pasiskevicius *et al*[110]. The heat will induce a varying refractive index change in the crystal by the thermo-optic effect, and together with the average temperature variation itself, the phase-matching condition will be distorted. Thus, instability in second harmonic power will follow. Furthermore, the photochromic effect in KTP will cause absorption of the infra-red light, referred to as blue induced infrared absorption (BLIIRA)[108]. This absorption will result in similar effects mentioned above for the visible light absorption, in addition to the decrease in fundamental power available for nonlinear conversion. The combined effect of these phenomena will limit the generated second harmonic power.

In Fig. 6.6 (left) we display the measured phase-matching curve for the 5 mm-long crystal, showing signs of distortion compared to the theoretical sinc^2-curve. This is a typical response when temperature gradients are present[111]. From the numerical fit it is deduced that the phase-matching temperature T_0 was 73˚C and the FWHM temperature bandwidth ΔT_{FWHM} was 7.0˚C. The latter value is in fair agreement with the calculated bandwidth[87] of 5.0˚C, which would correspond to an effective crystal length of 3.6 mm. For comparison, we made a similar measurement using a CW Ti-Sapphire laser (power level around 400 mW) resulting in the phase-matching curve displayed in the right graph in Fig. 6.6. This curve is evidently very close to an ideal sinc^2-function, apart from the somewhat asymmetrical side-peaks. From the numerical fit a phase-matching bandwidth of 5.2˚C was deduced, in excellent agreement with theory. The main reason for the difference in these phase-matching curves is the higher average power of the Q-switched 946-nm laser which leads to more absorbed power, resulting in a larger temperature elevation and shorter effective crystal length.

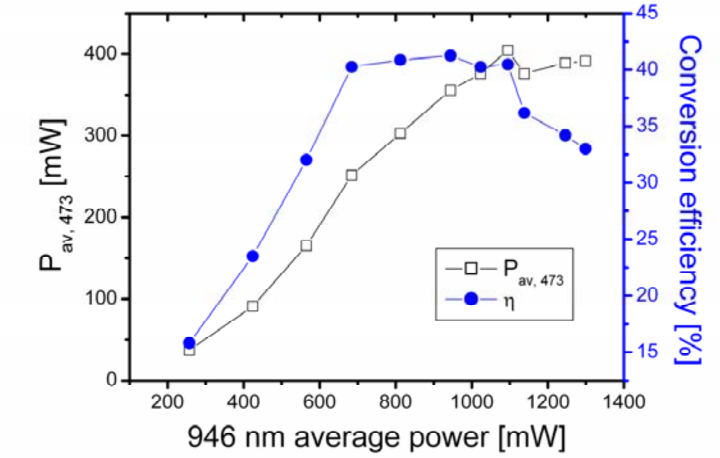

Fig. 6.5 The 473 nm average power and conversion efficiency as function of average 946-nm power. The measurement was done with the 5 mm long PPKTP crystal (Λ = 6.03 µm), using a focused beam waist radius of 65 µm.

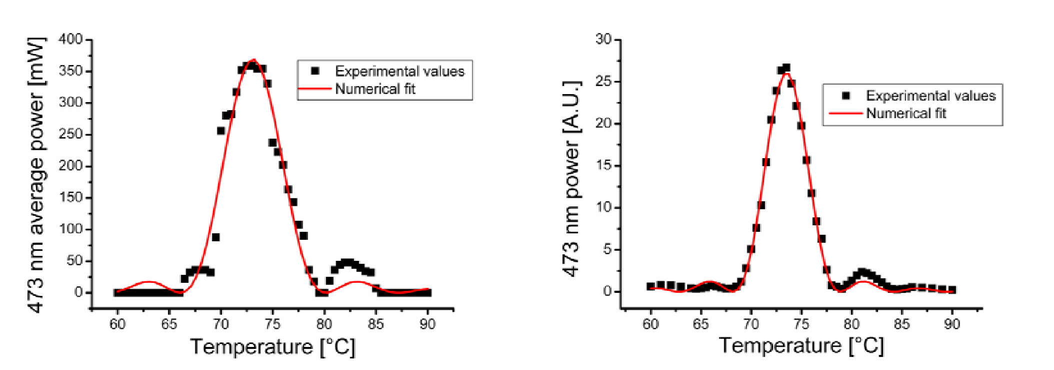

Fig. 6.6 Measurements done with the 5 mm long PPKTP crystal (Λ = 6.03 µm), using a focused beam waist radius of 65 µm. Left graph: The 473 nm average power as function of PPKTP crystal temperature, T_0 = 73˚C and ΔT_{FWHM} = 7.0˚C. Right graph: The 473 nm power as function of PPKTP crystal temperature, using a CW Ti-Sapphire laser as fundamental source. T_0 = 73˚C and ΔT_{FWHM} = 5.2˚C

It should also be mentioned that catastrophic damage occurred in the 2 mm-long, 6.03 µm-poled PPKTP crystal for a focused beam waist radius of 38 µm, which would correspond to a damage threshold of 92 MW/cm^2 (fundamental peak intensity, with Fresnel losses taken into account). This value corresponds well to the previously recorded data[112]. It should also be noted that no grey-tracking was observed in any of the PPKTP samples. In retrospective, a shorter poling period (which would mean a higher phase-matching temperature) might be more effective in terms of avoiding temperature gradients in the crystal and thus improving the power stability. Also, better thermal contact between the heat sink and PPKTP crystal could be a means of improving the power stability.

It can thus be concluded that although BiBO can provide 473-nm light with good power stability and relatively high conversion efficiency at room temperature, PPKTP is still the better choice because of its larger nonlinear coefficient.

6.4 Generation of 236 nm Light

The 473-nm light generated from the 5 mm long PPKTP crystal ($\Lambda = 6.03$ µm) was used for UV generation by single-pass frequency doubling in a 3x3x3 mm^3 β-BaB$_2$O$_4$ (BBO) crystal cut for type-I (oo->e) phase-matching ($\theta = 57.5^\circ$). The crystal was AR-coated for 473 nm and 236.5 nm. The phase-matching temperature was 23˚C and the nonlinear coefficient d_{eff} was 1.5 pm/V. A fused silica lens with focal length 40 mm was used to focus the blue light down to a 21 µm 1/e^2-radius beam waist in the BBO crystal, which corresponds to loose focusing in the Boyd-Kleinman theory. To measure the 236-nm light, a fused-silica prism and a Schott glass filter (UG5) was inserted after the BBO crystal to separate the UV from the residual blue light. With filter and absorption losses accounted for, the maximum 236.5-nm average power was 19.6 mW. Given that the 473-nm average power was 405 mW, this corresponds to a conversion efficiency of 4.8%. Average UV power and conversion efficiency as function of average 473 nm power is presented in Fig. 6.7, together with numerical fits. The 473-nm power was increased by turning up the pump power of the 946-nm laser. As is obvious from the figure, no saturation effects occurred at any power levels.

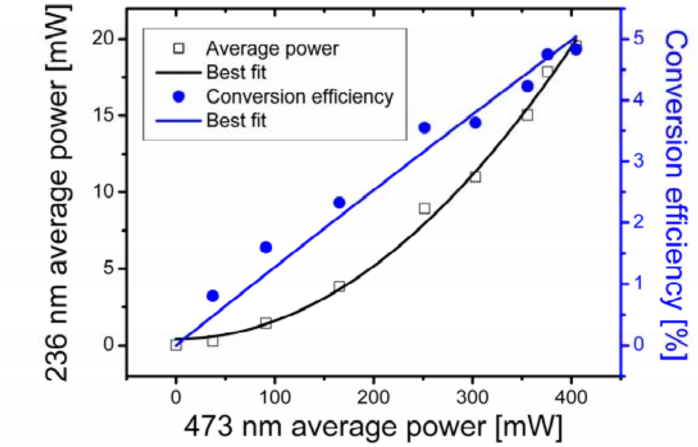

Fig. 6.7 UV average power and conversion efficiency as functions of 473 nm average power. The solid curves are best fits.

It can be noted that harder focussing (down to 12 µm given by the Boyd-Kleinman criteria) did not increase the output power, which can be explained by the small acceptance angle in the bc-plane in BBO (0.17 mrad · cm).

For several applications, good beam quality and low beam divergence is of importance. Using a camera with a pyroelectric sensor, we recorded an image of the UV beam, displayed in Fig. 6.8. Only a few side fringes were detected in the direction of walk-off, as expected, and we estimate that most of the power was contained in the central peak. The far-field diffraction angles were approximately 0.5 mrad x 1.5 mrad (full angle).

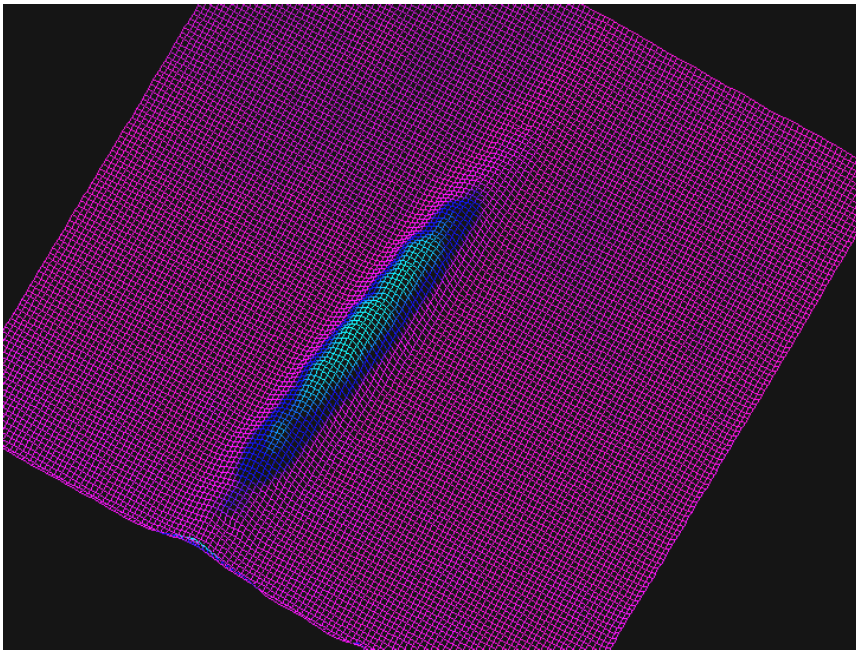

Fig. 6.8 UV beam in the far-field. The picture is taken with a pyroelectric sensor-based camera.

Chapter 7

Description of Work and Author Contribution

Paper I

Generation of turquoise light by sum-frequency mixing of a diode-pumped solid-state laser and a laser diode in periodically poled KTP
S. Johansson, S. Spiekermann, S. Wang, V. Pasiskevicius, F. Laurell, and K. Ekvall
Opt. Expr. **12**, 4935 (2004)

A versatile concept for generation of visible light was demonstrated using a laser diode having good beam quality and a diode-pumped solid-state laser in sum-frequency mixing in a single-pass configuration. Taking advantage of the relatively high output power from the solid-state laser and the flexibility in terms of wavelength for the laser diode, a compact 492 nm light source with an output power of 4 mW was constructed. A conversion efficiency as high as 2.2 $\%W^{-1}cm^{-1}$ was achieved, partly due to the high nonlinearity of the PPKTP crystal used in the frequency mixing. The generated 492 nm power exhibited very low noise, only a small peak at 2.3 MHz could be detected, which was assumed to originate from relaxation oscillations of the Nd:YVO$_4$ laser.

Contributions by the candidate: The candidate and S. Spiekermann designed the experimental setup. The experiment and the measurements were conducted by the candidate and V. Pasiskevicius. The periodically poled KTP crystal was fabricated by S. Wang. The candidate was responsible for writing the paper.

Paper II

Compact 492-nm light source based on sum-frequency mixing
S. Johansson, S. Wang, V. Pasiskevicius, and F. Laurell
Opt. Expr. **13**, 2590 (2005)

This paper was a continuation of Paper I, where the high circulating field of the intra-cavity 1064 nm laser was utilized for the frequency conversion into the turquoise spectral region. A maximum power of 27 mW of 492 nm light was achieved from sum frequency mixing of 170 mW of laser diode power and 39 W of circulating power, using less than 1 W of pump power for the diode-pumped solid-state laser. The 492 nm signal had a high stability and a RMS noise value of 2.5 % was measured. The same noise characteristics were observed in the solid-state laser. As opposed to visible laser sources employing intra-cavity second-harmonic generation who are marred by the “green problem”, the stability of the sum-frequency based light source is directly connected to the noise of the interacting lasers and is not related to the nonlinear conversion. Thus, the noise can be suppressed by stabilising the solid-state laser.

Contributions by the candidate: The experimental setup was designed by the candidate. The experiment and the measurements were conducted by the candidate. The periodically poled KTP crystal was fabricated by S. Wang. The paper was written by the candidate together with V. Pasiskevicius and F. Laurell.

Paper III

Efficient all solid-state continuous-wave yellow-orange light source
J. Janousek, S. Johansson, P. Tidemand-Lichtenberg, S. Wang, J.L. Mortensen, P. Buchhave, and F. Laurell
Opt. Expr. **13**, 1188 (2005)

Here, sum-frequency generation using two diode-pumped solid-state lasers oscillating at 1064 nm and 1342 nm, respectively, was performed. A highly efficient 593 nm laser source was developed using PPKTP as the nonlinear medium, capable of delivering 750 mW of continuous-wave output power. This corresponds to an optical-to-optical efficiency of 11%. In addition to the singly resonant configuration, the performance of a doubly resonant system was investigated. For certain magnitudes of the pump power, the doubly resonant laser system began to self-pulsate, emitting 100 ns long pulses with a peak power of 20 W.

Contributions by the candidate: The candidate participated in the design of the experimental setup and took part in the initial experiment and measurements. The periodically poled KTP crystal was fabricated by S. Wang. The paper was written by J. Janousek together with the candidate.

Paper IV

Polymer encapsulated miniature Nd:YAG lasers
D. Evekull, S. Johansson, S. Bjurshagen, M. Olson, R. Koch, and F. Laurell
El. Lett. **39**, 1446 (2003)

In this paper, a design concept for miniaturised diode-pumped solid-state lasers based on heat-conducting polymer carriers was presented. Using rhombic cut Nd:YAG microchips a total output power of 2 W at 1064 nm was achieved. This design concept provides a rugged building-set suitable for mass-production.

Contributions by the candidate: The design of the setup was done by R. Koch and the first experiments were conducted by D. Evekull. The candidate had the main responsibility for the final experiment and performed the measurements. The candidate wrote the paper with assistance from D. Evekull and S. Bjurshagen.

Paper V

Solid-state laser pumped by twisted beam shaped laser diode

S. Johansson, V. Pasiskevicius, F. Laurell, R. Hansson and K. Ekvall
Submitted to Optics Communications in November 2006

In this paper, a novel method of beam shaping the elliptical and astigmatic beam of a laser diode is presented. This method is based on the twisted Gaussian-Schell model beams, where asymmetrical beams are transformed into symmetrical beams with an added twist phase. In an effort to scale down the dimensions of the transformation optics, GRIN lenses were used to equalize the beam parameter products of a conventional broad-stripe 2 W laser diode into 24 and 18, respectively. The beam twisted laser diode was used for pumping of an intra-cavity frequency-doubled Nd:YAG quasi-three level laser operating at 946 nm, yielding 28 mW of output power in a Gaussian mode.

Contributions by the candidate: The design of the experimental setup was initially investigated by R. Hansson and K. Ekvall and the candidate performed the experiment and measurements. The candidate and V. Pasiskevicius discussed the theory and did the theoretical derivations. The paper was written by the candidate together with V. Pasiskevicus and F. Laurell.

Paper VI

An all solid-state UV source based on a frequency-quadrupled, passively Q-switched 946 nm laser

S. Johansson, S. Bjurshagen, C. Canalias, V. Pasiskevicius, F. Laurell, and R. Koch
Submitted to Optics Express in October 2006

A 236-nm light source with 20 mW of average power is reported using critically phase-matched second-harmonic generation in a beta-barium borate crystal at room temperature. The fundamental light source was a passively Q-switched 946 nm Nd:YAG laser tunable from 10 – 38 kHz and with a pulse length of 16 ns. In the generation of 473 nm light, periodically poled KTP and BiBO was compared in terms of conversion efficiency and stability. Two different phase-matching temperatures were also tried for the PPKTP crystals. The best experimental results were achieved with a 5-mm long PPKTP sample with a phase-matching temperature of 73 ˚C.

Contributions by the candidate: The experimental setup was designed and optimised by the candidate together with S. Bjurshagen and V. Pasiskevicius. The experiment and the measurements were mainly conducted by the candidate. The periodically poled KTP crystals were fabricated by C. Canalias. The candidate wrote the paper with assistance from V. Pasiskevicius, F. Laurell and S. Bjurshagen.

Chapter 8

Conclusions

In this thesis some new concepts for construction of visible and UV solid-state lasers were investigated. The lasers that have been designed and constructed have been based on the host crystals yttrium aluminium garnet (YAG) and yttrium vanadate (YVO_4) doped with the trivalent rare earth ion neodymium (Nd^{3+}). For the nonlinear conversion, periodically poled potassium titanyl phosphate (PPKTP), bismuth triborate (BiBO) and beta barium borate (BBO) have been employed.

Efficient lasing of a miniaturised Nd:YAG laser has been achieved using micro-carriers fabricated from a thermally conductive polymer. This is a generic approach that is especially suited for mass-production of functional laser devices.

In addition, it has been proven that GRIN lenses can provide a very compact beam shaping solution to standard laser diodes. In the case of pumping of solid-state lasers, it is desired to achieve good spatial overlap between the pump mode and the laser mode in order to ensure efficient extraction of the pump power. Especially for gain media lasing on quasi-three level transitions, the requirement for a tightly confined pump beam becomes even more acute. As laser diodes emit elliptic and astigmatic beams, it thus becomes necessary to employ a method of beam shaping. Our suggested method is an elaboration of a previously introduced concept of beam twisting, where asymmetrical beams are transformed into symmetrical beams with an added twist phase. By using GRIN lenses instead of conventional optics, compactness of the beam shaping system is obtained, at the same as automated assembly in solid-state laser manufacturing is facilitated due to the shape of these lenses. Furthermore, this beam shaping method has the important feature of polarisation preservation of the laser diode output. This is of special importance when pumping anisotropic laser media such as widely used ortho-vanadates or double tungstates since the polarization state of the pump light translates directly into the absorbed pump power and thus the laser output power.

A versatile approach for generation of visible light has been demonstrated using a laser diode of good beam quality and a diode-pumped solid-state laser in sum-frequency mixing. The idea is to take advantage of the individual strength of each device, which would be the flexibility in terms of wavelength for the laser diode and the possibility to reach high output power from the diode-pumped solid-state laser. As a proof of concept, we choose a 915 nm laser diode having good beam quality and a Nd:YVO_4 laser oscillating at 1064 nm to obtain light at 492 nm. In the first setup, a single-pass configuration for both the laser diode and the solid-state laser was used, yielding 4 mW of 492 nm output power. This corresponds to a conversion efficiency of 2.2 % $W^{-1}cm^{-1}$, which was to a large extent owing to the high nonlinearity of the PPKTP crystal used for the frequency conversion. However, since mode-hopping in the laser diode occurred, it became necessary to stabilize the laser diode at the phase-matching wavelength. This was done by means of a transmission grating employed in a Littrow configuration. A linewidth of approximately 300 MHz was measured, and the laser diode could be tuned between 906 nm and 916 nm where it operated perfectly stable. As a natural continuation of this scheme, the PPKTP crystal was placed inside the cavity of the Nd:YVO$_4$ laser, thus exploiting the high circulating field of the 1064 nm light. Still maintaining a very compact experimental setup, a maximum output power of 27 mW at 492 nm was attained. Apart from the freedom in choice of wavelength and the possibility to build compact light sources, another advantage of this scheme is the low noise characteristics. As opposed to visible laser sources employing intra-cavity second-harmonic generation who are marred by the "green problem", the stability of the sum-frequency based light source is directly connected to the noise of the interacting lasers and is not related to the nonlinear conversion. Thus, the noise can be suppressed by stabilising the individual lasers taking part in the nonlinear interaction. In all, a light source based on this scheme is thus well suited for biomedical applications, where high-frequency noise can have a detrimental effect on the accuracy of the bioanalysis.

Less freedom in the choice of wavelength, but substantially more output power was demonstrated in another scheme based on sum-frequency mixing where two different diode-pumped solid-state lasers were used for the nonlinear frequency conversion. We developed a 593 nm light source based on the nonlinear interaction in a PPKTP crystal between two Nd:YVO$_4$ lasers operating at 1064 nm and 1342 nm, respectively. An optical-to-optical efficiency as high as 11% was achieved, as the 593 nm light source generated up to 750 mW of output power from a total laser diode power of 6.4 W. This yellow-orange laser source has its main applications in dermatology and ophthalmology, due to the high absorption in haemoglobin in this particular spectral region.

Moreover, the emission wavelengths of both these visible laser sources correspond to the peak absorption of several popular fluorophores.

Finally, a deep-UV all solid-state laser source with 20 mW of average power was reported. A light source in this spectral region can provide enough photon energy to induce bond-breaking processes in many materials and could accordingly be utilised in applications such as lithography and material synthesis. A comparative study of the properties of PPKTP and BiBO was carried out during the course of this work. In the case of PPKTP, two different phase-matching temperatures were also evaluated. As for the nonlinear conversion efficiency, the PPKTP crystals outperformed the BiBO crystals. However, large amplitude fluctuations were observed using PPKTP phase-matched at room-temperature whereas BiBO could provide a 473 nm power stability within 1%. As it has earlier been shown that an elevated temperature can reduce the photochromic effect in KTP, a phase-matching temperature of 73 ˚C was tried for the nonlinear conversion into the blue spectral region. This method also proved to be efficient, resulting in a power stability within 3 % of the generated light, while maintaining the excellent conversion efficiency of PPKTP.

References

1. L. Schawlow and C. H. Townes, Phys. Rev. **112**, 1940 (1958).
2. T. H. Maiman, Nature **187**, 493 (1960).
3. P. Franken, A. Hill, C. Peters, and G. Weinreich, Phys. Rev. Lett. **7**, 118 (1961).
4. W. P. Risk, T. R. Gosnell and A. V. Nurmikko, *Compact Blue-Green Lasers* (Cambridge University Press 2003).
5. O. Svelto, *Principles of Lasers* (Springer, 1998).
6. A. E. Siegman, *Lasers* (University Science Books, California, 1986).
7. Y. F. Chen, C.F. Kao, and S.C. Wang, Opt. Comm. **133**, 517 (1997).
8. Y. Guyot, H. Manan, J. Y. Rivoire, R. Moncorgé, N. Garnier, E. Descroix, M. Bon, and P. Laporte, Phys. Rev. **B** 51, 784 (1995).
9. T. Chuang and H. R. Verdún, IEEE J. Quant. Electr. **32**, 79 (1996).
10. S. Guy, C. L. Bonner, D. P. Sheperd, D. C. Hanna, A. C. Tropper, and B. Ferrand, IEEE J. Quant. Electr. **34**, 900 (1998).
11. M. Pollnau, P. J. Hardman, W. A. Clarkson, and D. C. Hanna, Opt. Comm. **147**, 203 (1998).
12. M. Pollnau, P. J. Hardman, M. A. Kern, W. A. Clarkson, and D. C. Hanna, Phys. Rev. B. **58**, 16076 (1998).
13. P. J. Hardman, W. A. Clarkson, J. A. Friel, M. Pollnau, and D. C. Hanna, IEEE J. Quant. Electr. **35**, 647 (1999).
14. W. G. Wagner and B. A. Lengyel, J. Appl. Phys. **34**, 2040, (1963).
15. Szabo and R. A. Stein, J. Appl. Phys. **36**, 1562 (1965).
16. X. Zhang, S. Zhao, Q. Wang, Q. Zhang, L. Sun, and S. Zhang, IEEE J. Quant. Electr. **33**, 2286 (1997).
17. Z. Burschtein, P. Blau, Y. Kalisky, Y. Shimony, and M. R. Kokta, IEEE J. Quant. Electr. **34**, 292 (1998).
18. J. J. Degnan, IEEE J. Quant. Electr. **31**, 1890 (1995).
19. J. J. Degnan, D. Barry Coyle, and R. B. Kay, IEEE J. Quant. Electr. **34**, 887 (1998).
20. G. M. Zverev, G. Ya Kolodny, and A. M. Onischenko, Sov. Phys. JETP, **33**, 497 (1971).
21. W. A. Clarkson, N.S. Felgate, and D.C. Hanna, Opt. Lett. **24**, 820 (1999).
22. T. Y. Fan and R. L. Byer, IEEE J. Quant. Electr. 2**3**, 605 (1987).
23. W. Koechner, *Solid-State Laser Engineering* 5th Ed. (Springer Berlin, 1999).
24. S. Singh, R. G. Smith, and L. G. Van Uitert, Phys. Rev. B. **10**, 2566 (1974).
25. X. Zhang, A. Brenier, J. Wang, and H. Zhang, Opt. Materials **26**, 293 (2004).
26. L. A. Riseberg and H. W. Moos, Phys. Rev. **174**, 429 (1968).
27. C. Bibeau, S. A. Payne, and H. T. Powell, **12**, 1981 (1995).
28. P. N. Butcher and D. Cotter, *The Elements of Nonlinear Optics* (Cambridge University Press, 1990).
29. R. W. Boyd, *Nonlinear Optics* (Academic Press, 1992).
30. Y. R. Shen, *The Principles of Nonlinear Optics* (John Wiley & Sons, 1984).
31. R. Sutherland, *Handbook of Nonlinear Optics* (Marcel Dekker, Inc. 2003).
32. Yariv, *Quantum Electronics* (John Wiley & Sons, 1989).

33. D. A. Kleinman, Phys. Rev. **126**, 1977-1979 (1962).
34. J. A. Armstrong, N. Bloembergen, J. Ducuing, and P. S. Pershan, Phys. Rev. **127**, 1918 (1962).
35. G. D. Boyd and D. A. Kleinman, J. Appl. Phys. **39**, 3597 (1968).
36. S. Guha and J. Falk, J. Appl. Phys. **51**, 50 (1980).
37. J. A. Giordmaine, Phys. Rev. Lett. **8**, 19 (1962).
38. P. D. Maker, R. W. Terhune, M. Nisenoff, and C. M. Savage, Phys. Rev. Lett. **8**, 21 (1962).
39. E. A. Saleh and M. C. Teich, *Fundamentals of Photonics* (John Wiley & Sons, 1991)
40. P. A. Franken and J. F. Ward, Rev. Mod. Phys. **35**, 23 (1963).
41. M. Yamada. N. Nada, M. Saitoh, and K. Watanabe, Appl. Phys. Lett. **62**, 435 (1993).
42. M. M. Fejer, G. A. Magel, D. H. Jundt, and R. L. Byer, IEEE J. Quant. Electr. **28**, 2631 (1992).
43. L. Ouvrard and M. Troost, Compt. Rend., **111**, 177 (1890).
44. Tordjman, R. Masse, and J. C. Guitel, Zeitschrift für Kristallographie, **139**, 103 (1974).
45. F. C. Zumsteg, J. D. Bierlein, and T. E. Gier, J. Appl. Phys., **47**, 4980 (1976).
46. H. Hellwig, J. Liebertz, and L. Bohatý, Solid State Comm. **109**, 249 (1999).
47. M. Ghotbi and M. Ebrahim-Zadeh, Opt. Expr. **12**, 6002 (2004).
48. R. Eckardt, H. Masuda, Y. Fan, R. L. Byer, IEEE J. Quant. Electr. **26**, 922 (1990).
49. T. Sasaki, Y. Mori, M. Yoshemure, Y. K. Yap, and T. Kamimura, Mat. Sci. Eng. R **30**, 1 (2000).
50. Chen, Z. Lin, and Z. Wang, Apll. Phys. B **80**, 1 (2005).
51. J. J. Zayhowski and A. Mooradian, Opt. Lett. **14**, 24-26 (1989).
52. Å. Claesson, J. Holm, R. Koch, M. Olson, A. Olsson, C. Vieider, H. Åhlfeldt, and F. Laurell, El. Lett., **36**, 433-434 (2000).
53. J. Wallace, ”Polymer is foundation for Nd:YAG laser,” Laser Focus World **40**, 1 (2004).
54. B. Ehlers, K. Du, M. Baumann, H.-G. Treusch, P. Loosen, and R. Poprawe, SPIE **3097,** 639-644 (1997).
55. H. Zbinden and J.E. Balmer, Opt. Lett. **15,** 1014-1016 (1990).
56. W.A. Clarkson and D.C. Hanna, Opt. Lett. **21,** 375-377 (1996).
57. R. Simon and N. Mukunda, J. Opt. Soc. Am. A **10,** 95-109 (1993).
58. A.T. Friberg, E. Tervonen, and J. Turunen, J. Opt. Soc. Am. A **11,** 1818-1826 (1994).
59. H. Laabs, C. Gao, and H. Weber, J. Mod. Opt. **46,** 709-719 (1999).
60. Gao, H. Laabs, H. Weber, T. Brand and N. Kugler, Opt. Quant. El. **31,** 1207-1218 (1999).
61. L. Allen, M. W. Beijersbergen, R. J. C. Spreeuv, and J. P. Woerdman, Phys. Rev. A, **45,** 8185-8189 (1992).
62. M. W. Beijersbergen, L. Allen, H. E. L. van der Veen, and J. P. Woerdman, Opt. Comm., **96,** 123-132 (1993).
63. J. Courtial and M. J. Padgett, Opt. Comm., **159**, 13-18 (1999).
64. J. Camacho, and D. Tentori, J. of Optics A: Pure and Appl. Opt., **3**, 89-95 (2001).
65. H. Laabs, C. Gao, H. Weber, N. Kugel, and C. Zhao, Proc. SPIE, **3611**, 258-268 (1999).
66. L. Marshall, “Many variant lasers compete in the blue,” Laser Focus World, October, 79-83 (2004).

67. J. Webjörn, F. Laurell, and G. Arvidsson, IEEE Photonics Tech. Lett. **1**, 316 (1989).
68. Laurell: "Periodically poled materials for miniature light sources," Optical Materials **11**, 235 (1999).
69. T.D. Raymond, W.J. Alford, M.H. Crawford and A.A. Allerman, Opt. Lett. **24**, 1127 (1999).
70. Caprara, J.L. Chilla and L.A. Spinelli, US Patent 6,097,742 (2000).
71. Schielen, M. Golling and P. Unger, IEEE Photonics Tech. Lett. **14**, 777 (2002).
72. E.U. Rafailov, W. Sibbett, A. Mooradian, J. G. McInerney, H. Karlsson, S. Wang and F.Laurell, Opt. Lett. **28**, 2091 (2003).
73. A. Bouchier, G. Lucas-Leclin, P. Georges, and J. M. Maillard, Opt. Expr. **13**, 6974 (2005).
74. M. A. Holm, D. Burns, A.I. Ferguson and M.D. Dawson, Conference on Lasers and Electro-Optics (CLEO 2000), TOPS Vol.39, 2000, pp. 440-441.
75. M. Jacquement, F. Druon, F. Balembois, P. Georges, B. Ferrand, Opt. Expr. **13**, 2345 (2005).
76. D. Woll, B. Beier, K.J. Boller, R. Wallenstein, M. Hagberg and S. O'Brien, Opt. Lett. **24**, 691 (1999).
77. D. Woll, J. Schumacher, A. Robertson, M. A. Tremont, R. Wallenstein, M. Katz, D. Eger and A. Englander, Opt. Lett. **27**, 1055 (2002).
78. J.C. Bienfang, C.A. Denman, B.W. Grime, P.D. Hillman, G.T. Moore and J.M. Telle, Opt. Lett. **28**, 2219 (2003).
79. N. Saito, K. Akagawa, Y. Hayano, Y. Saito, H. Takami and S. Wada, in Advanced Solid-State Photonics, J. J. Zayhowski and G.J. Quarles, eds., Nineteenth Topical Meeting and Tabletop Exhibit (Optical Society of America, Santa Fe, New Mexico, 2004).
80. E. Herault, F. Balembois and P. Georges, Opt. Expr. **15**, 5653 (2005).
81. W.P. Risk, J.C. Baumert, G.C. Bjorklund, F.M. Schellenberg and W. Lenth, Appl. Phys. Lett. **52**, 85 (1988).
82. D.W. Anthon, G.J. Dixon, M.G. Ressl and T.J. Pier, Proc. SPIE, 898, 68 (1988).
83. W.P. Risk and W. Lenth, Appl. Phys. Lett. **54**, 789 (1989).
84. P.N. Kean, R.W. Standley and G.J. Dixon, Appl. Phys. Lett. **63**, 302 (1993).
85. L. Goldberg, M.K. Chun, I.N. Duling and T.F. Carruthers, Appl. Phys. Lett. **56**, 2071 (1990).
86. W.P. Risk and W.J. Kozlovsky, Opt. Lett. **17**, 707 (1992).
87. M.M. Fejer, G.A. Magel, D.H. Jundt and R.L. Byer, IEEE J. Quantum Electron. **28**, 2631 (1992).
88. S. Wang, V. Pasiskevicius, and F. Laurell, J. Appl. Phys. **96**, 2023 (2004).
89. T. Baer, J. Opt. Soc. Am. B **3**, 1175 (1986).
90. R. Häring and E. Gerster, EUROPhotonics, 38-39, August/September (2003).
91. M. Pask and J. A. Piper, Opt. Lett. **24**, 1490 (1999).
92. A.Sennaroglu, Appl. Opt. **41**, 4356 (2002).
93. Y. F. Chen, S. W. Tsai, S. C. Wang, Y. C. Huang, T. C. Lin and B. C. Wong, Opt. Lett. **27**, 1809 (2002).
94. S. Spiekermann, H. Karlsson, F. Laurell and I Fritag, Electron. Lett. **36**, 543 (2000).
95. C. Yung-Fu abd S. W. Tsai, Opt. Lett. **27**, 397 (2002).
96. Y. F. Chen and S. W. Tsai, Appl. Phys. B. **79**, 207 (2004).
97. Kumagai, K. Midorikawa, T. Iwane and M. Obara, Opt. Lett. **28**, 1969 (2003).
98. E. Herault, F. Balembois and P. Georges, Advanced Solid-State Photonics (Lake Tahoe, Nevada, 2006), paper MC5.

99. P. Tidemand-Lichtenberg, S. Johansson, M. Andersen, J. Janousek, P. Buchhave and F. Laurell, Advanced Solid-State Photonics (Lake Tahoe, Nevada, 2006), paper TuB19.
100. T. Kojima, S. Konno, S. Fujikawa, K. Yasui, and K. Yoshizawa, Opt. Lett. 2**5**, 58 (2000).
101. Sakuma, K. Deki, A. Finch, Y. Ohsako, and T. Yokota, Appl. Opt. **39**, 5505 (2000).
102. Sakuma, Y. Asakawa, and M. Obara, Appl. Opt. **39**, 5505 (2000).
103. Sakuma, Y. Asakawa, T. Imahoko, and M. Obara, Appl. Opt. **39**, 5505 (2000).
104. Chang, S. Wang, and A. Kung, Opt. Comm. **209**, 397 (2002).
105. Oka, L. Liu, W. Wiechmann, N. Eguchi and S. Kubota, IEEE Quantum Electronics. **1**, 859 (1995).
106. D. Gerstenberger, T. Trautmann, and M. Bowers, Opt. Lett. **28**, 1242 (2003).
107. V. Pasiskevicius, H. Karlsson, F. Laurell, R Butkus, V. Smilgevicius, and A. Piskarskas, "Highly efficient optical parametric oscillator in red spectral region with periodically poled KTP", Opt. Lett. **26**, 710 (2001).
108. J. Hirohashi, V. Pasiskevicius, and F. Laurell, "Picosecond blue light-induced infrared absorption in single-domain and periodically poled ferroelectrics," Submitted to J. Appl. Physics.
109. G. Hansson, H. Karlsson, S. Wang, and F. Laurell, "Transmission measurements in KTP and isomorphic compounds," Appl. Opt. **39**, 5058 (2000).
110. V. Pasiskevicius, S. Wang, J. Tellefsen, F. Laurell and H. Karlsson, "Efficient Nd:YAG laser frequency doubling with periodically poled KTP," Appl. Opt. **37**, 7116 (1998).
111. S. Spiekermann, F. Laurell, V. Pasiskevicius, H. Karlsson, and I. Freitag, "Optimizing non-resonant frequency conversion in periodically poled media," Appl. Phys. B. **78**, 211 (2004).
112. S. Wang, Fabrication and characterization of periodically-poled KTP and Rb-doped KTP for applications in the visible and UV (Doctoral Thesis in Physics, Stockholm, Sweden, 2005), http://www.laserphysics.kth.se.